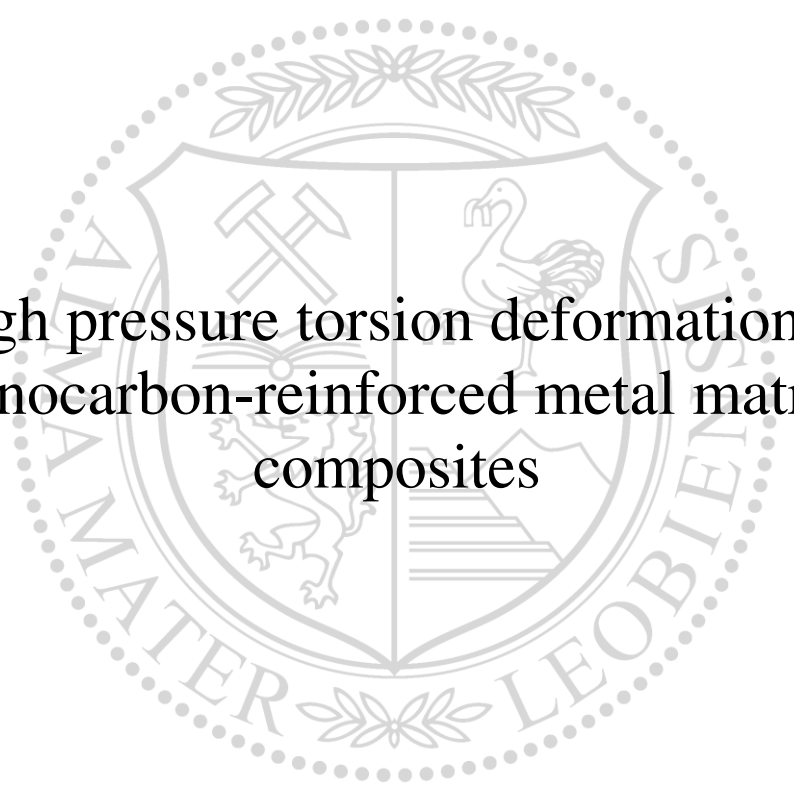




Chair of Materials Physics

Doctoral Thesis



High pressure torsion deformation of
nanocarbon-reinforced metal matrix
composites

Dipl.-Ing. Andreas Katzensteiner

October 2019

This doctoral thesis was written at the Erich Schmid Institute for Materials Science, Austrian Academy of Sciences as part of the FWF project I2294 N36 and typeset by the use of KOMA-Script and L^AT_EX 2_ε.

Erich Schmid Institute of Materials Science
Austrian Academy of Sciences
Jahnstrasse 12
8700 Leoben
Austria

AFFIDAVIT

I declare on oath that I wrote this thesis independently, did not use other than the specified sources and aids, and did not otherwise use any unauthorized aids.

I declare that I have read, understood, and complied with the guidelines of the senate of the Montanuniversität Leoben for "Good Scientific Practice".

Furthermore, I declare that the electronic and printed version of the submitted thesis are identical, both, formally and with regard to content.

Date 15.10.2019



Signature Author
Andreas, Katzensteiner

Acknowledgements

Writing a doctoral thesis is a challenging task and not something, that can be done without help. Therefore, I want to take this opportunity to thank all the people who helped me in this accomplishment.

First and foremost, I want to thank Dr. Andrea Bachmaier for giving me the opportunity to work at the Erich Schmid Institute and to write this thesis. Her continuous support and guidance always helped me in achieving my goals.

I also want to thank Prof. Reinhard Pippan for providing interesting ideas for new experiments, vast amounts of knowledge about materials science and beyond, a guiding hand throughout my work and a place where we can all learn from each other.

I want to thank Katherine Aristizabal and Dr. Sebastian Suarez for the great cooperation in our project and for the warm welcome and hospitality during my visit in Saarbrücken.

A special thanks to all the helping hands at the ESI, who helped me accomplishing my work: Peter for his expertise and help at the HPT, Silke for making even the worst samples shine, Gabi & Wiki for their help and support in all things TEM related, Franz & Robin for always providing the right tool for my work, as well as Thomas & Gerald for keeping the whole thing running.

A great thanks also to all my colleagues at the ESI, especially Karoline Kormout and Julian Rosalie for helping with the HRTEM, and my office colleagues Juraj, David and Michael, as well as Stefan, Martin and Lukas for many fruitful,

interesting and enjoyable discussions both on- and off-topic.

I also want to thank all my friends for their support and their continuous interest in my work. I hope, I could adequately explain what I was working on.

And last but not least, I want to thank my family. Without them I would not be where I am today.

Abstract

In this work, severe plastic deformation (SPD) was used to produce ultrafine-grained (ufg) and nanocrystalline (nc) metal-matrix composites (MMC) with various carbon-derived reinforcement phases. Nickel/Carbon nanotube (Ni/CNT), silver/nanodiamond (Ag/ND), gold/nanodiamond (Au/ND) and nickel/nanodiamond (Ni/ND) composites were produced from powder, either through colloidal mixing, sintering and subsequent high-pressure torsion (HPT) deformation or through ball milling and HPT-consolidation and -deformation.

The microstructural evolution of the HPT-deformed composites was investigated with scanning electron microscopy (SEM), electron backscatter diffraction (EBSD), transmission electron microscopy (TEM) and high-resolution transmission electron microscopy (HRTEM). It could be shown, that the amount of HPT-deformation has a strong influence on the grain size of the matrix material and the size and distribution of the second phase particles. Other similar important influencing factors were the amount of reinforcement particles, the HPT-deformation temperature and for the ball milled composites the milling time and milling velocity. With the right combination of production parameters, it was possible to create MMCs with grain sizes and second phase particle sizes smaller than 100 nm and a homogeneous distribution of the second phase materials.

The mechanical properties of the MMCs were investigated with microhardness measurements, tensile tests and compression tests. The microhardness was measured to increase in concordance with a decrease in the grain size, an increase in the amount of second phase particles as well as with the improvement of the second phase distribution. Along with the microhardness increase, the tensile and compression strength also increase while the ductility of the MMCs decreases.

Compression tests showed a certain mechanical anisotropy in the MMCs which depends mostly on the shape of the second phase particles and their size in relation to the grain size.

Kurzfassung

Die Methode der Hochdrucktorsionsumformung (HPT) wurde in dieser Arbeit verwendet, um ultrafeinkörnige und nanokristalline Metal-Matrix-Komposite mit Kohlenstoff-basierten Verstärkungstoffen herzustellen. Nickel/Kohlenstoffnanoröhrchen (Ni/CNT), Silber/Nanodiamanten (Ag/ND), Gold/Nanodiamanten (Au/ND) und Nickel/Nanodiamanten (Ni/ND) Komposite wurden aus Pulvern durch kolloidales mischen, sintern und HPT-Verformung oder durch Kugelmahlen und HPT-Verdichtung und -Verformung hergestellt.

Die Entwicklung der Mikrostruktur der HPT-verformten Komposite wurde mittels Rasterelektronenmikroskopie (SEM), Elektronen-Rückstreuungsdiffraktion (EBSD), Transmissionselektronenmikroskopie (TEM) und hochauflösender Transmissionselektronenmikroskopie (HRTEM) untersucht. Es konnte gezeigt werden, dass der Grad an HPT-Verformung einen starken Einfluss auf die Korngröße des Matrixmaterials und die Größe und Verteilung der Verstärkungsteilchen hat. Weitere wichtige Einflussfaktoren waren die Menge an Verstärkungsteilchen, die HPT-Verformungstemperatur und für die Komposite die mittels Kugelmahlen hergestellt wurden, die Mahlzeit und -geschwindigkeit. Mit der richtigen Kombination der Produktionsparameter war es möglich, Komposite mit Korngrößen und Teilchengrößen kleiner als 100 nm und einer homogenen Verteilung der Verstärkungsteilchen herzustellen.

Die mechanischen Eigenschaften der Komposite wurden mittels Mikrohärtmessungen, Zugversuchen und Druckversuchen ermittelt. Die Mikrohärtigkeit stieg mit der Verringerung der Korngröße, der Erhöhung des Anteils an Verstärkungsteilchen sowie mit der Verbesserung der Verteilung der Verstärkungsteilchen an. Zeitgleich mit dem Mikrohärtanstieg stiegen auch die Zug- und Druckfestigkeit an während die Duktilität der Komposite abnahm. Druckversuche zeigten eine gewisse mech-

anische Anisotropie, die zum Großteil von der Form der Verstärkungsteilchen und ihrer Größe in Relation zur Korngröße abhängt.

Contents

Acknowledgements	v
Abstract	vii
Kurzfassung	ix
1. Introduction	1
1.1. High-pressure torsion deformation	1
1.2. Nanocarbon-reinforced metal matrix composites	2
1.3. Deformation of nanocarbon-reinforced metal matrix composites by SPD	3
1.4. Motivation and aim of the work	5
2. Carbon-based Nanomaterials	7
2.1. Carbon Nanotubes	8
2.2. Nanodiamonds	11
3. Microstructural evolution of nickel/carbon nanotube composites de- formed by HPT	13
3.1. Experimental	13
3.2. Parameters influencing the microstructure	15
3.2.1. Equivalent strain	15
3.2.2. Second phase content	18
3.2.3. HPT-deformation temperature	19
3.3. Texture evolution	26
3.4. Post-deformation treatment: Annealing	28

Contents

4. Mechanical properties of nickel/carbon nanotube composites	31
4.1. Experimental	31
4.2. Microhardness and tensile strength	33
4.3. Ductility and fracture mechanisms	42
4.4. Compression strength and mechanical anisotropy	48
5. Nanodiamond reinforced metal matrix composites	55
5.1. Pre-deformation treatment: Ball-milling	55
5.2. Experimental	56
5.3. Microhardness and mechanical behaviour	57
5.4. Microstructure	69
6. Strengthening mechanisms in nanocarbon-reinforced metal matrix composites	77
6.1. Hall-Petch strengthening	77
6.2. Dislocation strengthening	81
6.3. Reinforcement strengthening	82
6.4. Load transfer strengthening	85
6.5. Impurities and solid solution strengthening	86
7. Summary	89
References	95
Appendix	107
A. Temperature dependent structural evolution in nickel/carbon nanotube composites processed by high-pressure torsion	109
A.1. Introduction	110
A.2. Experimental	111
A.3. Results and discussion	112
A.4. Conclusion	119

B. Influence of Processing Parameters on the Mechanical Properties of HPT-Deformed Nickel/Carbon Nanotube Composites	123
B.1. Introduction	124
B.2. Experimental Section	126
B.3. Results and Discussion	128
B.3.1. Microstructural development	128
B.3.2. Mechanical properties	129
B.3.3. Anisotropy	137
B.4. Summary	141

1. Introduction

Understanding of the structure property relation is the main scientific objective of the material science community. The goal of these activities is to develop a concept for the improvement of properties. One strategy to improve the mechanical properties, especially the strength, is grain refinement. Many different production methods have been developed to obtain this important task. These methods include amongst others various methods of severe plastic deformation (SPD) such as high-pressure torsion (HPT) or equal channel angular pressing (ECAP) [1] and the mechanical alloying of powdered metals through ball-milling [2]. The combination of materials with different mechanical properties to create a composite is another approach to improve the strength of materials [3].

1.1. High-pressure torsion deformation

HPT-deformation is an often used and relatively simple method to produce ultrafine-grained (ufg) or even nanocrystalline (nc) materials both from bulk materials as well as from powders [1]. Very high shear strains can easily be achieved even for brittle and high-strength materials by compressing the samples between two anvils and rotating one of the anvils against the other. These shear strains lead to fragmentation of the microstructure and a subsequent decrease in the grain size [4]. It can also be utilized for improving the particle distribution and reducing the particle size of the second phase in MMCs. In this case, higher strains are necessary to achieve a fully saturated microstructure than with single-phase materials [5]. A disadvantage of this process is that HPT-deformed materials are limited in the achievable sample size. The most used sample diameter is about 10 mm, however in the last few years an upscaling to about 70 mm has been performed [6].

1. Introduction

HPT-deformation was first developed by Bridgman in 1935 to investigate phase transformations under high pressure conditions [7]. Bridgman used the HPT-deformation process to deform many different materials, ranging from pure metals to glasses, minerals as well as biological materials and polymers. HPT-deformation and SPD in general became popular in the material science community in the late 1980s and early 1990s, when Ruslan Valiev and his colleagues from the Institute of Metals Superplasticity Problems in Ufa, Russia began to investigate ufg structures of Al [8]. Till 2002, all HPT samples have been processed by the russian group. The introduction of the constrained HPT resulted in an enormous international increase in the HPT activities [9–11]. Since then, HPT-deformation has been used for a variety of different materials systems and for the investigation of many different material properties [1, 12].

1.2. Nanocarbon-reinforced metal matrix composites

Metal matrix composites (MMCs) consist of a matrix of one or more metals and a second phase material homogenously dispersed in the matrix. One of the functions of the second phase is to give the composite a high strength through pinning of dislocations as well as inhibiting grain growth in ufg and nc materials, while the metal matrix ensures a certain toughness [3]. Second phase materials are mostly ceramic in nature, but refractory metals or carbon-based materials are also possible. These materials can be used in the form of long fibers or as small particles. In both cases, these materials have to possess a high microhardness and stiffness compared to the metal matrix [3].

The use of carbon-based materials such as carbon nanotubes (CNTs), graphene, fullerenes or nanodiamonds (NDs) as reinforcing phase in MMCs is a promising field of research mainly due to the superior mechanical properties such as the high strength of these materials [13, 14]. In the last two decades, the research on MMCs reinforced with carbon-based nanomaterials saw a growing number of publications, mainly focused on CNTs as reinforcement phase [15, 16]. Several publications were dedicated to giving an overview of the advantages and possible applications of these types of materials. In 2001, Thostenson et al. [17] provided

1.3. Deformation of nanocarbon-reinforced metal matrix composites by SPD

a review of the literature about the structure and processing of CNTs, as well as characterization and property modeling of CNTs and their composites. They showed that CNTs have a large potential as reinforcement of MMCs but that there are also significant challenges to overcome before this potential can be realized.

In 2010, Bakshi et al. [15] wrote a review about CNT-reinforced MMCs focusing on various processing techniques, strengthening mechanisms, interfacial phenomena, CNT dispersion and potential applications of CNT-reinforced MMCs. Radhamani et al. [16] assessed the progress and the future directions of the research on CNT-reinforced pure metals and steel, their production, properties and applications. Concentrating on individual metals reinforced by CNTs, Munir et al. [18] reviewed the production by powder metallurgy and the mechanical and thermal properties of CNT-reinforced Ti, and Miranda et al. [19] studied the ultra-high thermal conductivity applications of CNT-reinforced Al-MMCs.

The tribological properties of MMCs reinforced with carbon nanomaterials were reviewed by Dorri-Moghadam et al. [20] who looked at self-lubricating MMCs reinforced with CNTs and graphene as well as by Zhai et al. [21] as part of their more general overview of carbon nanomaterials in tribology, which also included the use of CNTs, NDs, graphene and fullerenes in coatings and as additives in lubricants. How analytical and numerical models can be used to evaluate and predict the mechanical behaviour of CNT-reinforced MMCs and what role the modelling of the CNTs (1D, 2D or 3D structure) plays, was compiled and reviewed by Imani-Yengejeh et al. [22].

1.3. Deformation of nanocarbon-reinforced metal matrix composites by SPD

A homogeneous distribution of the reinforcing carbon nanomaterials is the main challenge for these types of MMCs. SPD is one method to achieve this goal, and a number of different metals reinforced with carbon nanomaterials have been deformed by different SPD methods, mainly HPT, to improve the mechanical and

1. Introduction

the microstructural properties by homogenizing the second phase distribution and also by decreasing the grain size [5]. In Ni, reinforced with CNTs and deformed by HPT, the microstructural thermal stability was first investigated by Suarez et al. [23]. Within the scope of the research collaboration this work is a part of, the evolution of the microstructure [24], the structural defects of the CNTs [25], the reinforcement homogenization [26], the lattice defects and crystalline domain sizes [27], and the friction and tribo-chemical behaviour [28] of HPT-deformed Ni/CNT MMCs have been investigated by Aristizabal et al. For CNT-reinforced and HPT-deformed Cu, the grain refinement and microhardness increase compared to pure Cu, the thermal stability and the tensile strength were determined and presented in several publications [29–33]. Two other metals, for which the effect of CNT-reinforcement and HPT-deformation on the microstructure and the mechanical properties were evaluated are Al [34–37] and Ti [38].

CNTs are not the only carbon-based reinforcement phases, which were used for HPT-deformed MMCs. The influence of graphene was investigated in Ni [39], Al [40] and Cu [41], and fullerenes were used to improve the properties of Al [42–44]. The role of pure elemental carbon in strengthening of HPT-deformed Ni [45] and that of graphite in the case of Fe [46] has also been subject of investigations. Besides HPT, other SPD methods were also used to process nanocarbon-reinforced MMCs, for example Equal Channel Angular Pressing (ECAP) for CNT-reinforced Al [47, 48] and Cu [49], and Accumulative Roll Bonding (ARB) and related rolling techniques for CNT-reinforced Cu [50, 51] and Mg alloys [52, 53], and graphene-reinforced Al [54].

These publications all report an increase of the microhardness and/or the strength mainly caused by a grain refinement during the HPT-deformation process. In those cases, where the microstructural and mechanical properties of the nanocarbon-reinforced MMCs were compared to those of pure metals, the MMCs always showed higher microhardness/strength and smaller grain sizes due to the reinforcement phases acting as obstacles of grain boundary movement. The amount of reinforcing carbon nanomaterials on the other hand had a less significant influence on the material properties than their general presence or the temperature at which the

HPT-deformation process was conducted.

1.4. Motivation and aim of the work

The scope of this thesis was to investigate the evolution of the microstructural and mechanical properties of two different systems of nanocarbon-reinforced MMCs deformed by HPT, depending on the severity of the HPT-deformation, the amount of reinforcement phase material and the HPT-deformation temperature. A homogeneous distribution of the reinforcement phase is essential for a good mechanical performance of the MMCs and finding the right material and production parameters influencing this distribution is the main objective throughout this work.

With a homogeneous second phase distribution, MMCs are expected to have superior mechanical properties compared to pure metals and can be used for different applications where a better mechanical performance is needed. In 2010, Bakshi et al. [15] compiled a list with potential applications for CNT-reinforced MMCs, which could replace the more commonly used carbon fibre-reinforced MMCs. There are many possible applications for CNT-reinforced MMCs in the automobile, aerospace and space industry where high strength, low density, good wear resistance, good thermal and electric conductivity and a low coefficient of thermal expansion are needed. They could also be used for electronic applications, like sensors, batteries and electronic packaging where a high surface area, high current densities or reduced response times are important.

The motivation for using HPT-deformation in this work to improve the second phase distribution of the nanocarbon-reinforced MMCs stems from the possibility to apply large amounts of strains on the materials in a relatively simple manner. Both bulk materials and powders can be deformed to various degrees and at different temperatures, with the powders being pre-compacted and consolidated in the HPT. This distinguishes HPT-deformation from other processing techniques, such as powder extrusion or hot isostatic pressing, where creating a fully dense bulk material with a ufg or nc microstructure can be a difficult task [5,55].

1. Introduction

For the CNT and ND reinforcements used in this work, creating a homogeneous distribution primarily means overcoming the van der Waals forces between the individual particles. Besides using the shear forces occurring during HPT-deformation, the preparation methods were also chosen in regards to a dissolution of the agglomerates, either by using ultrasonication in the case of the nickel/carbon-nanotube (Ni/CNT) MMCs or ball-milling for the silver/nanodiamond (Ag/ND) MMCs.

2. Carbon-based Nanomaterials

Elemental carbon can exist in various forms, such as graphite or diamond, which are defined by the bonding states of their atomic orbitals. These carbon allotropes can either have an integer degree of carbon bond hybridization, a mixing of different hybridization states or a non-integer degree of hybridization. Diamond, graphite and carbyne have sp^3 , sp^2 and sp hybridized orbitals, respectively. Soot, carbon blacks, vitreous carbon and diamond-like carbon are examples for mixtures of different hybridization states. Closed-shell carbon structures like fullerenes (C_{60} , Bucky-balls), carbon onions or CNTs have non-integer hybridization states between 2 and 3. This fractional degree of hybridization is possible due to the curvature of their structures [13].

Another way to characterize carbon nanomaterials is their dimensionality, which has a significant influence on the chemical and electrical properties [13]. Small, dot-like carbon allotropes such as nanodiamonds and fullerenes are considered 0D due to their small size of less than 10 nm and their small aspect ratio. The molecular structure of the fullerenes gives them unusual optical properties, with possible applications as photoconductors, optical limiters or photorefractive materials [56]. CNTs with their high aspect ratio (small diameter, high length) are 1D, while graphene is a 2D monolayer of carbon atoms, arranged in a hexagonal pattern. Graphene is also the building block for both CNTs, when the monolayer sheet is rolled up into a tube, and graphite, when several sheets are stacked upon each other [57]. Such bulk forms of carbon, like graphite or macroscopic diamonds, are classified as 3D.

2.1. Carbon Nanotubes

Carbon nanotubes (CNTs) were first described by Iijima in 1991 [58]. He reported the production of graphitic needle-like tubes by arc-discharge evaporation of carbon in an argon-filled vessel. These needles had a diameter between 4 and 30 nm, were up to 1 μm long and consisted of several layers of graphitic sheets, rolled up into concentric tubes. The individual layers were separated by a distance of 0.34 nm, similar to the distance between the layers of bulk graphite.

These kinds of CNTs, consisting of multiple concentric graphene layers are called multi-walled carbon nanotubes (MWCNTs) in contrast to those consisting of only one rolled-up sheet of graphene, which are called single-walled carbon nanotubes (SWCNTs). SWCNTs have diameters of around 1 nm, while MWCNTs can be much larger with diameters between 10 and 100 nm [57].

CNTs have exceptionally good mechanical and thermal properties. Their sp^2 bond is 33% stronger than that of diamond (sp^3), and their tensile strength is as high as that of graphene, while their shape also provides high compression strength. The Young's modulus of nanotube bundles is larger than 1 TPa, which is especially interesting for CNT-reinforced composites. The thermal conductivity of CNTs in axial direction is higher than that of diamond, because of the 1D structure that strongly limits scattering processes. They also remain stable up to 4000 K, the melting point of graphite, due to thermal contraction in length at temperatures of several hundred degrees Celsius. Only at higher temperatures does thermal expansion occur. [14].

Of great importance for the electrical properties of CNTs is their structural symmetry. Depending on how the graphene sheet, depicted in Figure 2.1, is rolled up, the chiral angle θ of the CNTs changes between 0 and 30°. CNTs with $\theta = 0^\circ$ are called "zigzag", with $\theta = 30^\circ$ "armchair" and with $0 < \theta < 30^\circ$ "chiral" (Figure 2.2). The chiral vector C_h is defined by the integers (n,m), which determine θ and the CNT diameter d_t , and the basic vectors of the graphene honeycomb lattice. If the difference $n - m$ is a multiple of 3, the CNTs are metallic, otherwise

they become semiconducting (Figure 2.1). With CNTs it is therefore possible to have different modes of conduction without the necessity of doping. [59]

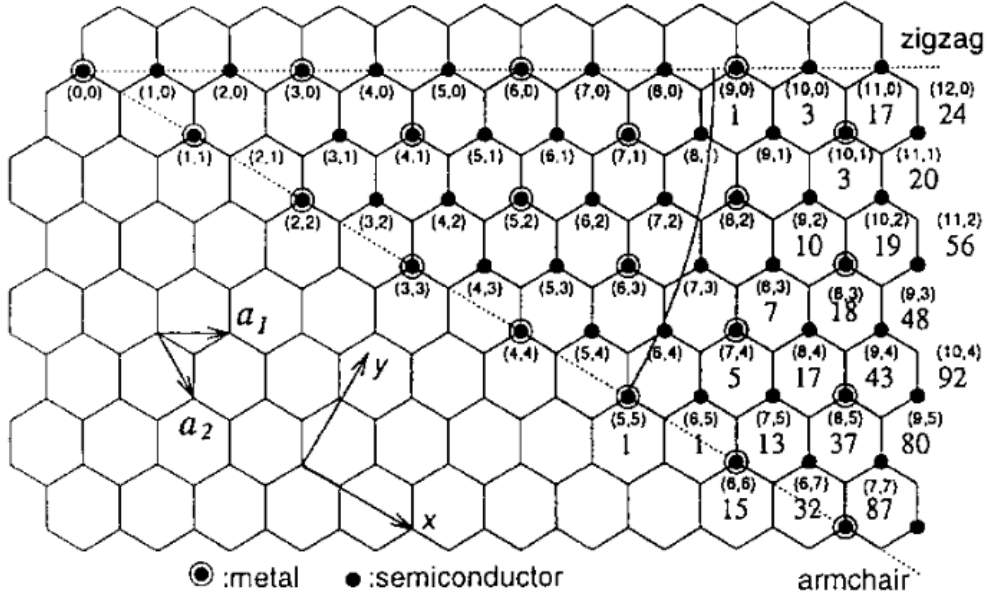


Figure 2.1.: The 2D graphene sheet is shown along with the vector which specifies the chiral nanotube. The pairs of integers (n, m) in the figure specify chiral vectors C_h for carbon nanotubes, including zigzag, armchair, and chiral tubules. Below each pair of integers (n, m) is listed the number of distinct caps that can be joined continuously to the cylindrical carbon tubule denoted by (n, m) . The circled dots denote metallic tubules and the small dots are for semiconducting tubules [59].

CNTs are of great interest as second phase materials in MMCs, since their superior mechanical and thermal properties can increase the tensile strength, microhardness and thermal stability of the matrix material. An increase of the elastic modulus of the composites is also possible with CNTs. On the other side, CNTs tend to form large agglomerates through attractive van der Waals forces due to their high surface area. This agglomeration can cause a deterioration of the mechanical properties of the material. Thus, a homogeneous distribution and a dissolution into smaller agglomerates or single CNTs is essential for homogeneous mechanical properties of the composites [15].

2. Carbon-based Nanomaterials

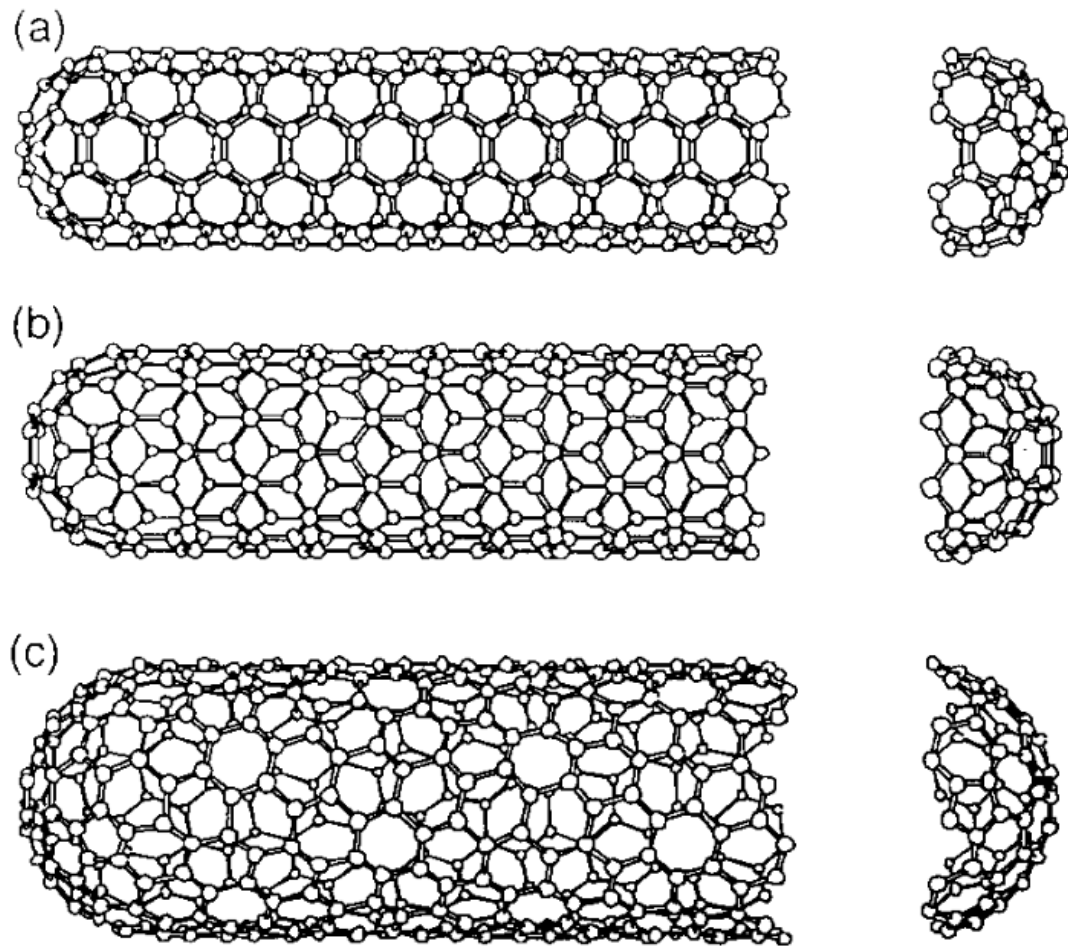


Figure 2.2.: By rolling up a graphene sheet (a single layer of carbon atoms from a 3D graphite crystal) as a cylinder and capping each end of the cylinder with half of a fullerene molecule, a “fullerene-derived tubule”, one layer in thickness, is formed. Shown here is a schematic theoretical model for a single-wall carbon tubule with the tubule axis OB normal to: a) the $\theta = 30^\circ$ direction (an “armchair” tubule), b) the $\theta = 0^\circ$ direction (a “zigzag” tubule), and c) a general direction B with $0 < \theta < 30^\circ$ (a “chiral” tubule). The actual tubules shown in the figure correspond to (n,m) values of: a) $(5,5)$, b) $(9,0)$, and c) $(10,5)$ [59].

2.2. Nanodiamonds

Nanodiamonds (ND), also known as ultra-dispersed diamonds (UDD), are particles with a diamond-like atomic structure (sp^3 hybridization) and a size between 4 and 6 nm (Figure 2.3). The physical properties of such small particles are strongly affected by adsorbed atoms, molecules and functional groups due to the large percentage of atoms present on the surface (about 50 % of all atoms). The diamond core on the other hand is chemically inert. Due to their large surface to volume ratio, they also show a strong predisposition to stick together and form larger agglomerates [13].

NDs are mainly produced by detonation of carbon-containing explosives and subsequent purification of the detonation soot. The utilized explosives are TNT and hexogen, and have a negative oxygen balance to provide free, nonoxidized carbon. During the detonation, thermodynamically stable conditions for the formation of diamonds (pressures of 20 to 30 GPa, temperatures of 3000 to 4000 K) are present. To prevent a transformation of the NDs into graphite, a high cooling rate of at least 3000 K/min are needed. There are other methods used to produce NDs, like grinding of natural diamond or Laser-assisted synthesis, but the detonation route is the most effective both in production scale and particle size [60].

The detonation soot contains between 50 and 65 wt% NDs, 35 to 45 wt% graphite-like structures and 1 to 5 wt% impurities. The purification of the NDs is done by thermal oxidation with nitric acid under pressure to separate the diamond phase. After purification, the material consists of 90 to 97 % NDs and 3 to 10% non-diamond carbon.

With their small size, a high microhardness and thermal stability, NDs can be used as reinforcements for composites to improve scratch and impact resistance as well as thermal stability and thermal conductivity. They can also be used in colloidal solutions for metallographic polishing or as lubricants. Functional coatings can likewise be improved by the addition of NDs [60]. The strong agglomeration of the NDs is detrimental for utilization of the superior microhardness of diamond

2. Carbon-based Nanomaterials

in MMCs, which makes the dissolution of the agglomerates and the homogenous dispersion of the particles in the matrix the main goal for the production of ND reinforced MMCs [61]. The spherical shape of the NDs and the sp^3 hybridization are helpful in this regard, as they are better dispersible both in liquid solvents and in metal matrix materials than other carbon-based materials such as CNTs with their long fiber-like shape [62].

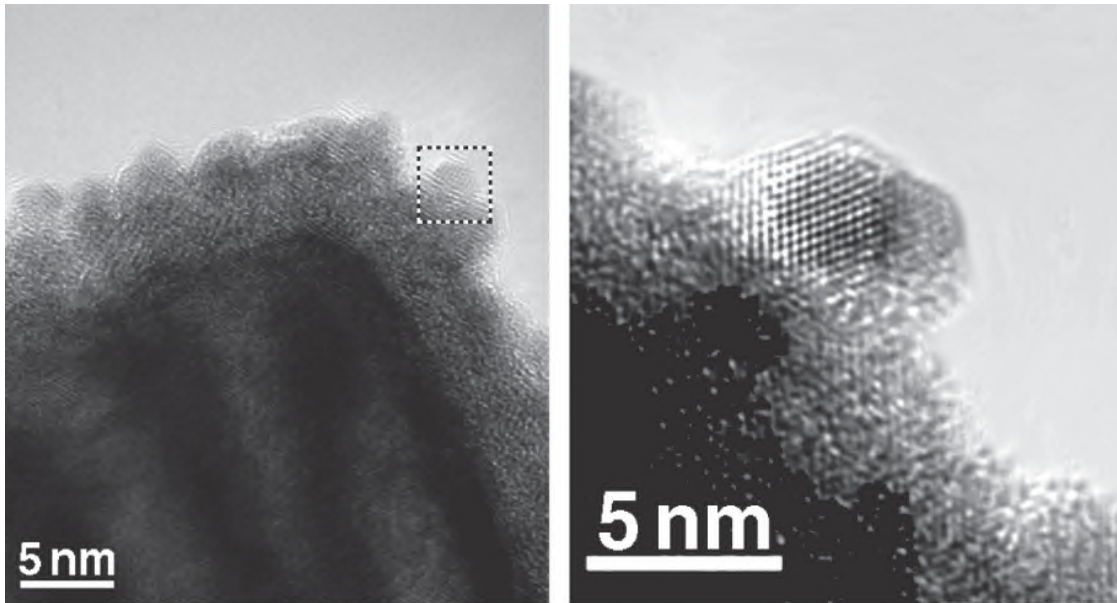


Figure 2.3.: HRTEM images of ultradispersed diamond particles obtained by explosive detonation synthesis [13].

3. Microstructural evolution of nickel/carbon nanotube composites deformed by HPT

3.1. Experimental

Ni/CNT MMCs used in this work were produced via colloidal mixing from Ni dendritic powder (Alfa Aesar, -325 mesh) and Multiwall CNTs (Graphene Supermarket, USA, purity > 95%, individual particle diameter of 20–85 nm, mean length between 5-15 μm) with final CNT weight percentages of 0.1, 0.25, 0.5, 1, 2, and 3. These weight percentages correspond to volume percentages of 0.42, 1.04, 2.08, 4.17, 8.33, and 12.5. For the mixing process, which is thoroughly described in ref. [62], the CNTs were dispersed in ethylene glycol using a homogenizer and an ultrasonic bath. The Ni powder was then added to the dispersion and further homogenized. After evaporating the solvent, the powder was pressed and sintered in a hot uniaxial press in vacuum [62]. The final composite samples had a diameter of 8 mm and a height of about 1 mm.

HPT-deformation was done at a pressure of 7.5 GPa and a velocity of 0.2 revolutions per minute for experiments at RT and 0.6 revolutions per minute for experiments at elevated temperatures. At RT, the number of HPT-revolutions was step-wise increased from 1 to 10, 20 and 30 revolutions for all CNT contents. HPT-deformations at elevated temperatures were done for 30 revolutions at 200°C, 300°C and 400°C. Also, a two-temperature deformation process was utilized with 30 revolutions at 400°C and subsequent 10 revolutions at 200°C.

3. Microstructural evolution of nickel/carbon nanotube composites deformed by HPT

The HPT-deformed samples were cut in half and embedded in resin to investigate the microstructure with a scanning electron microscope (SEM) type LEO 1525 in tangential direction along the radius. For TEM investigations, plain view TEM samples were prepared from HPT samples to examine the region around 2 mm from the center in axial direction as outlined in Figure 3.1. The selected samples had 1 wt% CNT content, HPT-deformed at RT for 30 revolutions as well as 2 wt% CNT content, HPT-deformed for 30 revolutions at 200°C, 300°C and 400°C and for 40 revolutions with the two-temperature process. A Phillips CM12 TEM was used for the standard TEM investigations, and a JEOL 2100F TEM equipped with a CS corrector for high-resolution imaging (HRTEM).

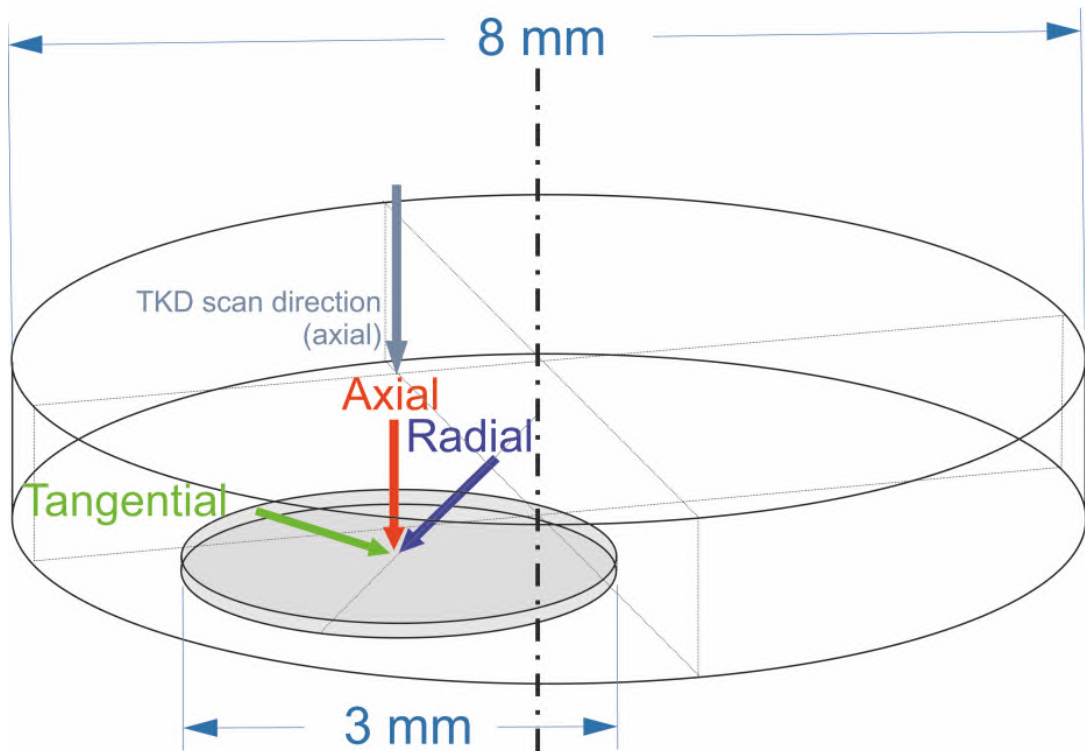


Figure 3.1.: Schematic of the HPT disc with the position of the TEM sample marked with principle viewing directions and TKD scan direction.

A scanning electron microscope (SEM) type LEO 1525 equipped with a Bruker

3.2. Parameters influencing the microstructure

QUANTAX EBSD analysis system was utilized for transmission Kikuchi diffraction (TKD) [63]. The number of TKD scans taken from the samples with 2 wt% CNTs, HPT-deformed at 200°C, 300°C, 400°C and 400 + 200°C were 6, 5, 1 and 3, respectively. Scans were taken in axial direction as for the TEM samples, as indicated in Figure 3.1. A maximum misorientation angle of 15° and a minimum grain size of 5 pixels were used for identification of single grains. Data acquisition and grain size analysis were performed with the program Bruker Esprit version 2.1 [64], pole figures and inverse pole figures were evaluated with the program OIM Analysis version 5.31 [65].

To investigate the thermal stability of the synthesized composites, HPT samples deformed at 200°C and 400 + 200°C were annealed at 500°C for 3h in a vacuum furnace. The specimens were heated and cooled within the vacuum furnace. After embedding in resin, the microstructure of the specimens was examined with SEM and compared to the microstructure of non-annealed samples. Additional TEM samples were produced analogous to the as-deformed samples (Figure 3.1).

3.2. Parameters influencing the microstructure

Three main parameters have been found to influence the microstructural evolution of the Ni/CNT MMCs and will be described in the following sections.

3.2.1. Equivalent strain

The first parameter is the amount of equivalent strain that is subjugated on the sample. The equivalent strain during HPT-deformation can be modeled as a simple shear strain [66] and is defined as

$$\epsilon_{eq} = \frac{2 * \pi * r}{t * \sqrt{3}} * n \quad (3.1)$$

with r the radius of the sample, t the thickness of the sample and n the number of HPT revolutions. According to this equation, the strain in the center of the HPT samples should be zero and increasing linearly with the radius [4]. As the

3. Microstructural evolution of nickel/carbon nanotube composites deformed by HPT

diameter of all samples is 8 mm and the sample thicknesses vary only slightly, the number of HPT-revolutions is the main factor to determine the equivalent strain.

With an increasing equivalent strain, the material experiences severe microstructural changes. To give an example for the microstructural evolution of the Ni/CNT MMCs, Figure 3.2 shows SEM images at a radius of 3 mm of the Ni/CNT MMCs with 1wt% CNTs HPT-deformed at RT for 1, 10, 20 and 30 revolutions. The size and the distribution of the CNT agglomerates does not significantly change with increasing number of revolutions, while the grain sizes of the Ni matrix decreases from 161 ± 35 nm in diameter for 1 revolution to 56 ± 11 nm for 30 revolutions.

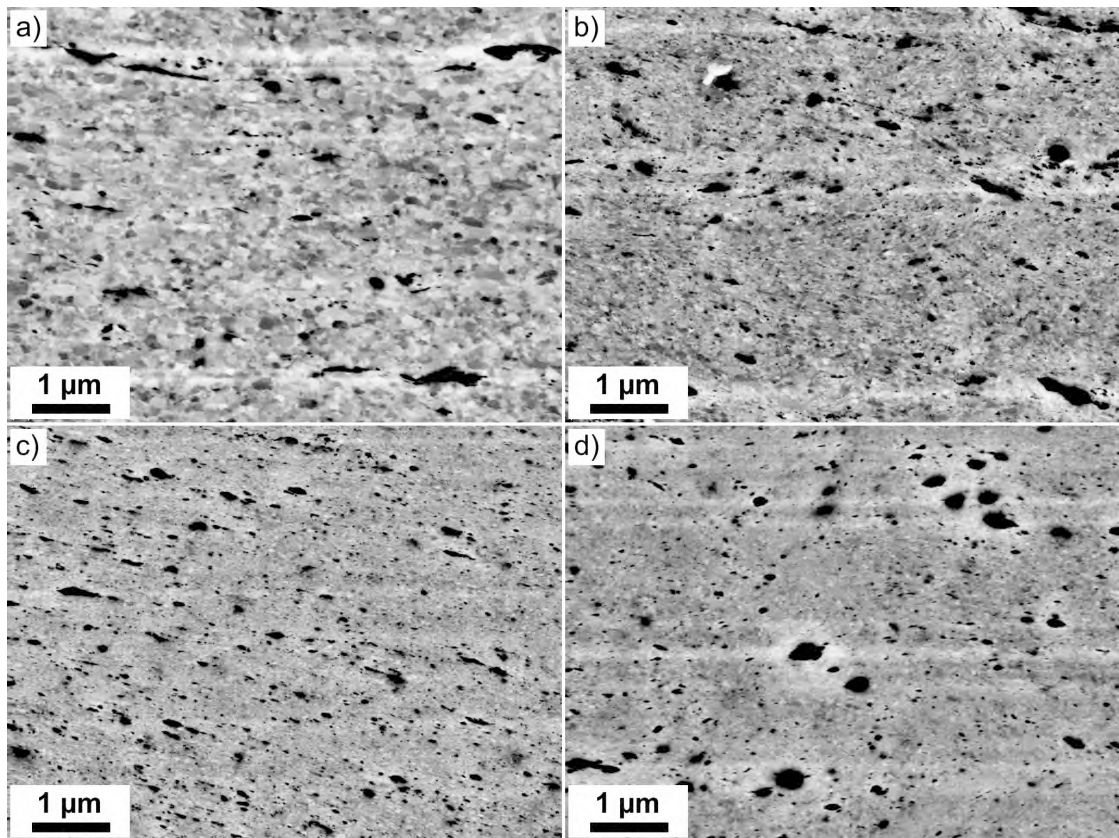


Figure 3.2.: Microstructure of Ni/CNT MMC with 1 wt% CNT, HPT-deformed at RT for a) 1 revolution, b) 10 revolutions, c) 20 revolutions and d) 30 revolutions (redrawn from publication A).

3.2. Parameters influencing the microstructure

As these grain sizes are very small given the resolution of the SEM images, especially for the sample HPT-deformed for 30 revolutions (Figure 3.2 d), TEM specimens of this sample were produced as outlined in Figure 3.1 to give a better estimate of the grain sizes. Figure 3.3 shows the Ni grain structure both as a bright field and a dark field image as well as the corresponding SAD pattern. Grain size measurements of these TEM images revealed a mean grain diameter of 41 ± 17 nm, which is in relatively good agreement with the value obtained from the SEM image.

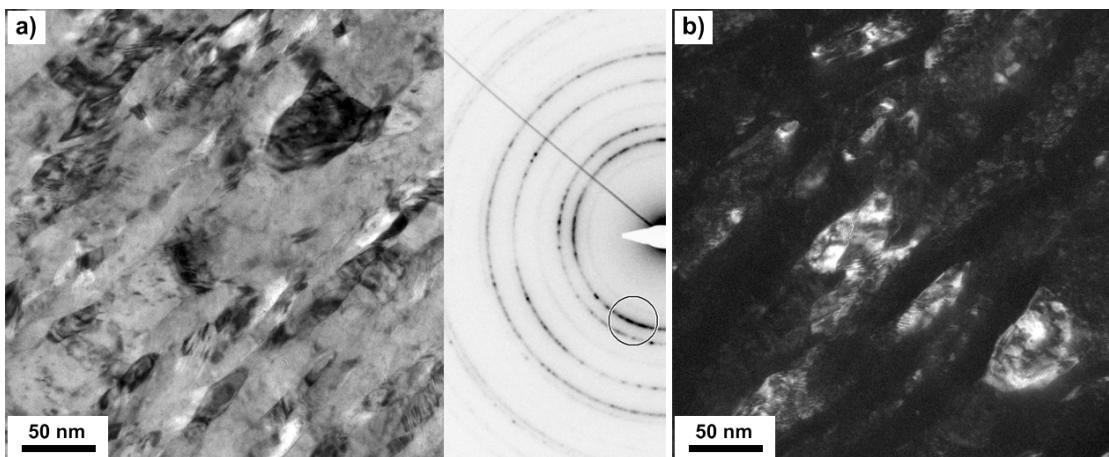


Figure 3.3.: a) Bright field TEM image with corresponding SAD pattern and b) dark field TEM image of Ni MMCs with 1wt% CNTs after 30 revolutions at RT ($r = 2$ mm) (redrawn from publication A).

The fragmentation of the microstructure through HPT-deformation of metals is a well-known phenomena [4]. At lower strains dislocations are generated in the material, which are concentrated into boundaries and not randomly throughout the microstructure. These boundaries subdivide the initial grains and with increasing strain the misorientation of the sub-grains increases and a new, finer microstructure develops. The grain fragmentation saturates at large strains where the grain size does not change with further deformation due to an equilibrium between the generation of dislocations and boundaries and their annihilation [67]. The sat-

3. Microstructural evolution of nickel/carbon nanotube composites deformed by HPT

uration grain size and the equivalent strain value necessary to reach saturation depend on several parameters, like the presence of impurities or alloys and the HPT-deformation temperature [4].

3.2.2. Second phase content

The second factor influencing the microstructure is the amount of reinforcement phase in the MMCs. In this work, Ni samples with CNT contents between 0.1 and 3 wt% were used to get an overview over a range of different CNT concentrations. More than 3 wt% were not used, as a previous study has shown that there is no additional reinforcing effect due to the strong reagglomeration of the CNTs [68].

The microstructural evolution depending on the CNT content was evaluated by comparing Ni/CNT samples with increasing CNT content, all HPT-deformed for 20 revolutions at RT (Figure 3.4). The 3 wt% sample (Figure 3.4 f) was only deformed to 2.5 revolutions, as a higher deformation was not possible due to slipping of the sample between the anvils. With increasing CNT content, the size and density of the CNT agglomerates increase. Especially with CNT contents of 2 and 3 wt% (Figures 3.4 e and f) large agglomerates, up to 1 μm long, are present. The Ni grain sizes on the other hand show no significant differences between the samples, although a thorough evaluation of the grain sizes would have to be conducted by TEM studies for all CNT contents similar to those shown in Figure 3.3 for 1 wt%.

A smaller saturation grain size than in pure metals can be achieved in MMCs, due to the reduction in grain boundary mobility by the second phase particles present at the grain boundaries and triple junctions [4]. A similar result was obtained by Rathmayr and Pippan [45] by comparing the saturation microstructures of HPT-deformed Ni with 8 and 600 ppm carbon content, where the samples with more carbon showed a smaller grain size than those with less carbon, independent of the HPT-deformation temperature. The finest microstructure for these materials was observed in Ni with 600 ppm carbon, HPT-deformed at liquid nitrogen temperature ($-196^{\circ}C$), with an average grain size of about 50 nm. This is about the same grain size as in the Ni/CNT MMCs, HPT-deformed at RT. The reason

3.2. Parameters influencing the microstructure

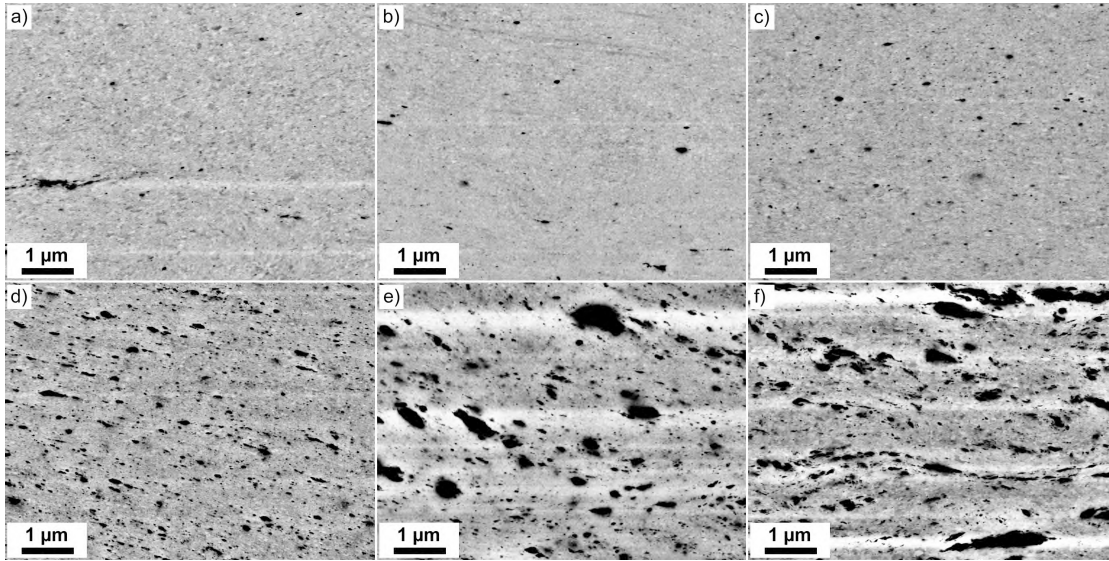


Figure 3.4.: Microstructure of Ni/CNT MMC, HPT-deformed for 20 revolutions at RT with a) 0.1 wt%, b) 0.25 wt%, c) 0.5 wt%, d) 1 wt%, e) 2 wt% and f) 3 wt% CNT content (for 3 wt% only 2.5 revolutions).

for the similar grain sizes between the different CNT concentrations is probably the fact that at higher concentrations most of the CNTs are accumulated in agglomerates, which are much larger than the Ni grain size (c.f. Figures 3.4 e and f). Therefore, the amount of CNTs present at the individual grain boundaries and triple junctions does not significantly increase with the overall CNT content.

3.2.3. HPT-deformation temperature

The last influencing factor for the microstructural evolution during HPT-deformation is the deformation temperature. Increasing the HPT-deformation temperature is known to increase the saturation grain size [4]. This thesis aims to show how this temperature increase will affect both the matrix grain size and the size and distribution of the CNT agglomerates.

To evaluate the influence of the HPT-deformation temperature on the microstructure, Ni/CNT MMC samples were deformed for 30 revolutions at 200°C, 300°C and 400°C. Figure 3.5 exemplarily shows the microstructural change for the 2wt%

3. Microstructural evolution of nickel/carbon nanotube composites deformed by HPT

Ni/CNT composite. HPT-deformation at 200°C results in large, irregular CNT agglomerates, imbedded inhomogenously in a nanograined Ni matrix (Figure 3.5 a). Increasing the HPT-deformation temperature to 300 and 400°C (Figures 3.5 b and c, respectively) leads to an increase in the Ni matrix grain size, a decrease in the size of the CNT agglomerates and a homogenization of the CNT distribution in the matrix.

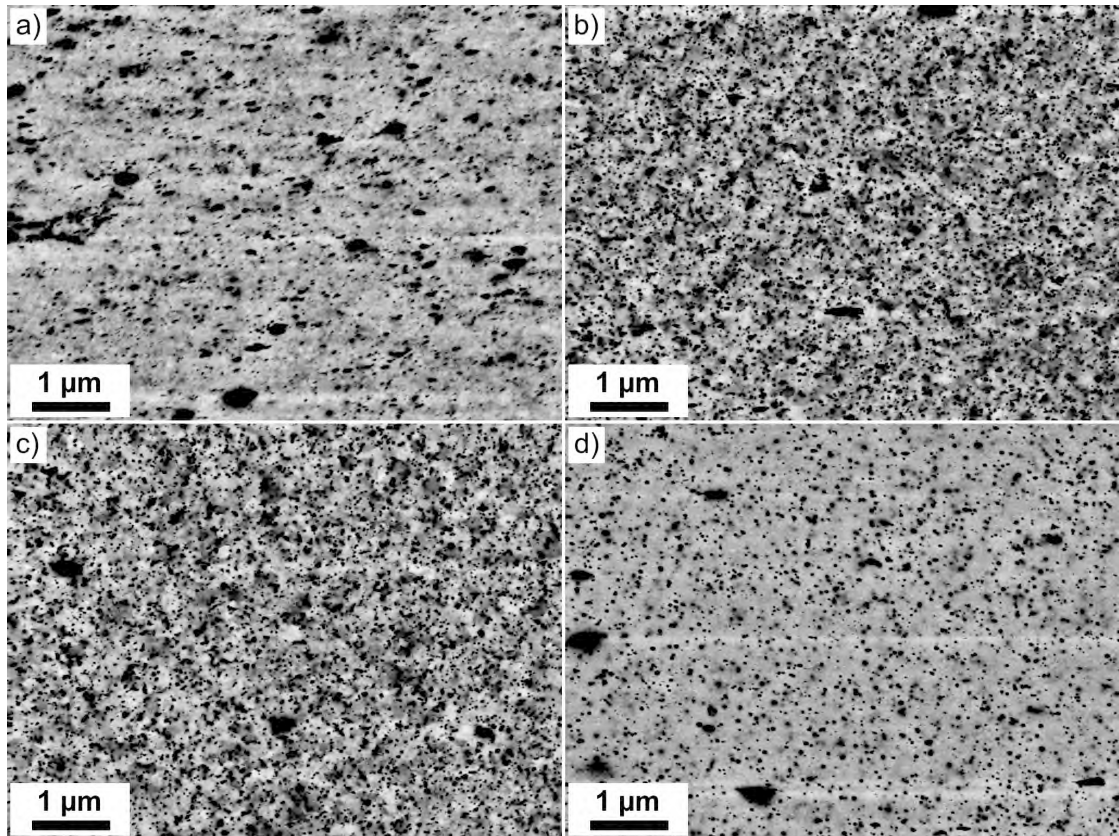


Figure 3.5.: Microstructure of Ni/CNT MMC with 2 wt% CNT, HPT-deformed for 30 revolutions at a) 200°C, b) 300°C, c) 400°C and d) for 40 revolutions at 400 + 200°C (redrawn from publication B).

To optimize the microstructure, a two-temperature deformation process has been developed by first deforming the MMCs at 400°C to decrease the agglomerate size and improve their distribution and then further deform the material at 200°C to

3.2. Parameters influencing the microstructure

decrease the Ni matrix grain size. Figure 3.5 d shows that this two-temperature HPT-deformation process was successful, resulting in a Ni matrix with grain sizes smaller than 100 nm and mostly small, homogeneously distributed CNT agglomerates. Some larger agglomerates are still present in this sample due to the high amount of CNTs. The other CNT concentrations showed similar results after HPT-deformations at the same temperature values.

TEM images of CNT agglomerates were taken at medium magnification to evaluate their distribution inside the Ni matrix and at high magnifications to determine their internal structure and to investigate the interface structure between CNTs and Ni. Figure 3.6 shows selected images for each HPT-deformation temperature to illustrate the influence of the temperature on the size, shape and distribution of the agglomerates. After deformation at 200°C, many of the agglomerates are irregularly shaped and poorly distributed (indicated by arrows in Figure 3.6 a). They consist of many MWCNT fragments, sticking together with no preferred orientation (Figure 3.6 b). The interface between matrix and agglomerates shows a good bonding of the phases without apparent voids. In the samples deformed at 300°C and 400°C, the CNT agglomerates are smaller and more homogeneously distributed in the matrix, compared to the 200°C sample (indicated by arrows in Figures 3.6 c and e). The shape of the agglomerates is mostly elliptical with the CNT-wall fragments inside resembling this shape, creating a fingerprint-like structure (Figure 3.6 d and f). The interfaces are equally well-defined as in the 200°C sample. In the two-temperature sample (400 + 200°C), the distribution and the size of the CNT agglomerates are comparable to those in the 300°C and 400°C samples (indicated by arrows in Figure 3.6 g). The internal structure also shows the fingerprint-like distribution of CNT fragments (Figure 3.6 h). The shape of the agglomerates on the other hand is more comparable to those in the 200°C sample. Again, there are no visible voids at the interface between the two phases. The spacings between the individual layers have been measured with the program ImageJ [69] to be 0.37 ± 0.03 nm, 0.37 ± 0.03 nm, 0.44 ± 0.06 nm and 0.41 ± 0.05 nm for the samples HPT-deformed at 200°C, 300°C, 400°C and 400 + 200°C, respectively. These values are slightly larger than the 0.34 nm measured in pristine MWCNTs [58].

3. Microstructural evolution of nickel/carbon nanotube composites deformed by HPT

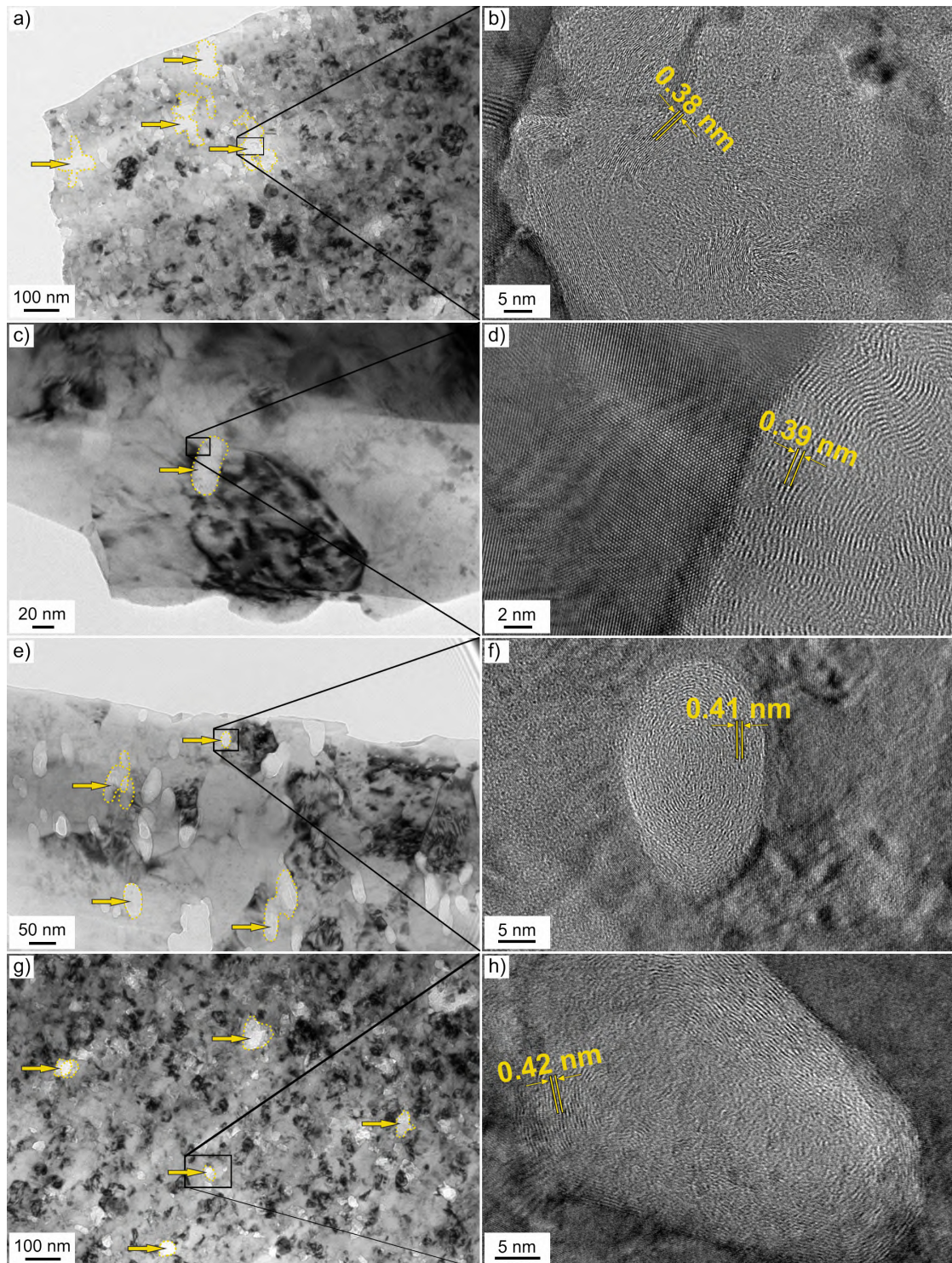


Figure 3.6.: TEM and HRTEM images of Ni with 2wt% CNTs HPT-deformed at a-b) 200°C, c-d) 300°C, e f) 400°C and g-h) 400 + 200°C. CNT agglomerates are marked by arrows on the left side and the spacing between the CNT layers is indicated on the right side.

3.2. Parameters influencing the microstructure

The HRTEM investigations showed a strong influence of the HPT-deformation temperature on the size, shape and distribution of the CNT agglomerates. Large, irregularly shaped agglomerates were found after HPT-deformation at 200°C and small ellipsoid ones at higher temperatures. The CNTs inside the agglomerates were broken into fragments and randomly oriented in the 200°C sample, with no discernable influence of the shear direction during HPT-deformation. With increasing HPT-deformation temperature, the orientation of the fragments resembled more the agglomerate shape. This fragmentation is in concordance with the results of a previous study of our group, which showed that irreversible damage to the CNTs is already introduced at low levels of strain [24]. During HPT-deformation, the CNTs undergo an amorphization trajectory following a model proposed by Ferrari et al. [70]. HPT-deformation up to 20 revolutions at room temperature does not however result in amorphization of the carbon, as can be seen in the Raman spectra of the CNTs, where the G band remains above values of 1580 cm^{-1} [24]. HRTEM images of the Ni/CNT MMCs investigated in this study (Figure 3.6) also show very little amorphization and mostly clusters of MWCNT fragments with typical interlayer spacing values of about 0.4 nm despite the strong HPT-deformation and high temperatures. CNT fragmentation with similar interlayer spacing as well as good bonding between the matrix and the CNTs was found in ball-milled and HPT-deformed Cu/CNT composites [30, 31, 33]. These findings suggest that it is not possible to use HPT-deformation to disperse CNTs in a metal matrix without damage or deformation, because large strains are necessary to create a homogenous distribution of small particles. In addition to the large strains, high HPT-deformation temperatures are needed for a homogeneous distribution of small CNT agglomerates, which further damages the CNTs and compacts the fragments into ellipsoid shapes (Figures 3.6 d and f).

Figure 3.7 shows exemplarily one TKD scan from each TEM sample of the Ni/CNT MMCs HPT-deformed at various temperatures. The scans were made at a radius of about 2 mm of the HPT samples, which corresponds to an equivalent strain between 300 and 500, where a saturation of the microstructure was reached. From an axial point of view, the Ni matrix consists of equiaxed grains, with the grain

3. Microstructural evolution of nickel/carbon nanotube composites deformed by HPT

sizes increasing with the HPT-deformation temperature (Figures 3.7 a, b and c) and again decreasing after the two-temperature deformation process (Figure 3.7 d). In these orientation maps, the crystal orientation of the grains is indicated by their color. The majority of the grains is oriented in [111]-direction along the axial direction of the HPT samples.

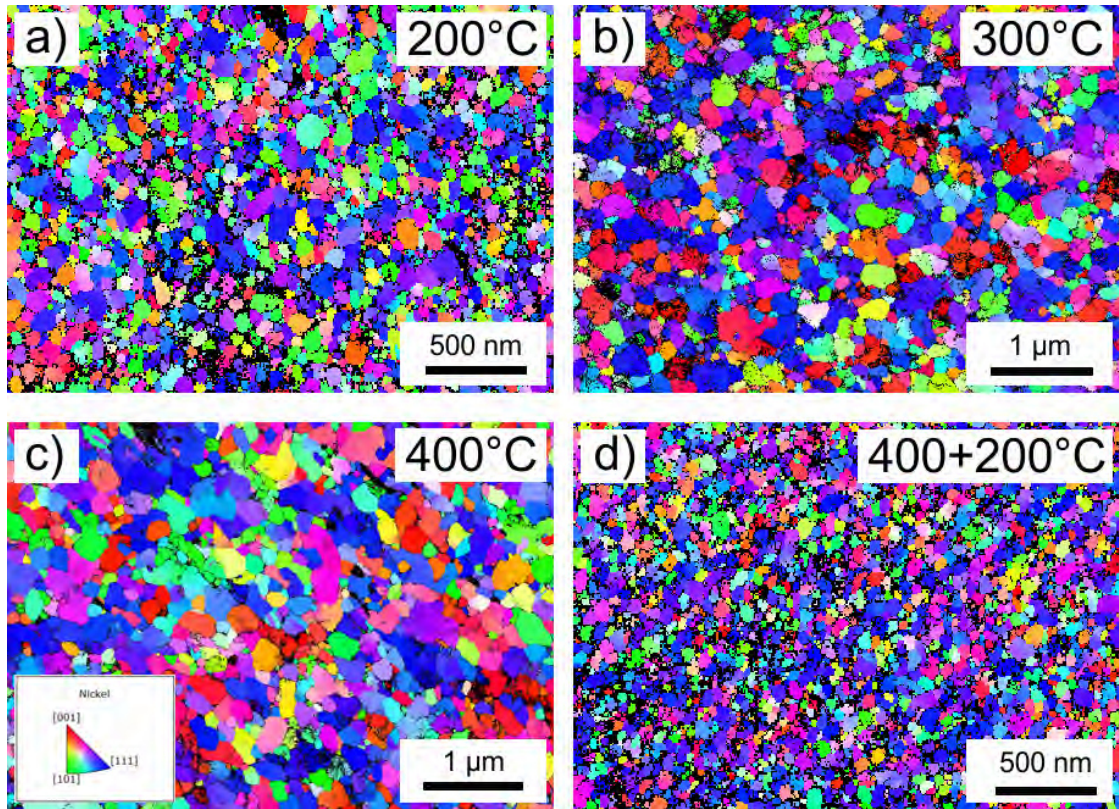


Figure 3.7.: Transmission Kikuchi diffraction scans showing grain orientation in axial direction of Ni with 2wt% CNTs HPT-deformed at a) 200°C, b) 300°C, c) 400°C and d) 400 + 200°C.

The grain sizes were measured from all TKD scans as the diameter of an equivalent circle and an area-weighted lognormal distribution was fitted on the data. Figure 3.8 shows the distributions for all HPT-deformation temperatures. The expectation value and the standard deviation of these fits as well as the number of measured grains for each deformation temperature are shown in Table 3.1. In-

3.2. Parameters influencing the microstructure

creasing the HPT-deformation temperature increases the average grain size, while the two-temperature deformation process results in similar grain sizes as the 200°C sample.

Table 3.1.: Average grain size, number of measured grains and saturation microhardness of 2 wt% Ni/CNT MMCs depending on the HPT-deformation temperature.

HPT-deformation temperature [°C]	Grain size [nm]	No. of measured grains	Saturation microhardness [HV0.3]
200	87 ± 50	4293	690 ± 39
300	293 ± 176	3361	497 ± 4
400	410 ± 290	1028	458 ± 8
400 + 200	100 ± 62	3274	790 ± 29

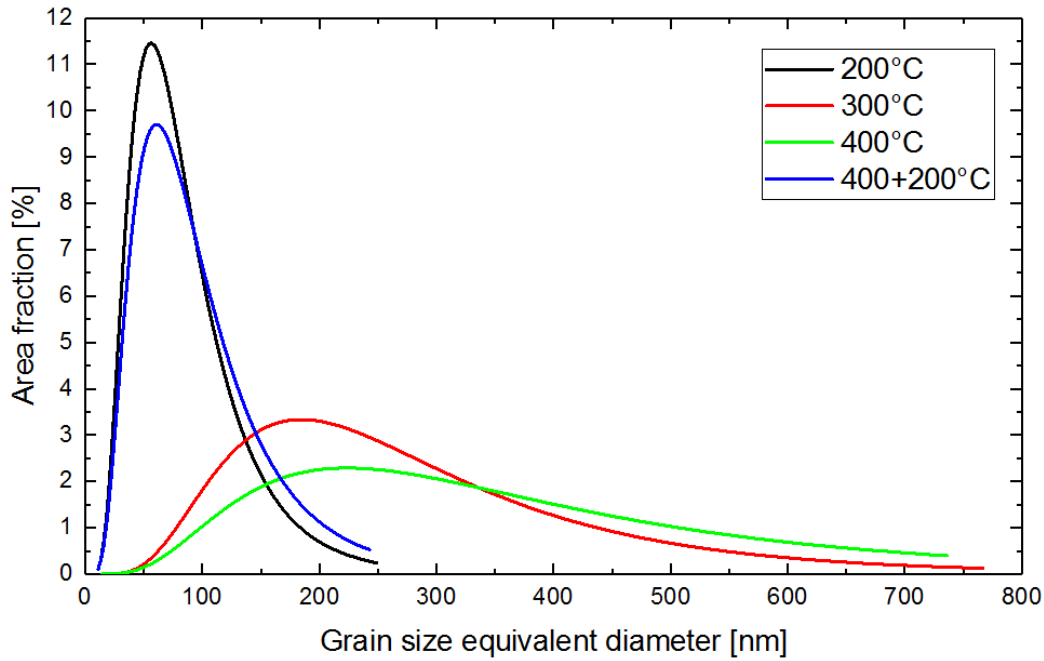


Figure 3.8.: Grain size distributions of Ni with 2wt% CNTs HPT-deformed at 200°C, 300°C, 400°C and 400 + 200°C.

3. Microstructural evolution of nickel/carbon nanotube composites deformed by HPT

Microstructures of HPT-deformed metals depend on the imposed strain, the presence of second phases and the deformation temperature [1]. Phipps et al. [71] showed that the grain size reduction during HPT-deformation saturates after a certain number of revolutions, depending on the temperature and the purity of the material. For the Ni/CNT MMCs investigated by TKD, the main factor for the measured grain size differences is the HPT-deformation temperature. All samples have the same material composition (2 wt% CNTs) and besides the two-temperature sample were also deformed to the same number of revolutions where microstructural saturation was reached (30 and 40, respectively). Higher temperatures during HPT-deformation of 300°C and 400°C resulted in a three and five times larger grain size, respectively, than in the sample HPT-deformed at 200°C (Table 3.1). The two-temperature deformation process with 200°C being the second processing temperature resulted in similar grain sizes as the deformation at 200°C alone, indicating that the second and lower HPT-deformation temperature determines the final grain size.

3.3. Texture evolution

(111)-pole figures were first recorded in axial direction, corresponding to the TKD scan direction, for all investigated HPT-deformation temperatures. To confirm that the texture corresponds with that of shear-deformed fcc metals, as described in Ref. [72], and especially to that of pure Ni [73], the viewing direction of the pole figures was rotated into the shear plane of the HPT samples and aligned with its radial direction. This was done to finally depict and compare the texture in radial direction (Figure 3.9). The resulting six-pointed stars, visible in the pole figures, are in good concordance with the pole figure of initially single crystalline Ni HPT-deformed to an equivalent strain of 32, where the now poly-crystalline Ni structure is saturated, and recorded in radial view (Figure 10 (i) in Ref. [73]). All samples have similar textures, with the texture of the sample deformed at 200°C (Figure 3.9 a) being less distinct than the other three. The distribution of the texture orientations is depicted in the inverse pole figures (Figures 3.9 e-h). All four samples show a concentration of grains orientated in the [111]-direction, with

the 200°C sample (Figure 3.9 e) having a less pronounced orientation distribution, which is in concordance with the grain orientation shown in Figure 3.7.

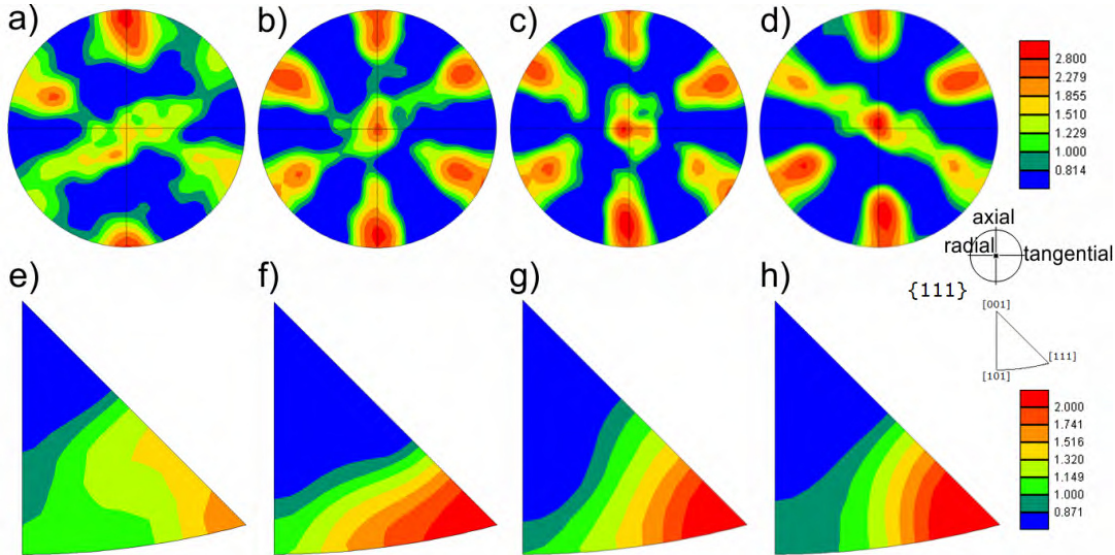


Figure 3.9.: (111)-pole figures in radial direction (a-d) and inverse pole figures (e-h) of Ni with 2wt% CNTs HPT-deformed at 200°C, 300°C, 400°C and 400 + 200°C, respectively.

Pole figures showed the same shear texture for each HPT-deformation temperature, while the inverse pole figures and the EBSD-scans showed the same distribution of grain orientations. This suggests that the imposed strain is the main factor determining the texture development and not the temperature. Ghosh et al. [74], on the other hand, found for HPT-deformed pure Ni additional texture components at deformation temperatures of 250°C and 400°C compared to deformation temperatures of -196°C and RT, where only the ideal deformation texture components were observed. However, an increase of the components angular spread with the temperature was found even before new texture components appeared. Further studies, using orientation distribution functions, have to be conducted, to determine if there is a similar temperature dependent spread of the texture in Ni/CNT MMCs and a shift of the appearance of new texture components to higher deformation temperatures compared to pure Ni. Hafok and Pippan [73] showed

3. *Microstructural evolution of nickel/carbon nanotube composites deformed by HPT*

for initially single-crystalline Ni that the initial [111]-orientation in axial direction is broken down through HPT-deformation into almost randomly oriented grains until a steady state of the grain size is reached. They also showed that the (111)-pole figure of severely deformed Ni develops a prominent six-pointed star when viewed in radial direction. This texture has been shown by Neale et al. [72] to result from shear strain imposed on rate-sensitive fcc metals. Comparable texture components in the pole figures of Ni/CNT MMCs (Figure 3.9) can therefore be attributed to the HPT-deformation of fcc Ni with no change of the texture due to the addition of CNTs. Similarly, no changes in the texture other than texture intensities were found in Mg/CNT and Al/CNT composites compared to the pure metals by Mokdad et al. [75] and Han et al. [76], respectively.

3.4. Post-deformation treatment: Annealing

The thermal stability of the microstructure of Ni/CNT composites with 2wt% CNT content HPT-deformed at 200°C and at 400 + 200°C was investigated by annealing at 500°C for 3 h in a vacuum furnace. These samples were chosen because of their similar small grain sizes in the as-deformed condition, but different second phase distributions. The microstructures of the as-deformed and of the annealed samples are shown in Figure 3.10. SEM and TEM images were taken at $r \approx 2$ mm from the center of the HPT discs. Figures 3.10 a and c show the sample HPT-deformed at 200°C, before and after annealing. Both the Ni grains and the CNT agglomerates grow relatively strong during annealing. The microstructures before and after annealing of the sample HPT-deformed at 400 + 200°C are shown in Figures 3.10 b and d. Here, the second phase particles are smaller and more homogeneously distributed. The annealed sample (Figure 3.10 d) shows a smaller increase of both grain size and agglomerate size compared to the annealed sample HPT-deformed at 200°C (Figure 3.10 c).

3.4. Post-deformation treatment: Annealing

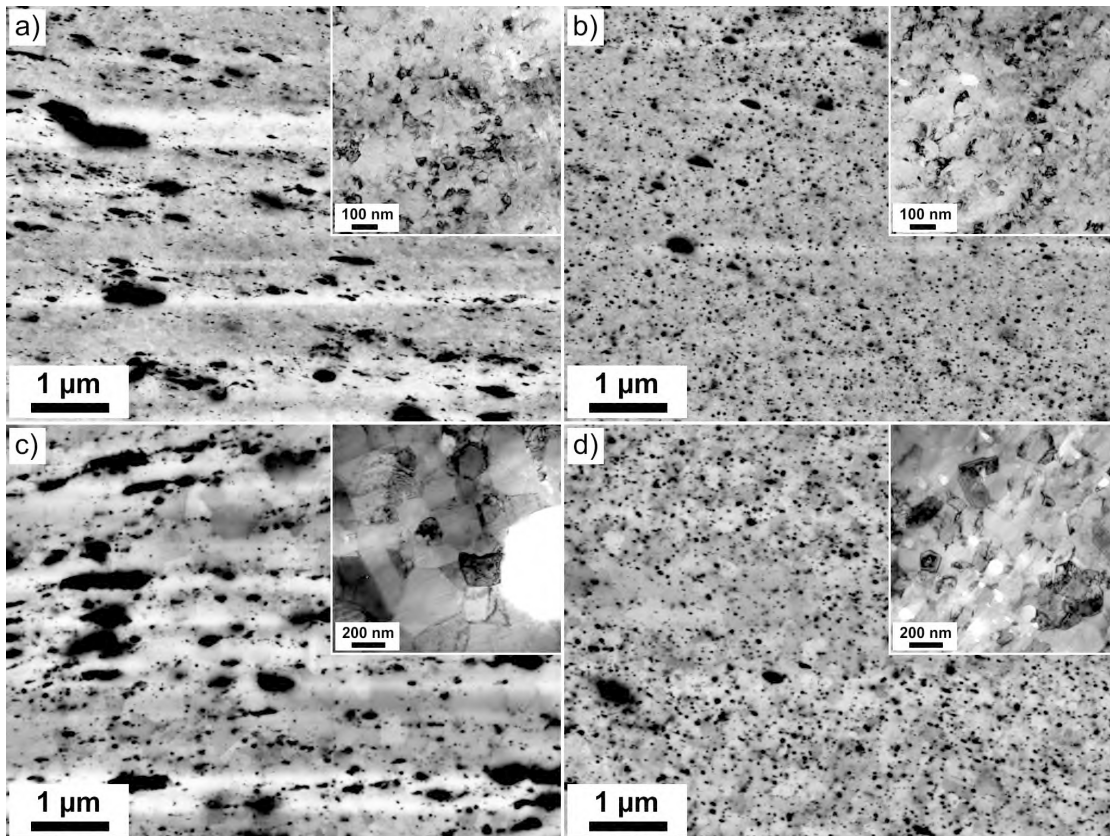


Figure 3.10.: Microstructure of 2 wt% Ni/CNT MMCs, HPT-deformed at various temperatures and annealed at 500°C for 3 hours: a) 200°C as-deformed, b) 400 + 200°C as-deformed, c) 200°C annealed and d) 400 + 200°C annealed.

4. Mechanical properties of nickel/carbon nanotube composites

Simultaneously with the microstructural development, the mechanical properties (microhardness, tensile strength, compression strength and ductility) of the HPT-deformed Ni/CNT MMCs also change with the number of revolutions, the CNT content and the HPT-deformation temperature. This chapter shows these developments for the same samples, which were investigated in Chapter 3 to give a comparison to the microstructural changes.

4.1. Experimental

For the microhardness measurements, the HPT-deformed samples were cut in half and embedded in resin to measure the Vickers microhardness in tangential direction with a Buehler Micromet 5100 using a load of 300 g (HV0.3). Measurements were done every 0.25 mm along the radius with three measurement points along the thickness of the samples, each. The Vickers microhardness is then drawn as a function of the equivalent strain ϵ_{eq} .

For the tensile tests, tensile test specimens were produced from HPT-deformed samples with a high-precision grinding machine. The processed specimens had a gauge length of 2.5 mm and a gauge diameter between 300 and 500 μm (Figure 4.1). Refs. [77, 78] give an overview of the specification of the grinding machine and the fabrication process. Tensile tests were then conducted with a Kammrath & Weiss tensile stage equipped with a 2 kN load cell and a testing velocity of 2.5 μms^{-1} at

4. Mechanical properties of nickel/carbon nanotube composites

RT. The tensile test setup and the evaluation software are thoroughly described in Ref. [77].

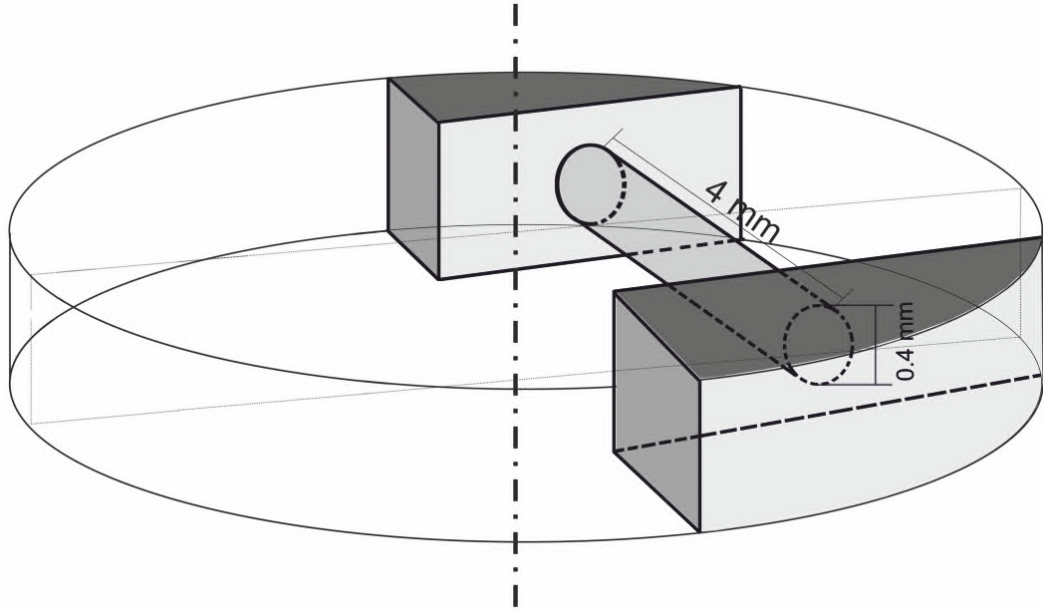


Figure 4.1.: Schematic of a tensile test specimen cut from an HPT disc.

To measure the compression strength and the mechanical anisotropy of the Ni/CNT MMCs, small cubes with side lengths of about 1 mm were cut and polished from HPT-deformed samples. Figure 4.2 shows the dimensions and the position of those cubes, as well as the testing directions. The compression tests were conducted in a Kammrath & Weiss tensile/compression module in axial, radial and tangential direction. A 10 kN loading cell was used to measure the compression forces, while a camera recorded the change of the specimen dimensions. The compression was conducted at RT with a constant velocity of $0.5 \mu\text{ms}^{-1}$. Data evaluation was done similar to the tensile tests.

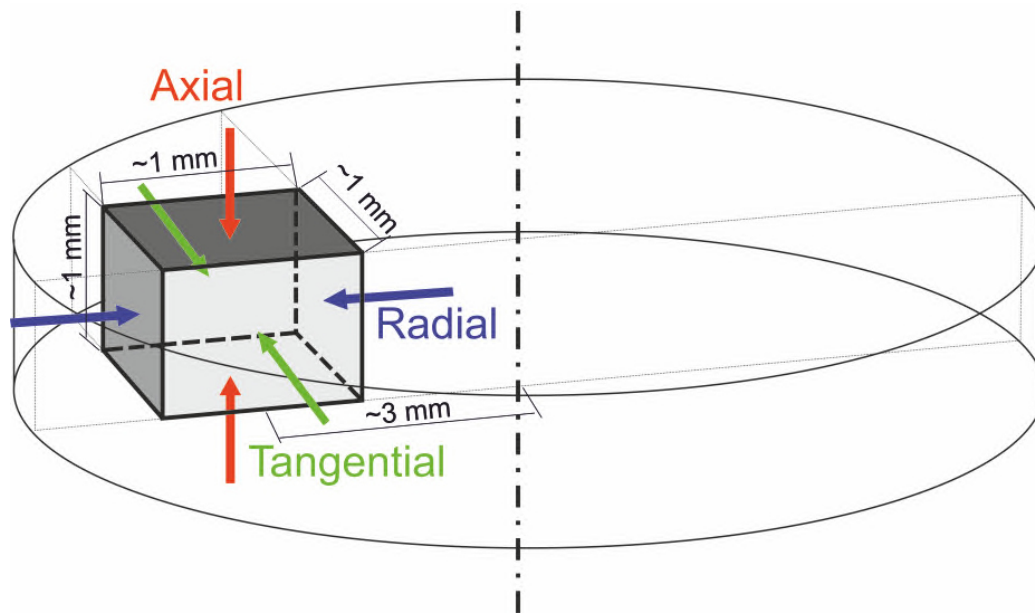


Figure 4.2.: Schematic of a compression test specimen cut from an HPT disc with the orientations of the acting forces in each test direction (redrawn from publication B).

4.2. Microhardness and tensile strength

With increasing numbers of HPT-revolutions/equivalent strain the microhardness of the Ni/CNT MMCs increases until it saturates at high strain values. This is exemplarily shown in Figure 4.3 for 1, 10, 20 and 30 revolutions of the Ni MMC sample with 1wt% CNTs. The rate of the microhardness increase slows down with increasing equivalent strain until after 30 revolutions it reaches a saturation microhardness of about 750 HV0.3 at an equivalent strain value of about 250.

Such high numbers of HPT-revolutions to reach a saturation of the microhardness are necessary due to the presence of the CNTs. For pure metals and single phase alloys a much lower strain is needed to reach the saturation regime, but the achievable microhardness is also lower than in MMCs [4, 79]. Another case where microhardness saturation is reached only after high equivalent strains is for HPT-consolidation and -deformation of powders due to the presence of oxide particles which act similar to reinforcements [80].

4. Mechanical properties of nickel/carbon nanotube composites

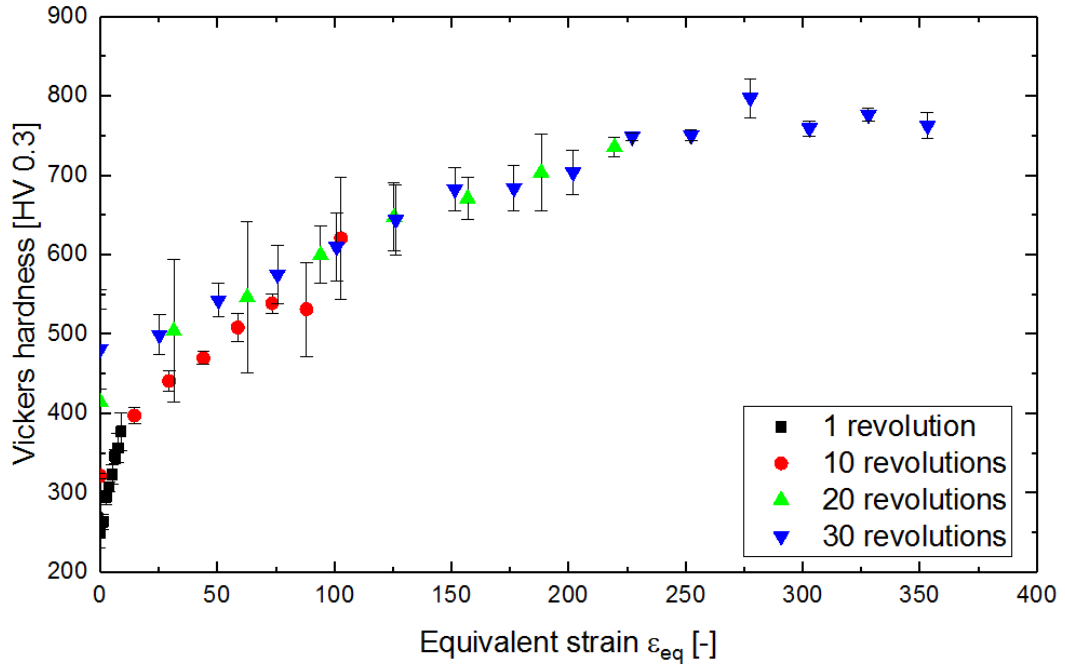


Figure 4.3.: Vickers microhardness as a function of the equivalent strain of Ni with 1wt% CNTs HPT-deformed for 1, 10, 20 and 30 revolutions (redrawn from publication A).

The CNT content has a less pronounced influence on the microhardness than the equivalent strain. As shown in Figure 4.4, all HPT-deformed samples reach saturation microhardness values above 700 HV after HPT-deformation for 20 revolutions at RT. The saturation onset was reached for all CNT concentrations at an equivalent strain of about 250. For the 3wt% CNT sample no steady state could be reached, as HPT-deformation at RT for more than 2.5 revolutions was difficult to achieve due to slippage of the sample between the anvils. This was probably caused by the combination of high microhardness and high CNT content, which decreases the friction coefficient [81].

The influence of the HPT-deformation temperature on the microhardness was investigated by deforming the Ni/CNT MMCs in the HPT at 200°C, 300°C and

4.2. Microhardness and tensile strength

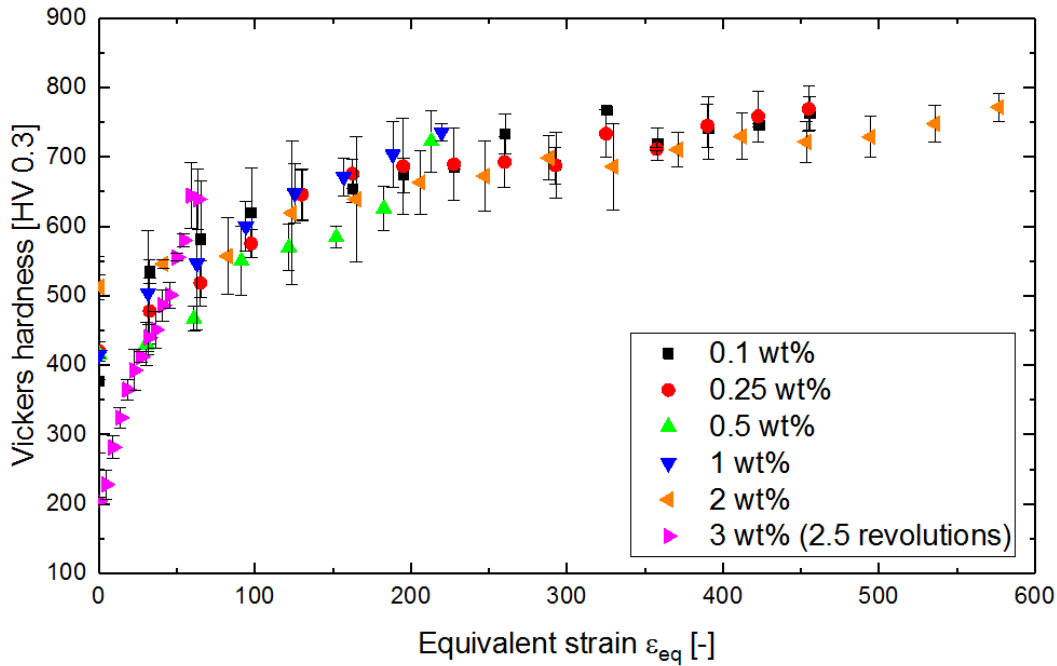


Figure 4.4.: Vickers microhardness as a function of the equivalent strain of Ni/CNT MMC, HPT-deformed for 20 revolutions at RT with 0.1 wt%, 0.25 wt%, 0.5 wt%, 1 wt%, 2 wt% and 3 wt% CNT content (for 3 wt% only 2.5 revolutions).

400°C as well as with a two-temperature process (400 + 200°C) which has been shown to provide both a small grain size and a homogeneous CNT distribution. The Vicker microhardness values of the Ni/CNT MMCs with 2 wt% CNTs, HPT-deformed at RT and at elevated temperatures are exemplarily shown in Figure 4.5.

After HPT-deformation for 20 revolutions at RT, a microhardness of 720 HV0.3 was reached. Increasing the HPT-deformation temperature to 200°C, 300°C and 400°C and the number of revolutions to 30 decreases the saturation microhardness values to 660, 500 and 460 HV0.3, respectively. It also decreases the equivalent strain necessary to reach saturation. The two-temperature process with 30 revolutions at 400°C and 10 revolutions at 200°C increases the microhardness to about 800 HV0.3 with a saturation onset at an equivalent strain of about 400.

4. Mechanical properties of nickel/carbon nanotube composites

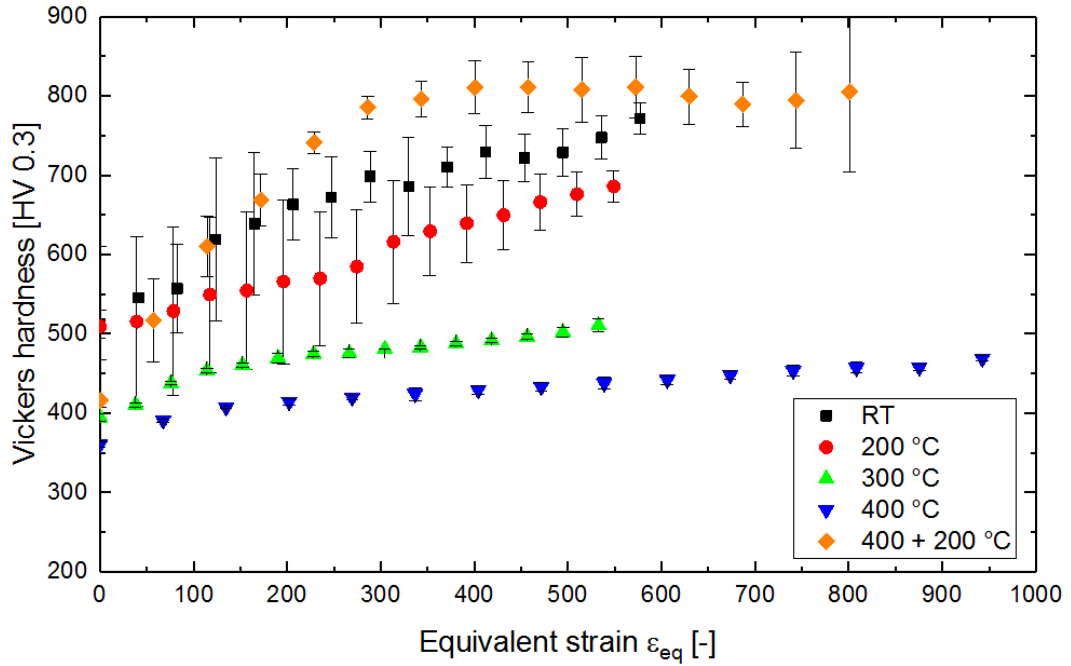


Figure 4.5.: Vickers microhardness as a function of the equivalent strain of Ni with 2wt% CNTs HPT-deformed for 30 revolutions at RT, 200°C, 300°C, 400°C and for 40 revolutions at 400 + 200°C.

A summation of all Vickers microhardness values at a sample radius of 3 mm is given in Table 4.1. The microhardness values all decrease with increasing HPT-deformation temperature from between 724 and 767 HV0.3 at RT to between 395 and 465 HV0.3 at 400°C. The two-temperature process resulted in the largest microhardness difference between the CNT contents with 519 HV0.3 for the 0.25 wt% sample and 854 HV0.3 for the 3 wt% sample.

Except for the samples with 0.25 and 0.5 wt% CNTs, the samples HPT-deformed at 400 + 200°C showed a higher microhardness compared to the samples HPT-deformed at only 200°C. As the EBSD-scans of the Ni/CNT MMCs with 2 wt% CNTs showed, the grain sizes of the samples HPT-deformed at 200°C and 400 + 200°C are identical (c.f. Figures 3.7 and 3.8). The microhardness increase

4.2. Microhardness and tensile strength

can therefore be attributed to a more homogeneous distribution and smaller size of the CNT agglomerates (c.f. Figures 3.5 and 3.6). Higher microhardness values in sintered Ni/CNT MMCs due to a better homogeneity of the reinforcement phase were also found by Rossi et al. [82].

Table 4.1.: Vickers Microhardness (HV0.3) values for all Ni/CNT compositions and HPT-deformation temperatures (r=3 mm).

wt% CNTs	0.1	0.25	0.5	1	2	3
RT	729 ± 33	724 ± 33	767 ± 22	753 ± 11	724 ± 24	-
200°C	604 ± 19	587 ± 37	762 ± 12	712 ± 49	690 ± 39	776 ± 27
300°C	501 ± 5	478 ± 6	520 ± 5	510 ± 6	497 ± 4	600 ± 1
400°C	401 ± 3	395 ± 3	438 ± 5	451 ± 3	458 ± 8	465 ± 3
400 + 200°C	638 ± 13	519 ± 26	575 ± 32	769 ± 9	790 ± 29	854 ± 12

The thermal stability of the microhardness of Ni/CNT composites with 2wt% CNT content HPT-deformed at 200°C and at 400 + 200°C was investigated by annealing at 500°C for 3 h in a vacuum furnace. The results of the microhardness measurements of the as-deformed and annealed states are shown in Figure 4.6. The as-deformed samples show an increase in the microhardness over the radius with microhardness values at r = 3 mm of 690 ± 39 and 790 ± 29 HV0.3 for the 200°C and the 400 + 200°C sample, respectively. The microhardness values of the annealed samples at r = 3mm are 369 ± 26 and 413 ± 6 HV0.3 for the 200°C and the 400 + 200°C sample, respectively. The annealing experiments result therefore in a microhardness reduction of about 320 HV0.3 for the sample HPT-deformed at 200°C and 380 HV0.3 for the sample HPT-deformed at 400 + 200°C.

The measured microhardness difference between the as deformed samples, despite having similar grain sizes, can be explained by the improved CNT distribution and the smaller size of the CNT agglomerates, as shown in Figures 3.5, 3.6, 3.7 and 3.10. After annealing, the 400 + 200°C sample still has a slightly higher microhardness than the 200°C sample, and also the grain size and agglomerate size

4. Mechanical properties of nickel/carbon nanotube composites

are smaller and the CNT distribution is more homogeneous (Figure 3.10 d). This shows that a higher thermal stability could be achieved with the two-temperature process through optimizing the CNT distribution in the Ni matrix. Compared to pure metals, CNT-reinforced MMCs generally show a higher thermal stability, as described by Jenei et al. with Cu [31] and Suarez et al. with Ni [23]. In comparison to the improvement of the thermal stability of Ni through addition of 1 and 3 wt% CNTs, HPT-deformed at RT to 4 revolutions by Suarez et al. [23], the two-temperature process could improve the thermal stability of Ni/CNT MMCs with 2 wt% CNTs even further. This is evident by the higher microhardness of the 2 wt% sample deformed with the two-temperature deformation process and annealed at 500°C for 3 hours in this study, compared to the 1 and 3 wt% samples deformed at room temperature and annealed at 300°C for 3 hours in Ref. [23].

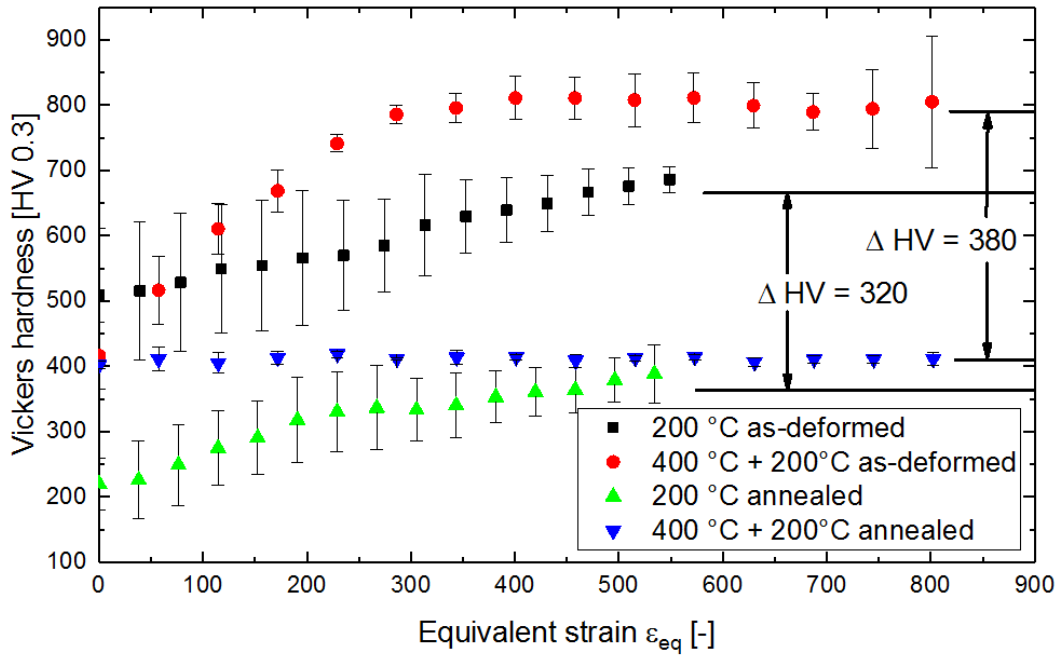


Figure 4.6.: Vickers microhardness as a function of the HPT-sample radius for as-deformed and for annealed Ni samples with 2wt% CNTs HPT-deformed at 200°C and 400 + 200°C. Annealing was performed for 3h at 500°C in a vacuum furnace.

4.2. Microhardness and tensile strength

The influence of the HPT-deformation temperature on the mechanical properties of the Ni/CNT MMCs was not only evaluated by microhardness measurements, but also by uniaxial tensile tests. The engineering tensile stress as a function of the engineering tensile strain is exemplarily shown in Figure 4.7 for the specimens with 0.25 and 2 wt% CNT content, HPT-deformed at 200°C, 300°C, 400°C and 400 + 200°C.

The 0.25 wt% specimen, HPT-deformed at 200°C, fractured already in the elastic regime at a tensile stress of 2121 MPa. After HPT-deformation at 300°C and 400°C, the 0.25 wt% specimens showed strong elongation with decreased ultimate tensile strength (UTS) values of 1338 and 892 MPa, respectively. The fracture stresses for these two samples were 1010 and 571 MPa, respectively. After the two-temperature deformation process (400 + 200°C), the UTS increases again to 1782 MPa and the fracture stress to 1531 MPa.

The 2 wt% specimens fractured both in the elastic regime after HPT-deformation at 200°C and 400 + 200°C at 2066 and 1671 MPa, respectively. At higher HPT-deformation temperatures, the 2 wt% specimens were stronger than the 0.25 wt% specimens with a UTS and an equally high fracture stress of 1558 MPa at 300°C and a UTS and fracture stress of 1221 and 1155 MPa, respectively, at 400°C.

The measured values for the yield strength, the UTS, the fracture stress and the Young's modulus for all CNT contents and HPT-deformation temperatures are shown in Figure 4.8. The yield strength (Figure 4.8 a) shows clear dependence on the CNT content only after the two-temperature deformation process, but here and in 200°C specimens with CNT content > 1 wt%, no plastic yield occurred due to early fracture in the elastic regime. At HPT-deformation at 300°C and 400°C the yield strength was generally lower with no clear dependence on the CNT content.

In Figure 4.8 b and c, the UTS and the fracture stress are plotted for all CNT contents. Similar to the yield strength, a general trend to lower values at higher

4. Mechanical properties of nickel/carbon nanotube composites

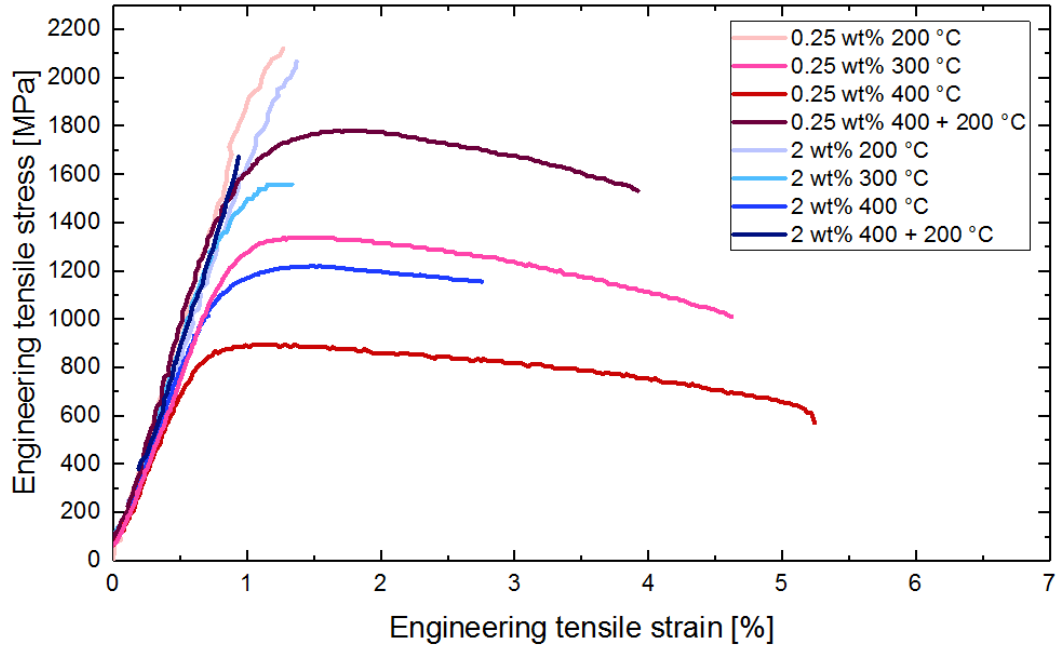


Figure 4.7.: Engineering tensile stress–strain curves of Ni MMCs with 0.25 and 2wt% CNTs (redrawn from publication B).

temperatures is given with no dependance on the CNT content. For specimens with no yielding (> 1 wt%, 200°C and 400 + 200°C) the fracture stress is plotted instead of the UTS (Figure 4.8 b).

The Young's modulus, as shown in Figure 4.8 d, also shows no change depending on the CNT content. As only the specimens HPT-deformed at 400°C have slightly lower values than the other specimens, a generally constant Young's modulus with a large scatter due to machine compliance has to be assumed.

A comparison between the measured values of the microhardness and the tensile strength can be made with the relation

$$H_V = 3 * \sigma_y, \quad (4.1)$$

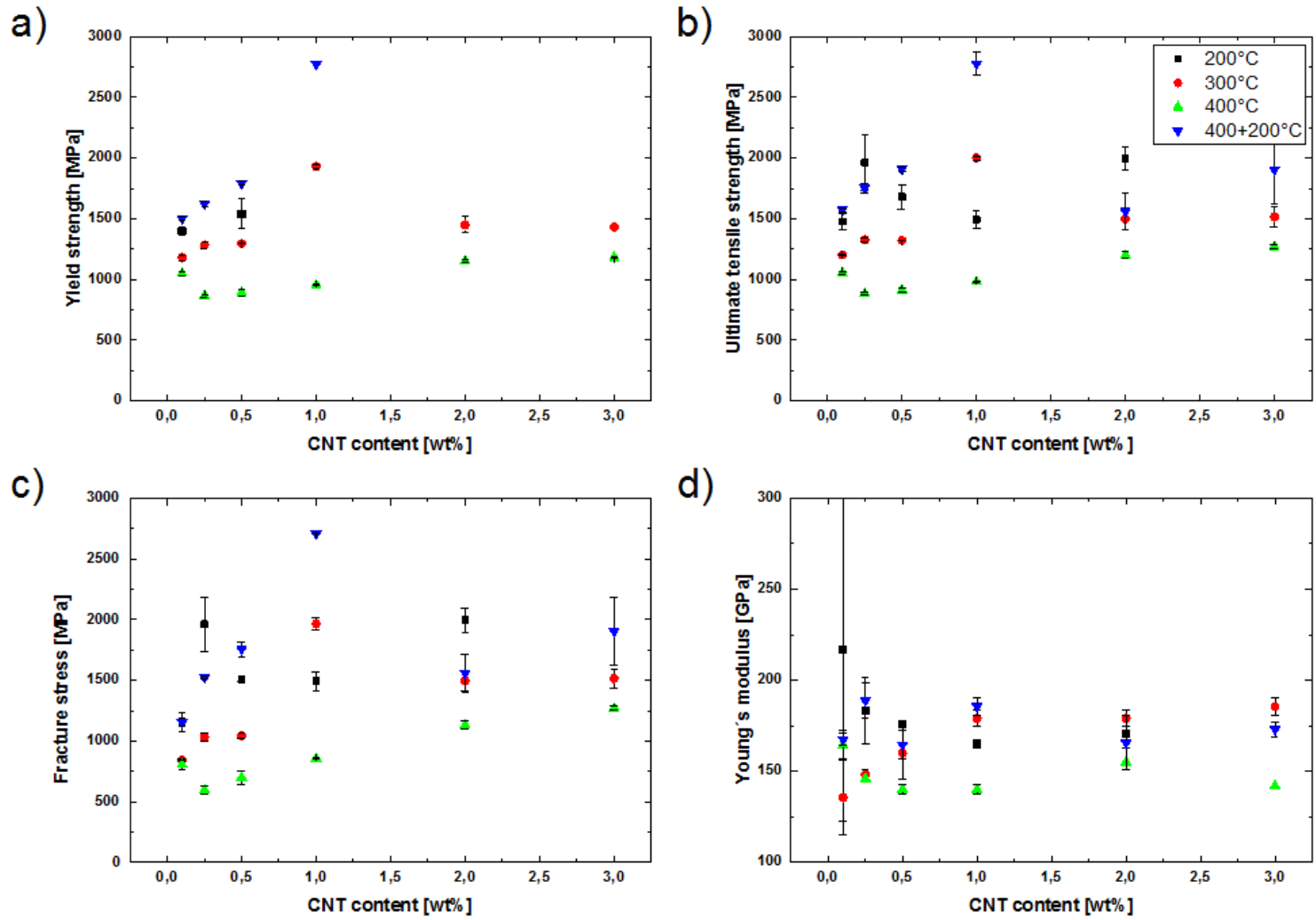


Figure 4.8.: Yield strength a), UTS b), fracture stress c), and Young's modulus d) as functions of the CNT content for Ni/CNT specimens HPT-deformed at different temperatures. (redrawn from publication B).

4. Mechanical properties of nickel/carbon nanotube composites

established by Tabor [83] with H_V the microhardness and σ_y the yield strength, both measured in MPa. Table 4.2 shows this relation between the microhardness shown in Table 4.1 and both yield strength and UTS shown in Figure 4.8 for all measured CNT contents and HPT-deformation temperatures. Almost all samples exhibit a microhardness to strength relation between three and five, with only a few below three. No apparent connection was found between the microhardness to strength ratio and the CNT content or the HPT-deformation temperature. This concentration of microhardness to strength ratios between three and five is rather unusual when compared to other materials. Zhang et al. [84] found for Cu and CuZn, deformed to various degrees by HPT and ECAP, as well as for different metallic glasses a microhardness to strength ratio around three. Only some metallic glass samples showed values between 3.8 and 6.3. For ceramics, on the other hand, they found much higher values between 28 and 183. This increase was found to be dependent on the ductility of the investigated materials. Ductile material, which were not fully hardened during the microhardness test showed a microhardness to strength ratio smaller than three. Materials, which followed the three-time relationship could be hardened-up to their UTS and for the brittle materials with ratios above three, the microhardness increases due to the limitations of the surrounding materials, which hinders shear deformation and enables cleavage cracking. To see, if the Ni/CNT MMCs follow this trend, shown in [84], the next section discusses their ductility and the occurring fracture mechanisms.

4.3. Ductility and fracture mechanisms

Concurrent with the UTS decrease due to increased HPT-deformation temperatures, the ductility increases. For the 0.25 and 2 wt% specimens, as shown in Figure 4.7, there is no plastic deformation after HPT-deformation at 200°C. At 300°C the ductility increases significantly for the 0.25 wt% specimen to a fracture strain of 4 %, and also the 2 wt% specimen shows some ductility with 0.5 % fracture strain. These values increase further after HPT-deformation at 400°C to 4.9 and 2.1 % for the 0.25 and 2 wt% specimens, respectively. A strong difference in the ductility of the two different CNT contents can be seen in the specimens HPT-deformed at 400 + 200°C. While both possess similar high tensile strengths,

4.3. Ductility and fracture mechanisms

Table 4.2.: Relations between microhardness and yield strength and UTS values for all Ni/CNT compositions and HPT-deformation temperatures.

HPT-deformation temperature [°C]	CNT content [wt%]	H_V/σ_y	H_V/UTS
200	0.1	4.2	4.0
	0.25	-	2.9
	0.5	4.9	4.5
	1	-	4.7
	2	-	3.4
	3	-	-
300	0.1	4.2	4.1
	0.25	3.9	3.8
	0.5	3.9	3.9
	1	2.6	2.5
	2	3.4	3.3
	3	4.1	3.9
400	0.1	3.8	3.7
	0.25	4.5	4.4
	0.5	4.8	4.7
	1	4.6	4.5
	2	3.9	3.7
	3	3.9	3.6
400+200	0.1	4.2	4.0
	0.25	3.1	2.9
	0.5	3.2	3.0
	1	2.7	2.7
	2	-	5.0
	3	-	4.4

the ductility is very different with a fracture strain of 3.1 % for the 0.25 wt% specimen and a failure in the elastic regime for the 2 wt% specimen.

In Figure 4.9 the uniform elongation, the strain at fracture and the reduction in area are plotted for all CNT content values and all HPT-deformation temperatures. The uniform elongation (Figure 4.9 a) shows no discernible correlation with the CNT content nor the HPT-deformation temperature. Only for the 2 and 3

4. Mechanical properties of nickel/carbon nanotube composites

wt% specimens the values are clearly higher at 400°C than at 300°C. The strain at fracture and the reduction in area (Figures 4.9 b and c) on the other hand display a clear trend both by decreasing with increasing CNT content and increasing with increasing HPT-deformation temperature. The specimens HPT-deformed at 400 + 200°C showed similar values as those HPT-deformed at 200°C.

The decrease of the ductility of Ni/CNT MMCs with increasing CNT content and with decreasing HPT-deformation temperature found in this work shows some similarities but also some differences with the results of similar investigations. Archakov et al. [39] investigated Ni mixed with 0.5–2 wt% thermally expanded graphite (TEG), which was ball-milled to create a Ni-graphene-graphite composite. Contrary to pure Ni, the composites showed no ductility and fractured in the elastic regime both after HPT-deformation at RT and at 200°C. The pure Ni sample showed always some ductility with a higher ductility after HPT-deformation at 200°C than at RT. Two studies, investigating the influence on the ductility of Al/CNT MMCs, also found a decreased fracture strain compared to pure Al [34, 35]. Rathmayr and Pippan [45] looked at Ni with carbon impurities between 0.06 and 0.008 wt%, HPT-deformed at various temperatures. For both 99.99 % pure Ni (8 ppm C) and 99.79 % Ni (600 ppm C), tensile test specimens showed remarkable stable ductility for HPT-temperatures ranging from –196°C to 400°C, with Ni99.79 having slightly lower fracture strain than Ni99.99.

The relation between ductility and microhardness to strength ratio, found by Zhang et al. [84] in various materials, where ductile materials showed a ratio at or below three and brittle materials above three, is not valid for the Ni/CNT MMCs investigated in this work. Comparing the microhardness to strength ratio, listed in Table 4.2, and the strain at fracture, shown in Figure 4.9 b, the microhardness to strength ratio is independent of their strain at fracture. Almost all samples have ratio values above tree, although some of them display good ductility with strain at fracture values up to 6 %, and those which have ratio values below three show brittle fracture. To explain this behaviour, a look at the fracture surfaces of the Ni/CNT MMCs and at the fracture mechanisms can be useful.

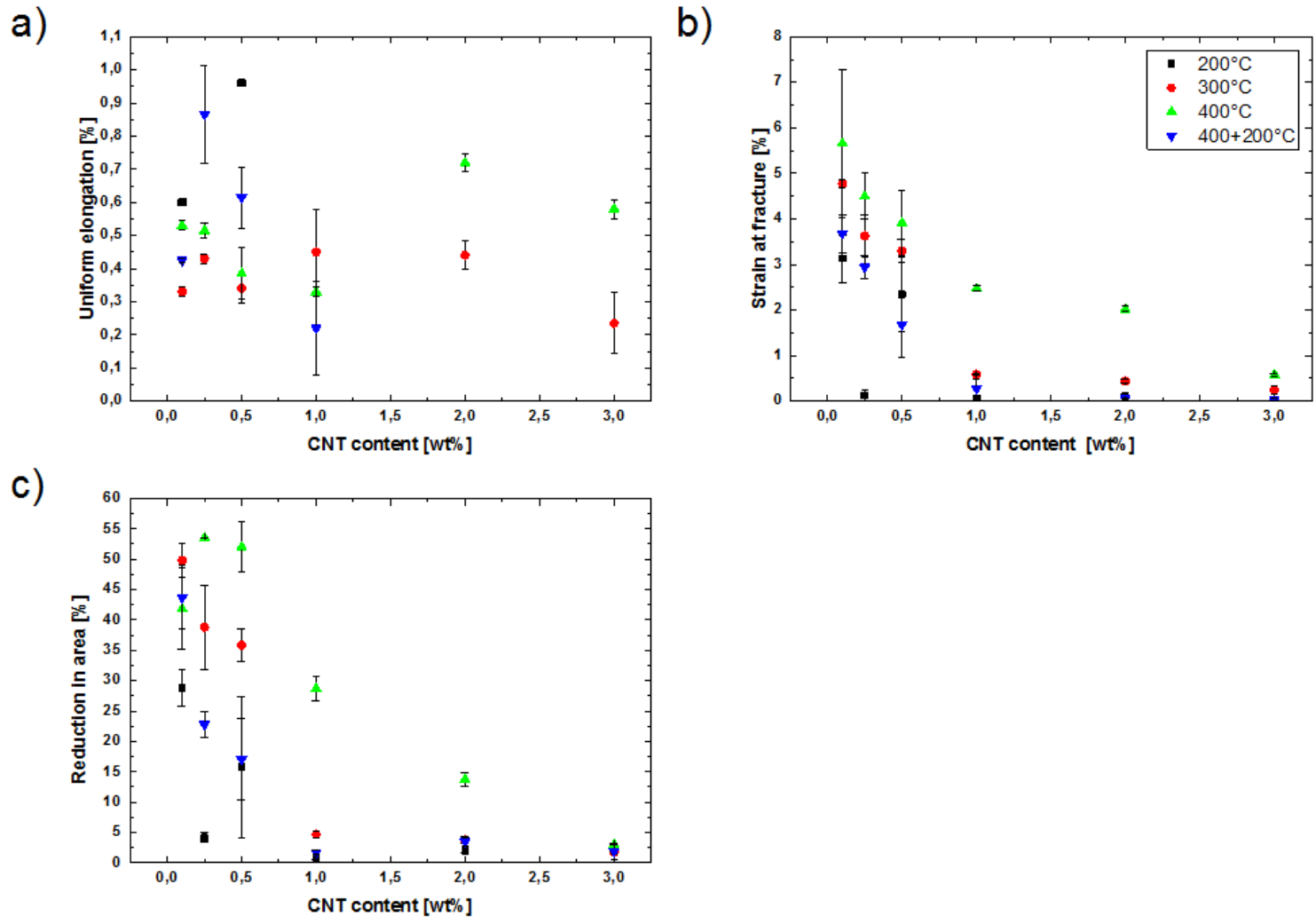


Figure 4.9.: Uniform elongation a), strain at fracture b) and reduction in area c) as functions of the CNT content for Ni/CNT specimens HPT-deformed at different temperatures. (redrawn from publication B).

4. Mechanical properties of nickel/carbon nanotube composites

For this, the fracture surfaces were investigated with an In-Lens detector in the SEM. The fracture surfaces of the 0.25 and 2 wt% specimens are shown exemplarily in Figure 4.10 for all HPT-deformation temperatures. The 0.25 wt% specimens (Figures 4.10 a-d) show generally a more ductile fracture surface than the 2 wt% specimens (Figures 4.10 e-h), which is in concordance with the reduction in area shown in Figure 4.9 c. With increasing HPT-deformation temperature, the ductility increases, and both 0.25 and 2 wt% specimens go from a generally brittle fracture surface at 200°C (Figures 4.10 a and e) to a more ductile one at 400°C (Figures 4.10 c and g). The two-temperature deformation process again highlights the difference between the low and the high CNT-content specimens with a ductile fracture of the 0.25 wt% specimen and a brittle fracture of the 2 wt% specimen (Figures 4.10 d and h).

In contrast to the apparent brittle-to-ductile transition seen in the low magnification images of the fracture surfaces, higher magnification images show microductile dimples in all investigated specimens. With increasing HPT-deformation temperature and lower CNT content the size of the dimples increases in accordance with the Ni matrix grain size.

Besides the structure of Ni matrix, the high magnification fractographs also show the presence of CNT agglomerates located at the center of some of the larger dimples (arrows in Figure 4.10). The 2 wt% specimen, HPT-deformed at 200°C (Figure 4.10 e) shows a large, irregular shaped inclusion, while the 2 wt% specimens deformed at 300°C and 400°C feature smaller and more disc-shaped inclusions (Figures 4.10 f and g). Still smaller are the inclusions present in the 0.25 wt% specimens, HPT-deformed at 400°C and 400 + 200°C (Figures 4.10 c and d).

The influence of the CNT content on the ductility, as presented in Figures 4.9 and 4.10, is more significant than on the yield strength and the UTS. The two-temperature deformation process in particular highlights the difference in the ductility of high and low CNT contents, with CNT contents ≥ 1 wt% resulting in a more brittle behaviour than CNT contents < 1 wt%.

4.3. Ductility and fracture mechanisms

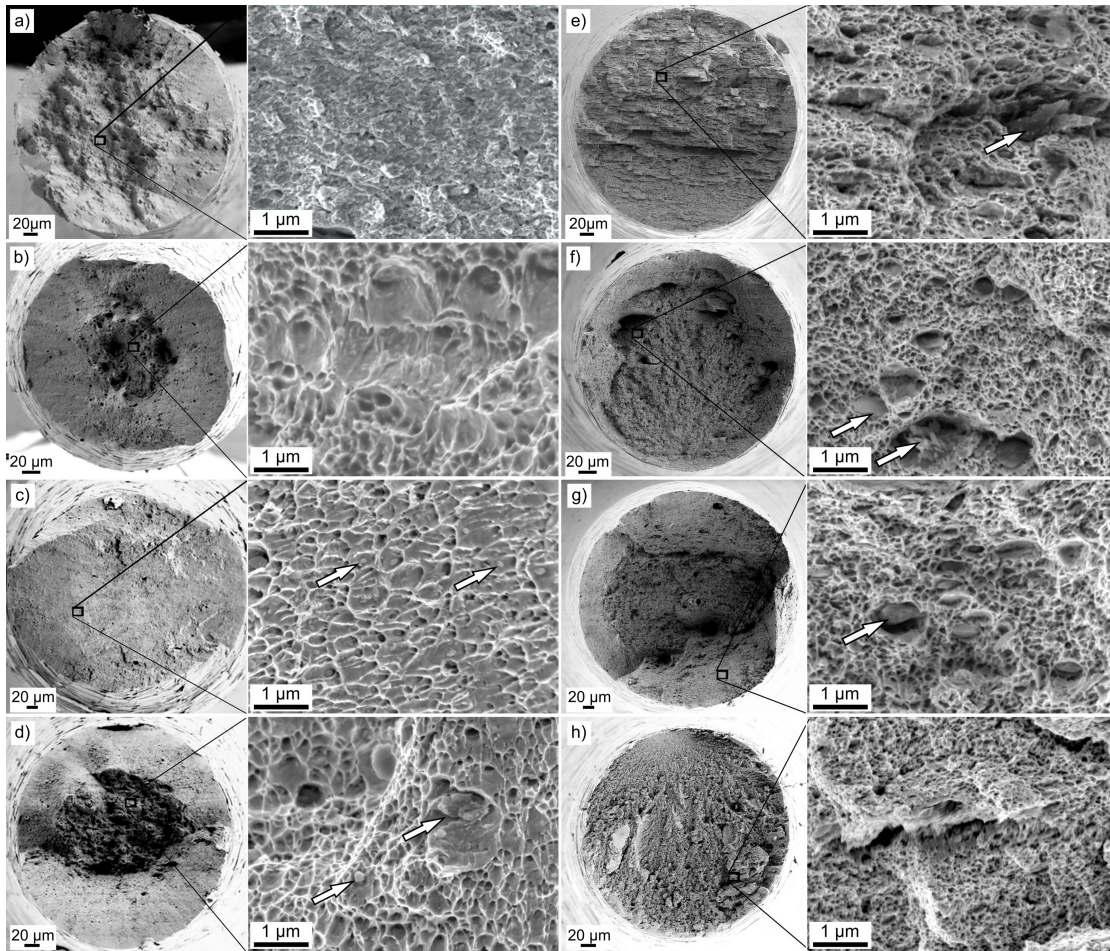


Figure 4.10.: Fracture surfaces and detail fracture surfaces of Ni MMCs with 0.25 and 2wt% CNTs HPT-deformed at a, e) 200°C, b, f) 300°C, c, g) 400°C, and d, h) 400 + 200°C. CNT agglomerates are marked by arrows. (redrawn from publication B).

As the Ni/CNT tensile specimens show a microductile fracture of the Ni matrix independent of the HPT-deformation temperature (Figure 4.10), similar to pure Ni [85], the overall ductility is most probably determined by the presence of the CNT agglomerates, acting as micro defects inside the Ni matrix. High amounts of CNTs in the Ni matrix result in large agglomerates which can not all be reduced in their size during HPT-deformation. These large agglomerates are also more irregular in their shape especially after HPT-deformation at lower temperatures

4. Mechanical properties of nickel/carbon nanotube composites

(c.f. Figures 3.6 a and b and 4.10 e). They consist of bundles of interlocked CNTs, which are prone to act as fracture nuclei due to strong compression and damaging by the HPT-deformation process [25, 62].

With increasing tensile stress the micro defects inside the agglomerates grow until a complete fracture. At stress levels near the UTS, the fragmented agglomerates create pores in the Ni matrix. At higher HPT-deformation temperatures, where the CNT agglomerates are smaller and more disc-shaped (Figure 4.10 b, c, f and g), the agglomerates show no fracture, but a decohesion from the Ni matrix [86]. In both cases, these pores grow, while additional pores emerge in the Ni matrix due to a multi-axial stress distribution. These pores subsequently grow, coalesce together and finally the whole specimen fractures. The size of the pores depend on the grain size and on the size of the agglomerates. In both high and low CNT specimens the size of the pores increases with the HPT-deformation temperature concurrent with the grain size (c.f. Table 3.1). As the CNT agglomerates in the 2 wt% specimen HPT-deformed at 400°C (Figure 4.10 g) are relatively large, the pores which contain agglomerates are also larger than the empty pores, while in the 0.25 wt% specimen (Figure 4.10 c) the pores with and without inclusions are about the same size. The occurrence of brittle fracture of the reinforcement phase in an otherwise ductile fracture with microdimples of the metal matrix has been observed in Al/SiC MMCs [87] while the decohesion of small inclusions without fracture leading to different sized pores depending on the presence of those inclusions was observed in Ni with only 8 ppm carbon content [45].

4.4. Compression strength and mechanical anisotropy

The test results for the compression tests were plotted for all CNT contents with the compression stress as a function of the compression strain. In Figure 4.11, specimens with 0.25 and 2wt% CNTs, HPT-deformed at a) 200°C, b) 300°C, c) 400°C, and d) 400 + 200°C are exemplarily shown.

4.4. Compression strength and mechanical anisotropy

For the 0.25 wt% specimens (red curves) the yield stress decreases from around 3000 MPa after HPT-deformation at 200°C (Figure 4.11 a) down to around 1500 MPa after HPT-deformation at 400°C (Figure 4.11 c). It again increases up to 2500 MPa after the two-temperature deformation process (Figure 4.11 d). The anisotropy similarly decreases with increasing HPT-deformation temperature as can be seen by the convergence of the yield stresses of the three testing directions.

As the yield strength decreases with the HPT-deformation temperature, the ductility of the 0.25 wt% specimens increases. While at 200°C only the axial direction showed some reasonable ductility (Figure 4.11 a), after HPT-deformation at 300°C and 400°C, compression strain of up to 25 % could be reached (Figures 4.11 b and c). With the two-temperature process, the ductility slightly decreases with values between 5 and 15 % (Figure 4.11 d).

Ni/CNT MMC specimens with 2 wt% (blue curves) show a similar behaviour, but with a lower yield strength of around 2500 MPa at 200°C (Figure 4.11 a), a slightly higher yield strength of up to 2000 MPa at 400°C (Figure 4.11 c) and brittle fractures at 400 + 200°C (Figure 4.11 d).

The fracture mode of the Ni/CNT MMCs during compression mostly depends on the amount of CNTs. Specimens with low CNT content deform by shear band formation and strain localization at an angle of about 45° at 200°C and by ductile deformation (barrel shape) at higher HPT-deformation temperatures. Specimens with CNT content ≥ 1 wt% generally fail through brittle fracture. Some deform by shear band formation at higher HPT-deformation temperatures.

To determine the influence of the size, shape and distribution of the CNT agglomerates on the mechanical anisotropy of the Ni/CNT MMCs, their microstructure was evaluated by SEM in axial, radial and tangential direction. Figure 4.12 shows the images taken at a radius of 3 mm from the center of the HPT-discs for the Ni/CNT MMCs with 2 wt% CNT content, HPT-deformed at 200°C, 300°C, 400°C, and 400 + 200°C. Binarized versions of the SEM images were produced with the program ImageJ [69] to evaluate the diameter, aspect ratio and nearest neighbour

4. Mechanical properties of nickel/carbon nanotube composites

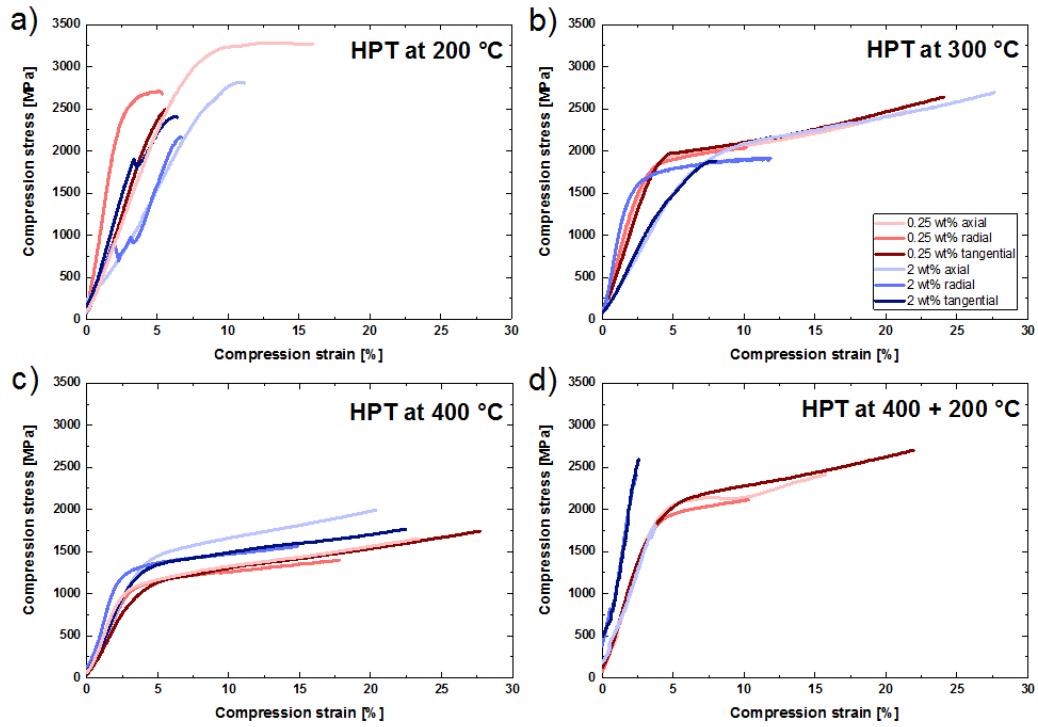


Figure 4.11.: Compression stress-strain curves in axial, radial and tangential direction of Ni MMCs with 0.25 and 2wt% CNTs, HPT-deformed at a) 200°C, b) 300°C, c) 400°C, and d) 400 + 200°C (redrawn from publication B).

distance (NND) of the agglomerates and superimposed on the original images to make them more visible.

After HPT-deformation at 200°C (Figures 4.12 a-c), the size of the agglomerates shows a large variation with some agglomerates having a diameter larger than 300 nm. The shape of the agglomerates can be described as oblate ellipsoid or almost flat disc, which are primarily stretched in the shear direction (Figure 4.12 b). The distribution at 200°C HPT-deformation temperature is rather inhomogeneous with clusters or concentration of larger agglomerates inter-dispersed by smaller ones. Especially in axial direction (Figure 4.12 c) there are areas with no discernible CNT agglomerates.

4.4. Compression strength and mechanical anisotropy

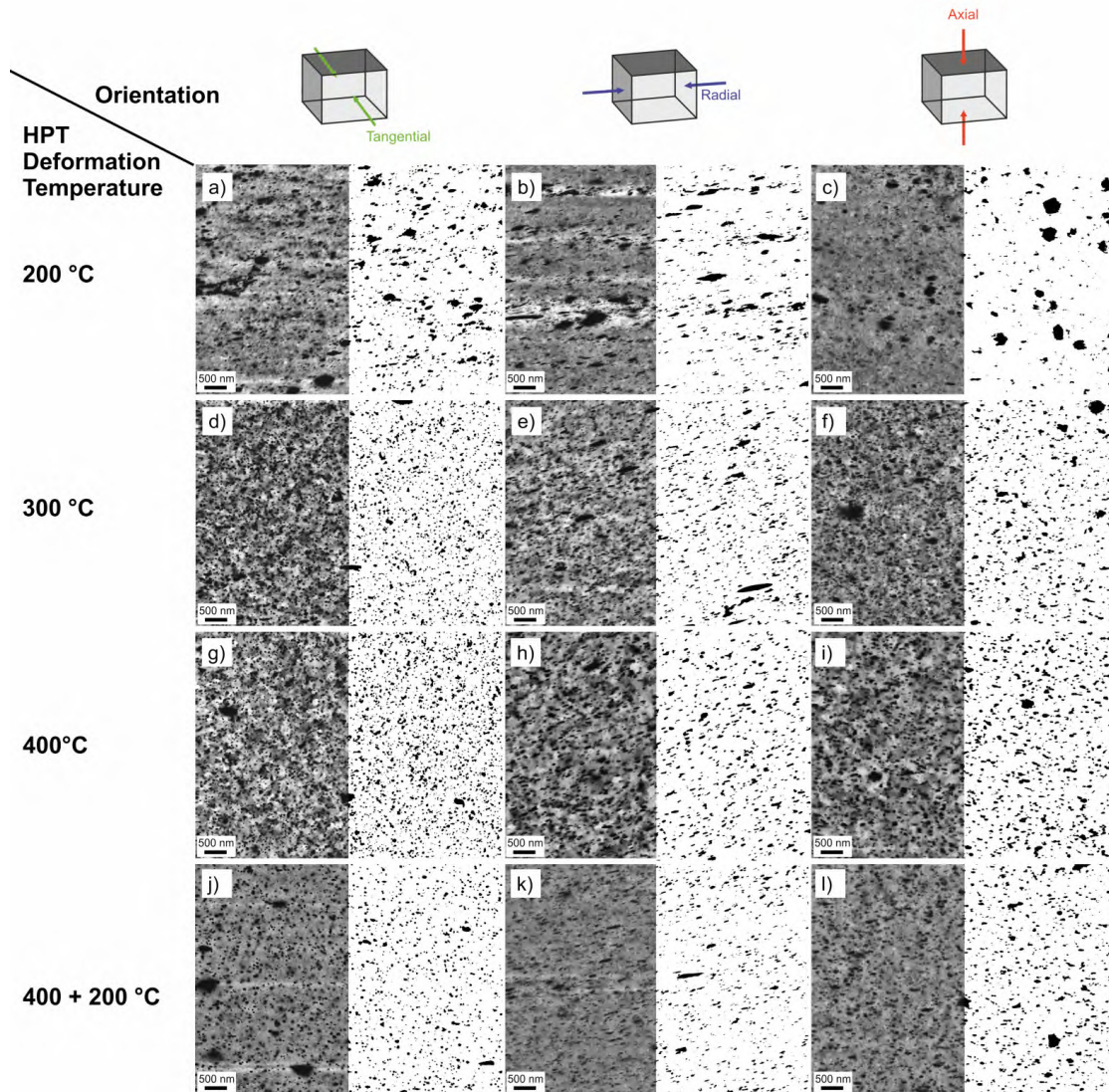


Figure 4.12.: SEM images at 3 mm radius in tangential, radial, and axial direction of Ni MMCs with 2 wt% CNTs, HPT-deformed at 200°C a-c), 300°C d-f), 400°C g-i), and 400+200°C j-l) (redrawn from publication B).

Increasing the HPT-deformation temperature to 300°C (Figures 4.12 d-f) results in fewer larger agglomerates and more smaller ones with diameters smaller than 50 nm. The aspect ratio of the agglomerates decreases only slightly with the ag-

4. Mechanical properties of nickel/carbon nanotube composites

glomerates still elongated mainly in shear direction. The agglomerate distribution becomes more homogeneous with a smaller variance of the NND.

Figures 4.12 g-i show the microstructure after a further increase of the HPT-deformation temperature to 400°C. The agglomerate sizes are very similar to those of the 300°C specimens with slightly less very small and very large ones. The aspect ratio also only decreases very marginally with the agglomerates again elongated in shear direction. The NND of the agglomerates increases to an extent due to there being less very small agglomerates, but overall the distribution of the agglomerates is very homogeneous.

In terms of agglomeration properties, the two-temperature deformation process shows no significant change from the 300°C and 400°C specimens. As depicted in Figure 4.12 j-l, the microstructure images show a homogeneous distribution of small agglomerates, elongated in shear direction. Only a few agglomerates larger than 200 nm in diameter are present.

The grains of the Ni matrix show, contrary to the CNT agglomerates, no discernible elongation in shear direction. The grain sizes depend in all three directions on the HPT-deformation temperature as shown in Figures 3.7 and 3.8 and Table 3.1.

To evaluate the relation between the mechanical properties of the Ni/CNT MMCs during the compression tests and their microstructure, depending on the HPT-deformation temperature and the testing orientation, a comparison between Figures 4.11 and 4.12 has to be done.

The 2wt% specimens show a decrease of both the magnitude and the anisotropy of the yield strength with increasing HPT-deformation temperature as well as an increase in the ductility. With the two-temperature deformation process, the yield strength and its anisotropy again increase and the ductility decreases to similar values observed at 200°C (blue curves in Figure 4.11). Concurrent with these property changes, the sizes and distribution of the CNT agglomerates become

4.4. Compression strength and mechanical anisotropy

more homogeneous, while their aspect ratio decreases slightly. Also the Ni grain sizes increase. In the specimens deformed at 400 + 200°C the Ni grain sizes decrease again to 200°C values, while the agglomerate properties are the same as in the 400°C specimens.

The change in the compression strength and ductility can be attributed to the increase in the grain size. This corresponds to the decrease of the microhardness and tensile strength, shown in Section 4.2, the increase of the ductility, shown in Section 4.3, as well as the increase of the grain size, shown in Section 3.2.3. The return of the strength and ductility in the 400 + 200°C specimens to values similar to the 200°C specimens has also been shown by those previous results.

The change in the anisotropy with the HPT-deformation temperature can be explained by the change in the number of larger, elongated CNT agglomerates. Both decrease from 200°C to 400°C and again slightly increase in the 400 + 200°C specimens. Due to the higher CNT content, more of these large agglomerates remain at higher HPT-deformation temperatures in the 2 wt% specimens than in the 0.25 wt% specimens, which is in concordance with their higher anisotropy at those temperatures (Figure 4.11 b-d). Higher values of anisotropy due to a higher volume fraction of reinforcing particles were also found in Al/SiC MMCs by Ganesh and Chawla [87]. They observed a higher tensile strength in the direction of extrusion, which was also the preferred orientation of the elongated SiC particles. The compression tests of the 2 wt% NiCNT MMCs on the other hand showed a higher compression strength in axial direction, normal to the shear direction and elongation. This difference is probably a result of the different testing modes (tensile vs. compression).

The anisotropy of the Ni/CNT MMCs could also be partially influenced by an elongation of the Ni grains in shear direction. As the grains are too small to be adequately resolved in the SEM images (Figure 4.11), TEM images have to be used to determine a possible elongation of the Ni grains. Figure 3.6 shows the microstructure of the MMCs in axial direction. An elongation of the CNT agglomerates in one preferred direction can be clearly seen for the 300°C and 400°C

4. Mechanical properties of nickel/carbon nanotube composites

samples (Figures 3.6 b and c, respectively). The Ni grains, on the other hand, show no elongation in this direction. The grain shape is therefore unlikely to influence the mechanical anisotropy of the Ni/CNT MMCs. This is also in concordance with results obtained from tensile and compression tests of pure HPT-deformed Ni by Rathmayr et al. [88]. They found that the grain aspect ratio has no influence on the strength or the uniform elongation in either loading condition. What they found, was a difference of about 100 MPa in the UTS, which they concluded was caused by the shear texture.

The shear texture of the Ni/CNT MMCs with 2 wt% CNT content is shown in Figure 3.9 for the same HPT-deformation temperatures as for the compression tests. While the anisotropy of the compression strength changes with the HPT-deformation temperature, the shear texture shows no significant changes. Another factor speaking against an influence of the shear texture on the anisotropy of the Ni/CNT MMCs is that in this case a higher compression strength would be measured in tangential testing direction (parallel to the shear direction) than in axial testing direction (perpendicular to the shear direction) [88]. This is not the case for the specimens HPT-deformed at 200°C, 300°C and 400°C (Figures 4.11 a-c). Only the two-temperature deformation process (Figure 4.11 d) displays a lower compression strength in axial direction, but due to the fracture in the elastic regime in this case, a premature failure of this specimen, and therefore a possibly higher strength, can not be excluded.

5. Nanodiamond reinforced metal matrix composites

The second part of this thesis focuses on the production of MMCs reinforced with NDs. NDs are less vulnerable to high deformation forces than CNTs due to their size and shape, therefore ball-milling can be used to blend the ND powder and the metal powders together before compaction and deformation by HPT. The main focus of this work was on creating Ag/ND MMCs, but Au/ND MMCs were also produced. Additionally, Ni/ND processed by colloidal mixing and sintering were HPT-deformed and investigated. The Ag/ND MMCs could be used for example as heat sinks due to the high thermal conductivity reported in ND-reinforced metals [89], or for applications where a superior wear resistance is needed [90]. Ag/ND and Au/ND MMCs could also both be used for jewellery applications.

5.1. Pre-deformation treatment: Ball-milling

Mechanical alloying through high-energy ball-milling is a well-known method to blend two or more powdered materials into a homogenous mixture. For this process, the powders are loaded in the right proportion into the mill together with the grinding medium. Hardened steel balls are the most used grinding medium, but other materials like tungsten carbide or various ceramics can also be used, depending on the hardness of the milled materials [2].

Mostly used for alloying different metals together [91–94], it can also be used to refine the grains of pure metals [95–97] and to disperse second phase particles

5. Nanodiamond reinforced metal matrix composites

such as NDs in a metal matrix powder [98–103]. The severe plastic deformation happening during ball-milling due to the highly kinetic impact of the steel balls on the powders results in different structural changes. The powder particles are constantly broken apart and re-welded together, which decreases the grain size and increases the dislocation density. This leads to a microhardness increase through Hall-Petch and work hardening. Different metals are welded together and build a homogeneous alloy during the ball-milling process. The solubility of otherwise non-mixable materials can be extended by the ball-milling process to create metastable supersaturated solid solutions. Brittle, insoluble particles, like oxides or non-metallic reinforcement phases (ceramics, NDs) get uniformly dispersed in the more ductile metal powders [2].

Due to the high impact energies during milling, long fiber materials such as CNTs are not so well-suited for this method. The breaking and shortening of the fibers would be detrimental to their function [104]. NDs on the other hand are small (4-6 nm diameter), have a low aspect ratio and a high strength [60]. Therefore, they can be easily distributed during ball-milling without damaging their structure. In this work, a planetary ball-mill was used to mix Ag powder and ND powder to create a Ag/ND MMC powder, which was then further processed by HPT-consolidation and -deformation. Special emphasis was laid on finding the optimal milling parameters to ensure a homogenous distribution of the NDs.

5.2. Experimental

Pure Ag powder (-500 mesh, spherical, purity: 99.9 %) provided by Alfa Aesar and ND powder (particle size: 4-6 nm, carbon purity: > 98%) provided by Plas-machem were used as starting materials for the Ag/ND MMCs. For the Au/ND MMCs and the Ni/ND MMCs, the same ND powder was used as well as pure Au powder (5.5-9.0 micron, spherical, purity: 99.96+ %) and pure Ni powder (-325 mesh, dendritic), both provided by Alfa Aesar.

Ball-milling was conducted in a planetary ball-mill PM 400 (Retsch) in ambient atmosphere as well as in an inert Argon atmosphere. Figure 5.1 shows a schematic

5.3. Microhardness and mechanical behaviour

of the milling process. Up to 4 hardened steel jars are mounted on a rotating plate. The ratio of plate rotation speed ω_R to jar rotation speed ω_r is 1 : -2. The plate rotation speed ω_R and the milling time t can be pre-programmed. The ball-milling was conducted with alternating intervals of 15 minutes milling and 15 minutes breaks to prevent heating of the powder. The jars were filled with powder and hardened steel balls in a weight ratio of 1 : 10. Either pure Ag powder or mixtures of Ag and ND powder with ND contents of 0.1, 0.5, 1, 2 and 5 wt% (0.3, 1.6, 3.2, 6.3 and 14.8 vol%) were milled. After milling, the Ag/ND composite powders were compacted and deformed by HPT as depicted in Figure 5.1. The HPT-deformation was conducted at room temperature at a hydrostatic pressure of 5 GPa and a velocity of 0.6 rounds per minute. Table 5.1 summarizes the production parameters for all presented samples.

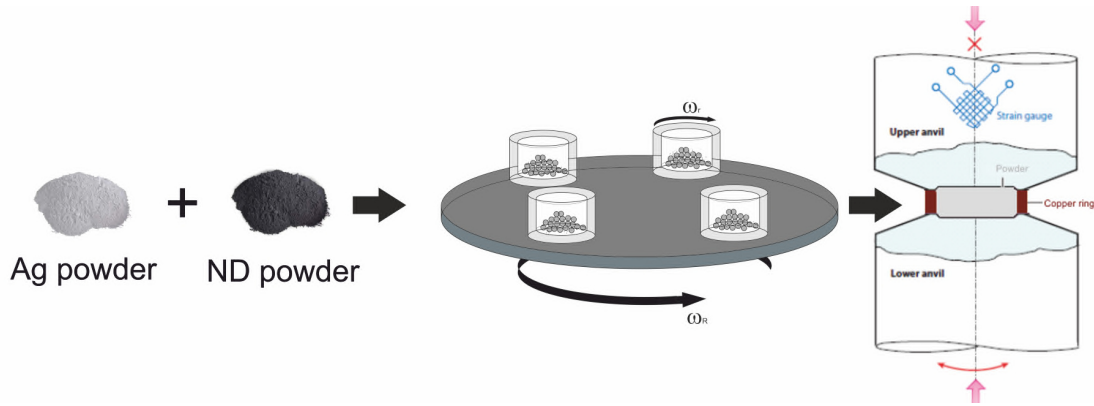


Figure 5.1.: Schematics of the ball-milling process and the powder compaction and HPT-deformation process (modified from ref. [4]).

5.3. Microhardness and mechanical behaviour

Ag/ND composites were produced by adding increasing amounts of NDs to the Ag powder and by ball-milling the mixed powders with increasing milling time t and a milling velocity $\omega_R = 150$ rpm (Table 5.1). The powders were then compacted

5. Nanodiamond reinforced metal matrix composites

Table 5.1.: ND content, milling parameters and number of HPT revolutions for all investigated Ag/ND composite samples.

Sample number	ND cont. [wt%]	ND cont. [vol%]	Milling time t [h]	Milling speed ω_R [rpm]	Milling atmosphere	HPT turns n
1	0	0	-	-	-	30
2	0.1	0.3	2	150	air	20
3	0.5	1.6	2	150	air	20
4	0.5	1.6	2	150	air	-
5	1	3.2	3	150	air	20
6	2	6.3	3	150	air	30
7	5	14.8	6	150	air	30
8	5	14.8	6	300	air	30
9	0	0	6	300	Ar	30
10	0.1	0.3	6	300	Ar	30
11	0.5	1.6	6	300	Ar	30
12	0.5	1.6	6	300	Ar	-
13	0.5	1.6	6	300	Ar	5
14	2	6.3	6	300	air	30
15	2	6.3	6	300	air	5

and deformed by HPT. Figure 5.2 shows the results for the microhardness measurements of the first processed Ag/ND composite samples compiled in Table 5.1 (samples 2-7) as well as the microhardness of a pure as-received Ag sample, which was only HPT-deformed for 30 revolutions and contains no ND reinforcement (sample 1). The microhardness at a radius of 3 mm increases from 105 HV0.1 for the pure HPT-deformed Ag reference sample to 160 HV0.1 for the Ag/ND composite sample with 5 wt% NDs ball-milled for 6 hours at 150 rpm and HPT-deformed for 30 revolutions. In addition to the HPT-deformed samples, the average microhardness of an Ag 0.5 wt% ND composite sample, ball-milled for 2h at 150 rpm and compacted at 5 GPa hydrostatic pressure without further HPT-deformation (sample 4), is given (77 ± 4 HV0.1) to show the effect of subsequent HPT-deformation on the microhardness evolution.

5.3. Microhardness and mechanical behaviour

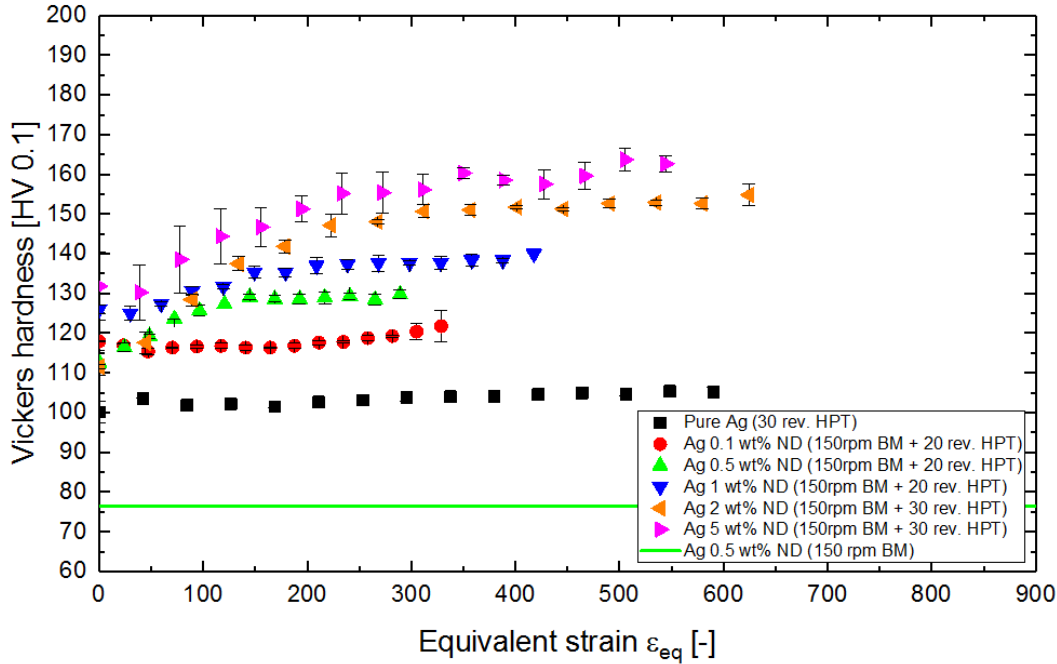


Figure 5.2.: Vickers microhardness [HV 0.1] as function of the equivalent strain ϵ_{eq} for pure as-received Ag and Ag/ND composites with varying amounts of NDs, ball-milled for varying milling times at 150 rpm.

Despite the increase in milling duration (3h or 6h instead of 2h for ND contents ≥ 1 wt%), the onset of microhardness saturation goes to higher values of equivalent strain with increasing ND content (Figure 5.2). To ensure saturation of microhardness over the whole sample even for high ND contents, the ball-milling velocity ω_R was increased from 150 rpm to 300 rpm, first for 5 wt% NDs (sample 8 in Table 5.1). These milling parameters (6 h at 300 rpm) result in an increased microhardness, which is constant over the whole radius (Figure 5.3). Composite powders with 0.1, 0.5 and 2 wt% NDs as well as pure Ag powder were then produced with the same milling parameters (samples 9-15 in Table 5.1). All 300 rpm composite samples showed increased microhardness compared to the 150 rpm composite samples, while the microhardness of the pure HPT-deformed Ag sample, ball-milled at 300 rpm (sample 9) did not change compared to the pure Ag reference sample (sample 1) after subsequent HPT-deformation. Overall, a mi-

5. Nanodiamond reinforced metal matrix composites

microhardness increase of more than 80 HV0.1 compared to the pure Ag reference sample could be achieved by adding NDs as reinforcement phase. Additionally, 30 HPT-revolutions were enough to reach full saturation, except for the 0.5 wt% sample, which showed a slight microhardness increase over the first 0.5 mm from the center (Figure 5.3). To evaluate the individual contributions of ball-milling and HPT, the average microhardness of a compacted sample with 0.5 wt% NDs (sample 12) and the microhardness of a sample HPT-deformed for 5 revolutions containing the same amount of NDs (sample 13) are shown in Figure 5.3. The compacted sample is about 45 HV0.1 (32 %) softer than the HPT-deformed sample. Furthermore, even a smaller amount of strain is enough to reach saturation, as the 5 revolutions sample shows similar microhardness values as the 30 revolutions sample at comparable strain ($\epsilon_{eq} \sim 100$). In terms of microhardness saturation, 5 revolutions are enough for samples containing higher amounts of NDs (2 wt%, sample 15), since nearly no microhardness increase with increasing equivalent strain up to a strain of about 100 is observed (Figure 5.3).

Concurrent with the Ag/ND composites, ND reinforced MMCs with Au as matrix material were produced and investigated. Several powder mixing methods and ND concentrations were compared. Au MMCs with 0.1 and 1 wt% NDs were prepared by colloidal mixing [62], while ball-milling for 6 hours at 300 rpm milling velocity was used to produce an MMC powder with 0.5 wt% NDs. These powders were compacted and HPT-deformed at RT for 30 or 50 revolutions. Additionally, pure Au powder was compacted and HPT-deformed for 10 revolutions as a reference sample. Figure 5.4 shows the measured Vickers microhardness as function of the equivalent strain for these Au/ND MMCs. HPT-deformed pure Au powder reaches microhardness values of 110 HV0.1 after 10 HPT-revolutions. Au powder reinforced with 0.1 wt% NDs, colloidal mixed, compacted and HPT-deformed for 30 revolutions shows an increased microhardness of 140 HV0.1, while the identically processed Au/ND MMC with 1 wt% reaches 160 HV0.1. The highest microhardness values were reached with a 0.5 wt% ND content, ball-milled for 6 hours at 300 rpm. Two samples were prepared by HPT-deformation, one with 30 revolutions and one with 50 revolutions. Both reached a microhardness of 190 HV0.1, with the 50 revolution sample having a more evenly saturated microhardness along the

5.3. Microhardness and mechanical behaviour

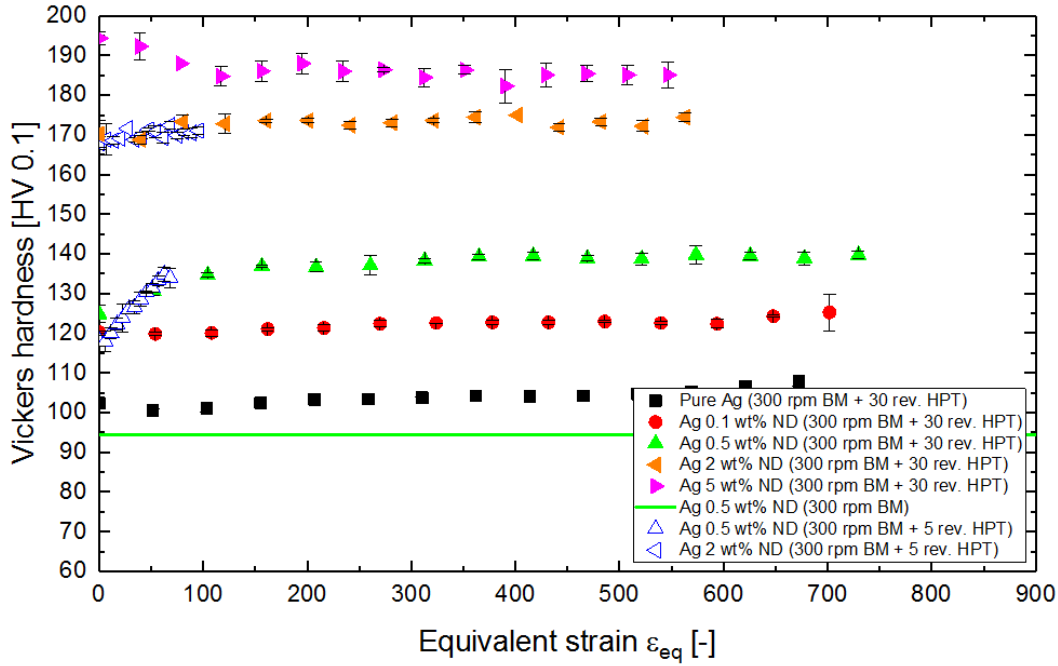


Figure 5.3.: Vickers microhardness [HV 0.1] as function of the equivalent strain ϵ_{eq} for pure as-received Ag and Ag/ND composites with varying amounts of NDs, ball-milled for 6h at 300 rpm.

sample radius.

Another material combination that was investigated is Ni reinforced with NDs. They were produced similar to the Ni/CNT composites by colloidal mixing and sintering with ND contents of 0.5, 1, 3 and 10 vol% [62]. All ND concentrations were first HPT-deformed for 30 revolutions at RT. As can be seen in Figure 5.5, the reached saturation microhardness values were 510, 600 and 660 HV0.3 for the 0.5, 1 and 3 vol% samples, respectively. A continuous microhardness measurement along the radius of the 10 vol% sample was not feasible due to the large amount of cracks present after HPT-deformation. To increase the microhardness, improve the ND distribution and avoid the formation of cracks, the Ni/ND MMCs were also HPT-deformed with the two-temperature deformation process developed for the Ni/CNT MMCs. The 0.5 and 10 vol% samples were HPT-deformed for 30 rev-

5. Nanodiamond reinforced metal matrix composites

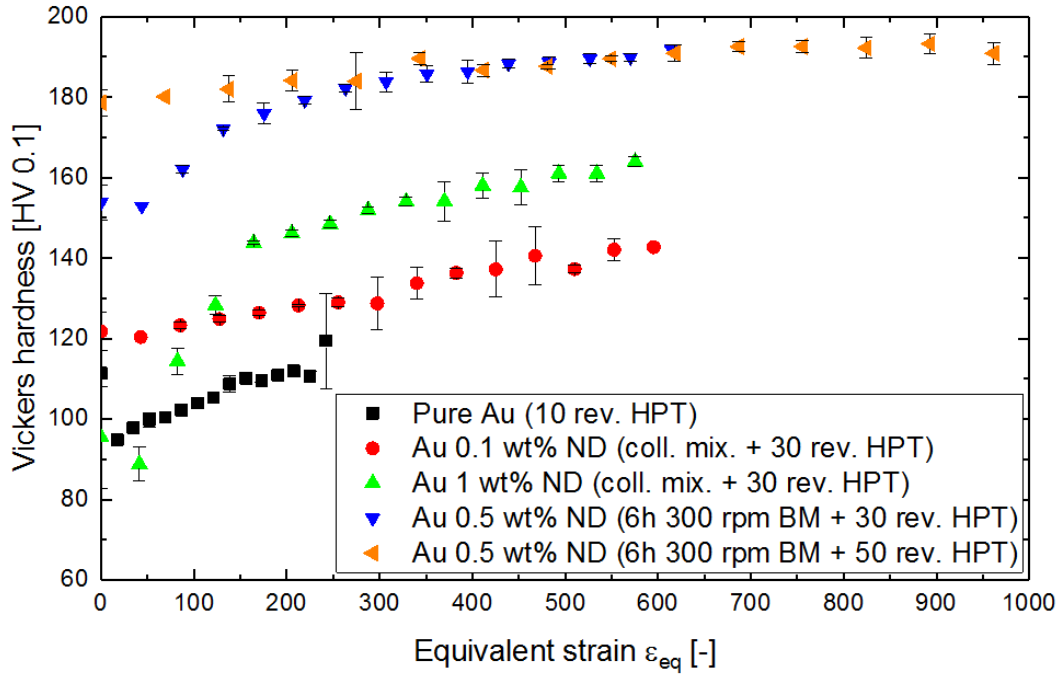


Figure 5.4.: Vickers microhardness [HV 0.1] as function of the equivalent strain ϵ_{eq} for pure as-received Au and Au/ND composites with varying amounts of NDs, blended together by either colloidal mixing or ball-milling for 6h at 300 rpm.

olutions at 400°C and then for 10 revolutions at 200°C, the 1 and 3 vol% samples for 30 revolutions at 400°C and then for 1 revolution at RT. The microhardness values increase to 570 and 660 HV0.3 for the 0.5 and 1 vol% samples, respectively, remains at 660 HV0.3 for the 3 vol% sample and reaches 800 HV0.3 for the 10 vol% sample (Figure 5.5).

A comparison with the microhardness of the Ni/CNT shows that the Ni/ND MMCs have a lower saturation microhardness than the Ni/CNT MMCs after HPT-deformation at RT (c.f. Figures 5.5 and 4.4). While the Ni/ND MMCs have microhardness values between 510 and 660 HV0.3 depending on the ND content, the Ni/CNT MMCs all have microhardness values above 720 HV0.3 with less variation between the different CNT contents. For the samples deformed with the

5.3. Microhardness and mechanical behaviour

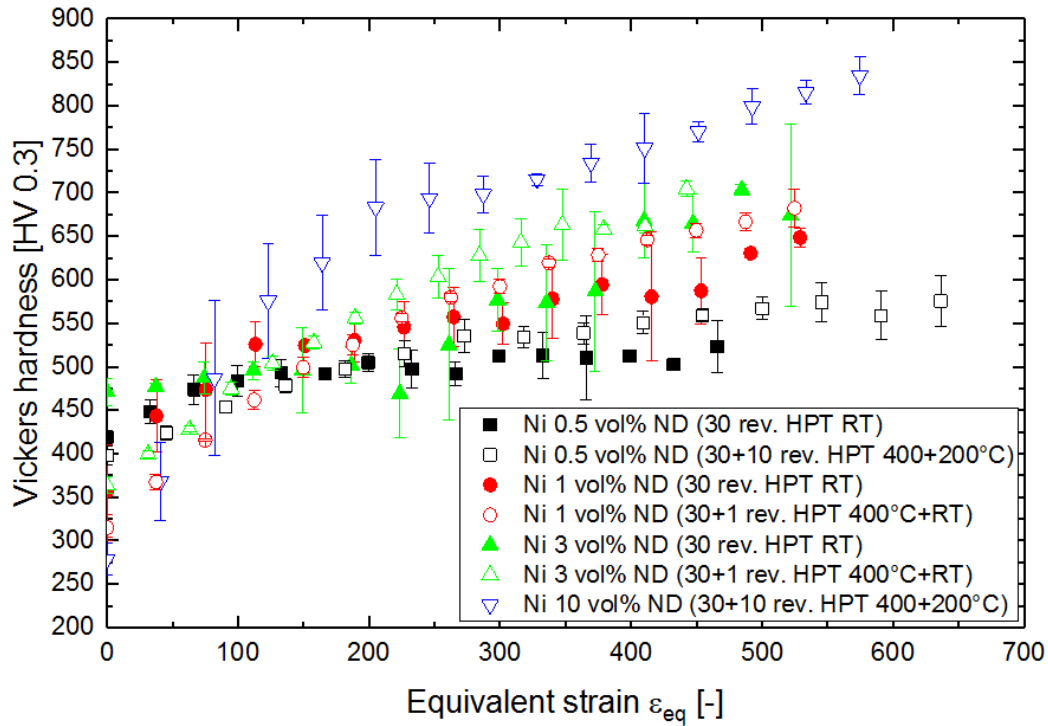


Figure 5.5.: Vickers microhardness [HV 0.3] as function of the equivalent strain ϵ_{eq} for Ni reinforced with varying amounts of NDs and HPT-deformed at RT and at elevated temperatures.

two-temperature process, the Ni/ND MMCs gain a saturation microhardness more similar to the Ni/CNT MMCs with values for the Ni/ND samples between 570 and 800 HV0.3 compared to those for the Ni/CNT samples between 520 and 850 HV0.3.

To evaluate the influence of the NDs on the mechanical properties of HPT-deformed Ag, tensile tests were performed with pure HPT-deformed Ag powder samples, HPT-deformed pure ball-milled Ag samples, and HPT-deformed ball-milled composite samples with 0.1, 0.5 and 2 wt% ND content. These samples were selected to investigate both the influence of the ball-milling process and of the increasing ND content on the mechanical properties of HPT-deformed Ag. Ag/ND composite

5. Nanodiamond reinforced metal matrix composites

samples with 5 wt% NDs were not tested due to their disposition to develop cracks during HPT-deformation. The processing parameters were chosen to be 6 hours at 300 rpm for ball-milling and 30 revolutions for the subsequent HPT-deformation to guarantee a homogeneous distribution of the NDs in the testing region. Characteristic engineering stress-strain curves are shown in Figure 5.6. In Table 5.2, the mean values and standard deviations for the ultimate tensile strength (UTS), the yield strength, the uniform elongation, the stress and strain at fracture and the area reduction for four samples of all investigated composites are summarized. UTS, yield strength and stress at fracture are slightly higher for HPT-deformed pure ball-milled Ag samples compared to pure HPT-deformed Ag powder samples and further increase with increasing ND content. The uniform elongation, strain at fracture and area reduction on the other hand decrease.

The tensile strength is proportional to the microhardness and known to increase both for ball-milled and HPT-deformed metals due to the decreased grain size [1, 91]. Concurrent with the strength increase a decrease of the ductility has to be accepted for these materials. Angella et al. [105] showed, that the UTS of as-cast pure Ag increases from 140 MPa for undeformed Ag to 320 MPa after an applied equivalent strain of about 8 by equal-channel angular pressing (ECAP). The fracture elongation on the other hand decreases from 26 % to 15 %. Gubicza et al. [106] also looked at the influence of ECAP on the mechanical properties of pure Ag. They reached an UTS of 330 MPa and an elongation of 25 % after 4 ECAP passes. These results are similar to those we found for pure HPT-deformed Ag powder samples, which are 329 ± 11 MPa and 13 ± 1 % for the UTS and the fracture elongation, respectively (Table 5.2). In contrast, the UTS of coarse-grained Ag is much lower. Hsueh et al. [107] investigated the tensile behavior of pure cold drawn Ag wires and recorded an UTS of 180 MPa and an elongation of 17 %. For pure, undeformed Ag ingots, Wu and Lee [108] observed an UTS of 107 MPa and a uniform strain of 25 %.

The same effect of increasing strength and decreasing ductility is prevalent with the addition of hard second phases [5]. The stress-strain curves of the Ag/ND composite samples (Figure 5.6 and Table 5.2) follow this behavior. The tensile

5.3. Microhardness and mechanical behaviour

strength, yield strength and stress at fracture increase with increasing ND content, while the uniform elongation, strain at fracture and area reduction of fracture decrease. The UTS for instance increases from 350 MPa for the pure ball-milled HPT-deformed Ag sample to 387, 438 and 531 MPa for the Ag/ND composite samples with 0.1, 0.5 and 2 wt%, respectively. Since all these sample were ball-milled and HPT-deformed with the same parameters, it is reasonable to ascribe the observed UTS increase to the presence of the NDs. Several studies show, that a reinforcement with NDs [102] and also CNTs [104] increases the tensile strength and decreases the ductility of composites compared to pure metals. Both in these studies and in the present work, the mechanical properties of nanocarbon-reinforced MMCs depend heavily on the distribution and the agglomerate size of the second phases. The right choice of the production methods (co-deposition, ball-milling, HPT-deformation) and parameters is therefore paramount to a superior mechanical behaviour.

After tensile testing, fractographs were made with SEM (Figure 5.7). Low magni-

Table 5.2.: Mechanical properties of the tensile test specimens produced from HPT-deformed Ag and Ag/ND composites.

HPT-def. Sample 30 turns	UTS [MPa]	Yield strength [MPa]	Uniform elongation [%]	Stress at fracture [MPa]	Strain at fracture [%]	Area reduction [%]
pure HPT- deformed Ag	329 ± 11	280 ± 10	3.0 ± 0.8	6 ± 2	12.6 ± 1.2	94 ± 4
pure HPT- deformed ball- milled Ag	350 ± 7	303 ± 7	2.2 ± 0.2	166 ± 66	10.1 ± 2.1	74 ± 6
0.1 wt% ND	387 ± 7	324 ± 4	2.5 ± 0.2	247 ± 36	8.8 ± 1.5	66 ± 18
0.5 wt% ND	438 ± 7	352 ± 15	1.9 ± 0.4	404 ± 18	4.2 ± 0.6	21 ± 9
2 wt% ND	531 ± 18	477 ± 10	0.9 ± 0.3	531 ± 18	0.9 ± 0.3	4 ± 1

fication images show that the fracture surface area increases with the ND content from almost complete necking in the pure Ag reference specimen (Figure 5.7 a)

5. Nanodiamond reinforced metal matrix composites

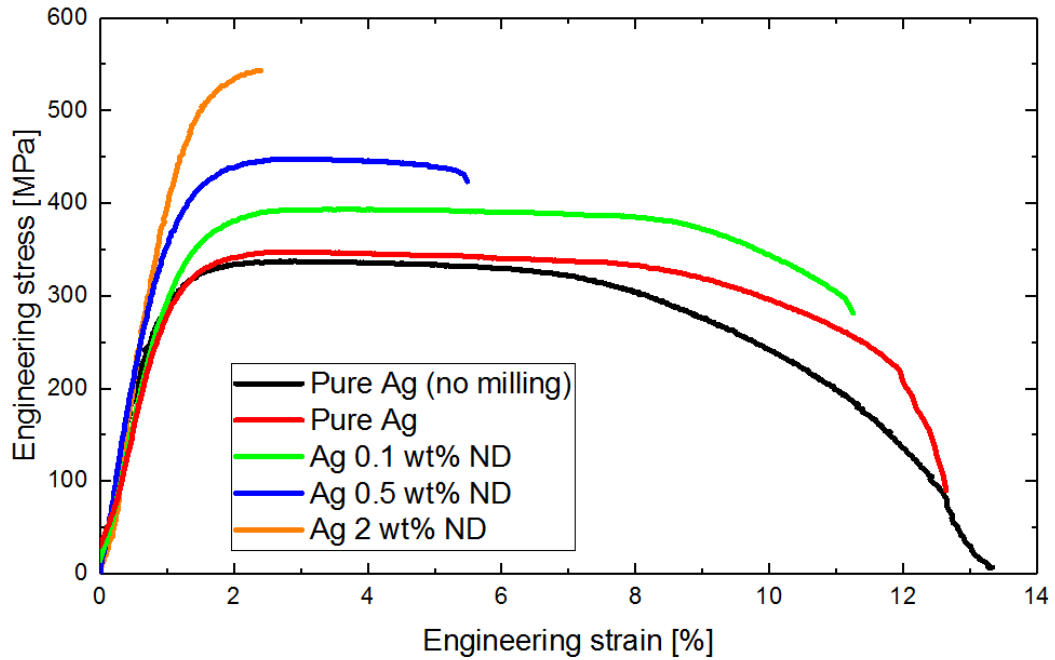


Figure 5.6.: Engineering stress as function of the engineering strain for a pure Ag reference sample, a ball-milled Ag powder samples and ball-milled Ag/ND composite samples with 0.1, 0.5 and 2 wt% ND content, HPT-deformed for 30 revolutions.

with an area reduction of 94 % to a more brittle failure with only a small amount of necking and an area reduction of only 4 % in the 2 wt% Ag/ND composite specimen (Figure 5.7 e). The high magnification images of the fracture surfaces show dimples of various sizes. The diameters of the dimples were measured in the program ImageJ [69] to be 2.0 and 1.2 μm for the two pure HPT-deformed Ag powder specimens, respectively (Figures 5.7 a and b), 486 and 423 nm for the 0.1 wt% and 0.5 wt% Ag/ND composite specimens, respectively (Figures 5.7 c and d) and only 94 nm for the 2 wt% Ag/ND composite specimen (Figure 5.7 e). The ball-milled pure Ag and Ag/ND specimens also show some inclusions of different sizes which are located inside roughly half of the larger dimples visible in the images (arrows in Figure 5.7).

5.3. Microhardness and mechanical behaviour

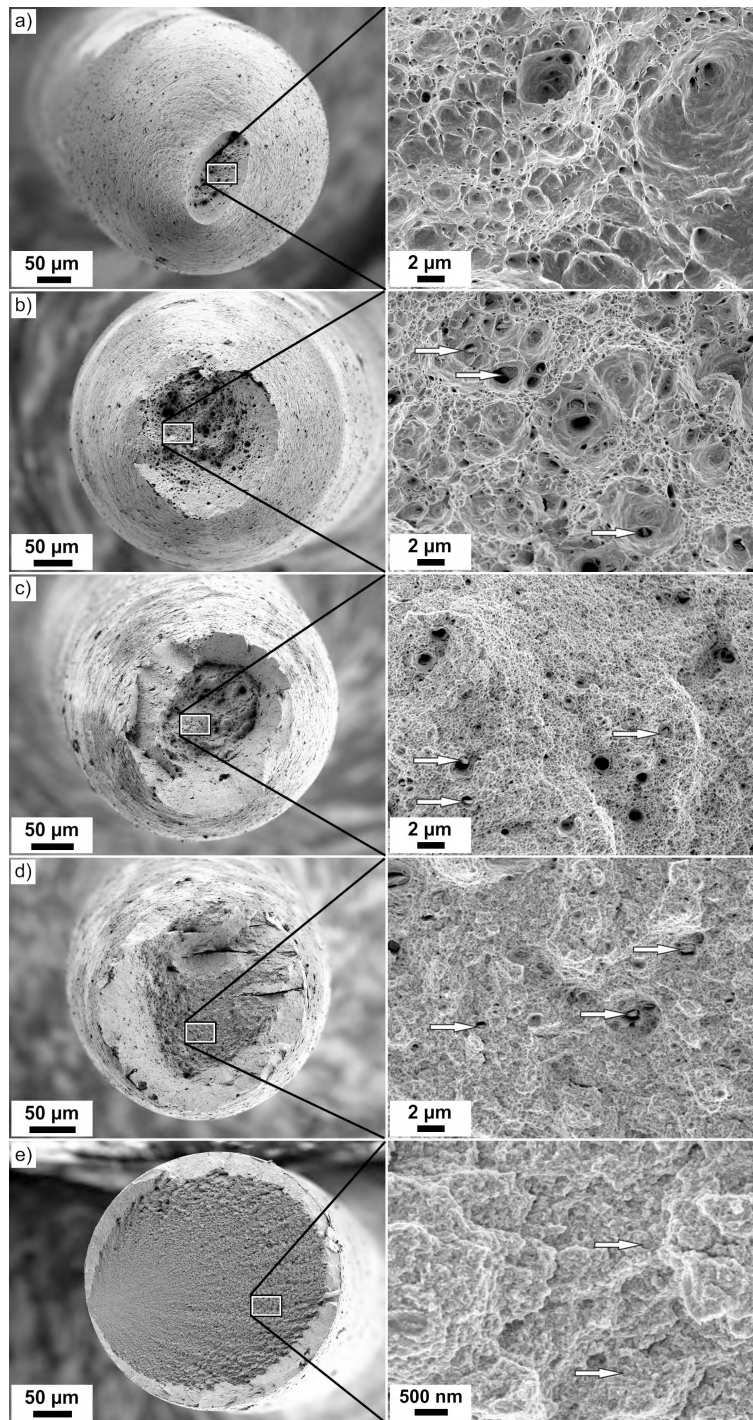


Figure 5.7.: SEM images of fracture surfaces for a) a pure Ag reference sample, b) a ball-milled Ag powder sample and ball-milled Ag/ND composite samples with c) 0.1, d) 0.5 and e) 2 wt% ND content, HPT-deformed for 30 revolutions (arrows indicate inclusions).

5. Nanodiamond reinforced metal matrix composites

The area reduction and morphology of the fracture surfaces are important characteristics of the ductility of a material and depend like the other mechanical properties on the matrix grain size, the size and distribution of the second phase particles and on the bonding between them and the matrix. Large agglomerates of second phase particles have to be thoroughly broken-down and well dispersed in the matrix to minimize the probability of crack initiation inside those agglomerates or at the interface between them and the matrix [109]. Due to the increasing ND content, the area reduction decreases and the fracture surfaces show decreasing dimple sizes (Figure 5.7). The fracture surface of the pure HPT-deformed Ag powder sample (Figure 5.7 a) shows large, deep dimples without any inclusions. The pure ball-milled HPT-deformed Ag powder sample (Figure 5.7 b) has smaller dimples with inclusions (arrows in Figure 5.7 b), probably coming from impurities picked up during the ball-milling process. The fracture surfaces of the 0.1 wt% and 0.5 wt% Ag/ND composite samples (Figure 5.7 c and d) show mainly very small dimples which are slightly deeper in the 0.1 wt% sample, and only a few larger dimples containing $\sim 1 \mu\text{m}$ long inclusions. The 2 wt% Ag/ND composite sample (Figure 5.7 e) shows almost brittle fracture with very small dimples and some smaller ($\sim 200\text{nm}$), more spherical inclusions. In all investigated samples these inclusions are present in approximately half of the larger dimples visible in the micrographs and show no apparent fracture. This indicates that the fracture of the material is initiated by decohesion between the hard particles, which are located at the grain boundaries and triple junctions (see Figure 5.11), and the Ag matrix, and not by particle cracking [86]. The decohesion of particles and matrix leads to the formation of voids in the material, which then grow with increasing tensile stress. When the voids are large enough, they begin to coalesce, a crack forms and ultimately the material fractures [86]. In contrast to the particle decohesion found in this study, Hanada et al. [102] found in Cu ball-milled with 30 at% ND reinforcement and consolidated by spark plasma sintering, that large ND agglomerates showed particle cracking during compression tests. Hot extrusion of those Cu/ND composites on the other hand provided a better dispersion of the ND particle and no particle fracture could be observed. A homogeneous dispersion and a dissolution of the ND agglomerates into small clusters can therefore be seen as essential for a strong and reasonably ductile MMC.

5.4. Microstructure

To show the development of the second phase distribution, depending on the processing parameters and the ND content, SEM micrographs were taken in tangential direction. Figure 5.8 shows the images taken at an equivalent strain of 250 of the pure Ag reference sample (sample 1: no milling) and for the composite samples with varying milling durations (2 hours for samples 2 and 3, 3 hours for samples 5 and 6 and 6 hours for sample 7).

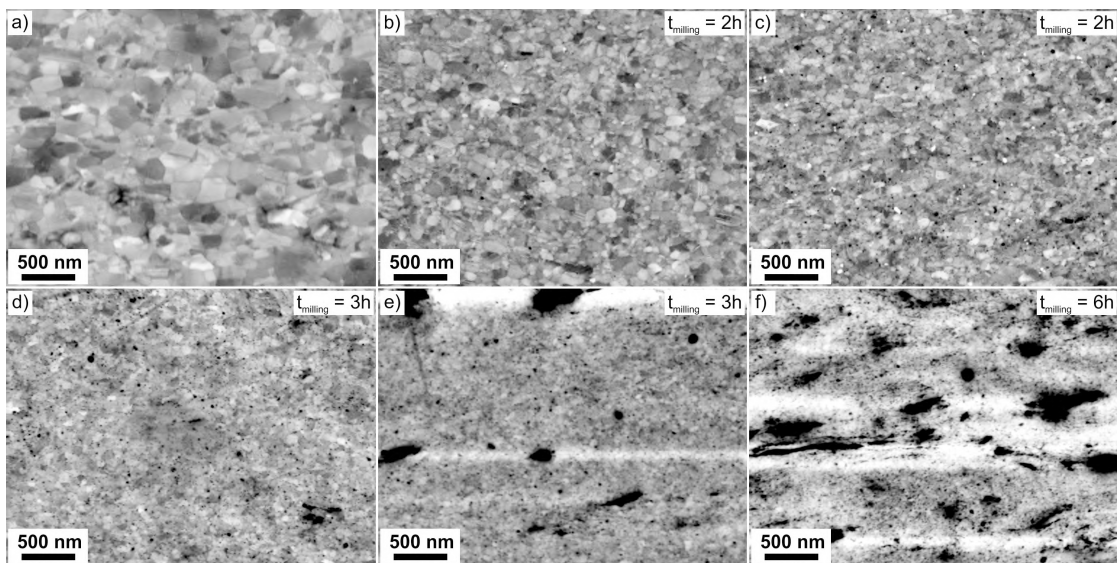


Figure 5.8.: SEM micrographs at $\epsilon_{ps} = 250$ of HPT-disks for a) a HPT-deformed pure Ag reference sample and HPT-deformed Ag/ND composite samples, ball-milled at $\omega_R = 150$ rpm for various times with ND content of b) 0.1 wt%, c) 0.5 wt%, d) 1 wt%, e) 2 wt% and f) 5 wt%.

Figure 5.9 shows the micrographs for the samples ball-milled at 300 rpm (samples 8-11 and 14 in Table 5.1) taken at the same equivalent strain of 250. The grain sizes of the pure Ag reference sample and the Ag/ND composite samples with 0.1 and 0.5 wt% NDs show no significant differences compared to the samples ball-milled with 150 rpm, while the samples with higher ND content have grain sizes below the resolution of the SEM images for both processing conditions (150 rpm and 300 rpm, cf. Figures 5.8 d,e,f and 5.9 d,e). The distribution of the

5. Nanodiamond reinforced metal matrix composites

NDs on the other hand is much better for the samples ball-milled at 300 rpm, especially for higher ND contents (cf. Figures 5.9 d, e).

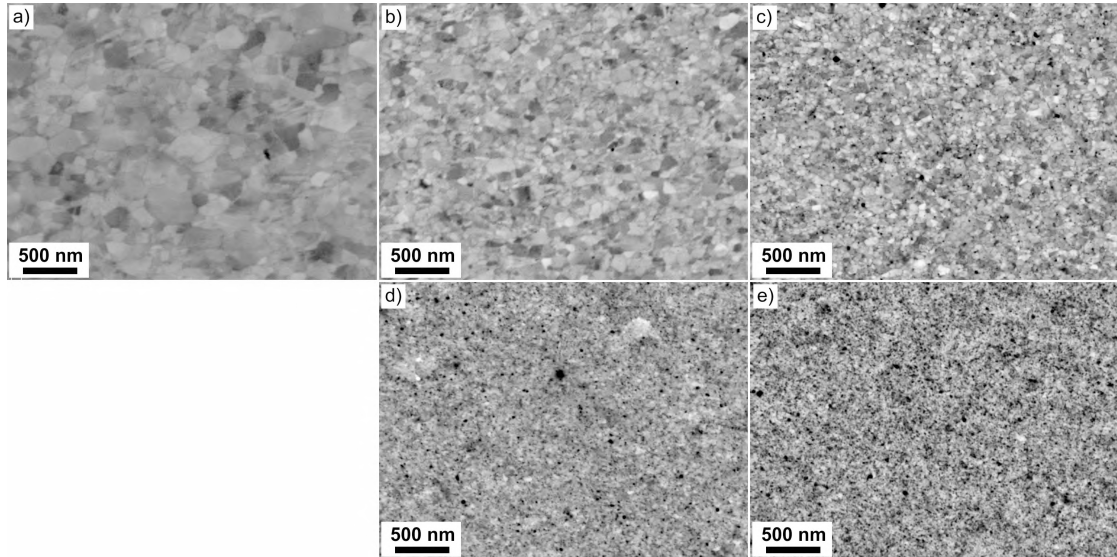


Figure 5.9.: SEM micrographs at $\text{eps} = 250$ of HPT-disks for a) a HPT-deformed pure Ag powder sample and Ag/ND composite samples, ball-milled at $\omega_R = 300$ rpm for 6 hours with ND content of b) 0.1 wt%, c) 0.5 wt%, d) 2 wt% and e) 5 wt%.

To give an example on how the second phase distribution develops over the sample radius, SEM micrographs of the Ag/ND composite sample with 2 wt% NDs ball-milled at 300 rpm taken at 0, 1, 2 and 3 mm from the center are shown in Figure 5.10. The NDs in the sample are relative homogeneously distributed over the whole radius. Only at $r = 0$ mm, there are some larger clusters of ND agglomerates (Figure 5.10 a). The NND, the aspect ratio and the size of the ND clusters were measured with the program ImageJ [69] from the SEM images (Figure 5.10). While the NND and the aspect ratio do not change significantly along the radius (about 35 nm and 1.5, respectively) the diameter of the ND clusters decreases slightly from 17 nm near the center to 11 nm at a sample radius of 3 mm.

Due to the small grain sizes of the Ag/ND composite samples with high ND content

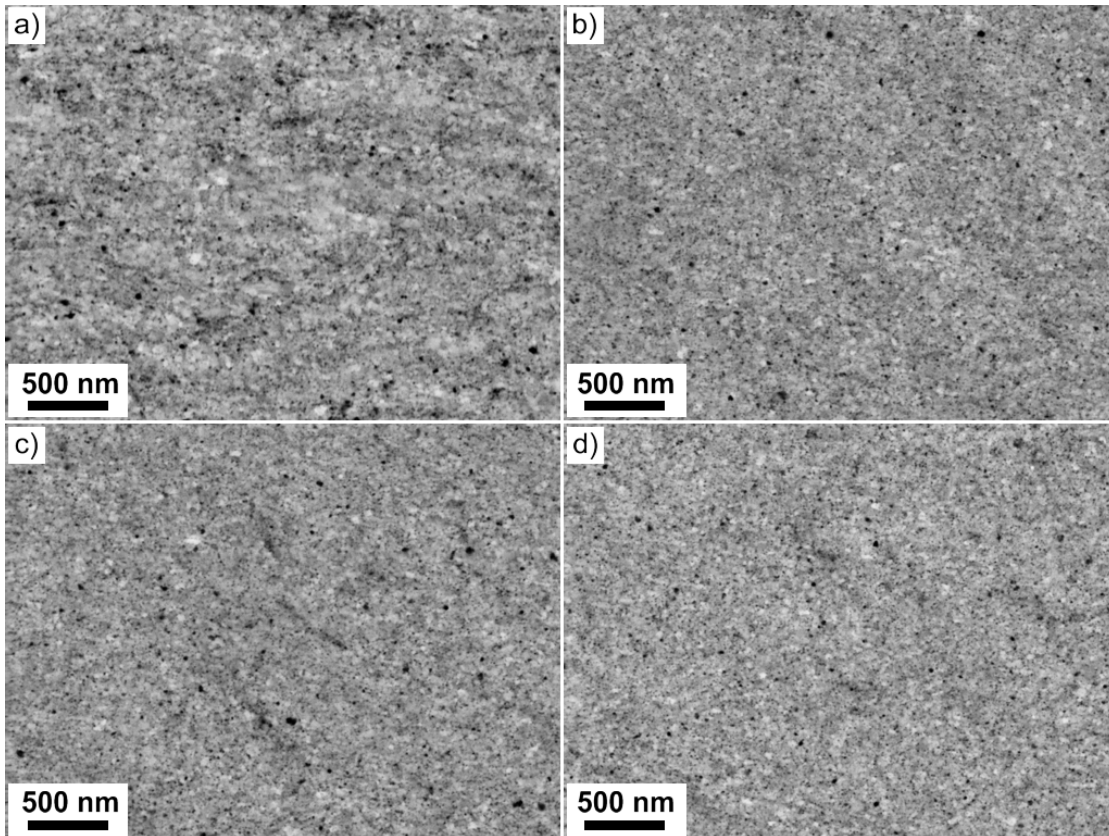


Figure 5.10.: SEM micrographs of a HPT-deformed 2 wt% Ag/ND composite sample, ball-milled at $\omega_R = 300$ rpm for 6 hours, taken at a radius of a) 0 mm, b) 1 mm, c) 2 mm and d) 3 mm.

(> 0.5 wt%) and to investigate the structure of the ND clusters, TEM samples were made from the Ag/ND composite samples with 2 wt% NDs ball-milled at both 150 and 300 rpm. Figure 5.11 exemplarily shows TEM images of the composite samples ball-milled for 3 hours at 150 rpm (sample 6, Figure 5.11 a) and for 6 hours at 300 rpm (sample 14, Figure 5.11 b) and corresponding SAD patterns. Both microstructures consist of equiaxed Ag grains with ND clusters dispersed between the grains. Ag grain sizes were determined from the TEM images as the diameters of equivalent circles of around 300 grains for each sample. They were found to be 49 ± 16 nm for the 150 rpm sample and 43 ± 16 nm for the 300 rpm sample. Figure 5.11 b also includes a HRTEM image of a ND cluster located at

5. Nanodiamond reinforced metal matrix composites

a triple junction. The cluster consists of several single crystal ND particles, indicated by their ordered crystal structure (arrows in Figure 5.11 b), separated by an amorphous carbon grain boundary phase (blue markings in Figure 5.11 b). The recorded SAD patterns show only Ag and no diamond diffraction peaks or peaks from possible impurities.

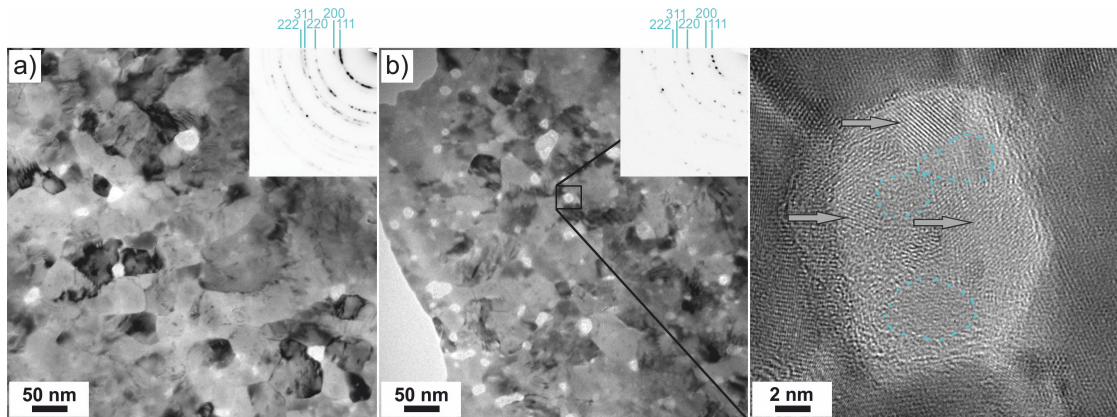


Figure 5.11.: TEM micrographs and SAD patterns for HPT-deformed 2 wt% Ag/ND composite samples ball-milled for a) 3h at 150 rpm and b) 6h at 300 rpm, including a HRTEM image of an ND cluster (arrows indicate possible single crystal ND particles, blue markings indicate amorphous regions).

Ufg or nc grains and a fine dispersion of the NDs inside the matrix play a key role in providing high strength for a composite material. HPT-deformation [5] and ball milling [2] are often-used methods to decrease the grain size and to disperse the second phase particles homogeneously throughout the matrix.

The ball-milling process is the main driving factor for a homogeneous ND distribution. Milling time and velocity are important factors in this regard. A comparison between an only HPT-deformed Ag/ND composite sample with 0.5 wt% NDs, (10 revolutions at RT) and a previously ball-milled Ag/ND composite sample with 0.5 wt% NDs shows that the size of the ND agglomerates is reduced and their distribution inside the matrix is improved through the ball-milling process (c.f. Figure 5.12 and Figure 5.8 c). Increased milling time and velocity have been

5.4. Microstructure

shown to further improve the break-down of large agglomerates and the subsequent dispersion of NDs in the metal powder. Changing the ball-milling velocity from 150 rpm (Figure 5.8) to 300 rpm (Figure 5.9) results in smaller agglomerates which are also better distributed. Several previous studies have also shown that an increased milling time leads to a better second phase distribution and consequently to a higher microhardness of MMCs [91,98–102]. Ball-milling on its own does not however decrease the grain size, as can be seen when comparing the pure HPT-deformed Ag reference sample to the pure ball-milled HPT-deformed Ag sample (Figures 5.8 a and 5.9 a). TEM images (Figure 5.11) of the 2 wt% Ag/ND composite samples ball-milled at different velocities also show no significant difference in the grain size (49 ± 16 nm and 43 ± 16 nm for 150 rpm and for 300 rpm, respectively).

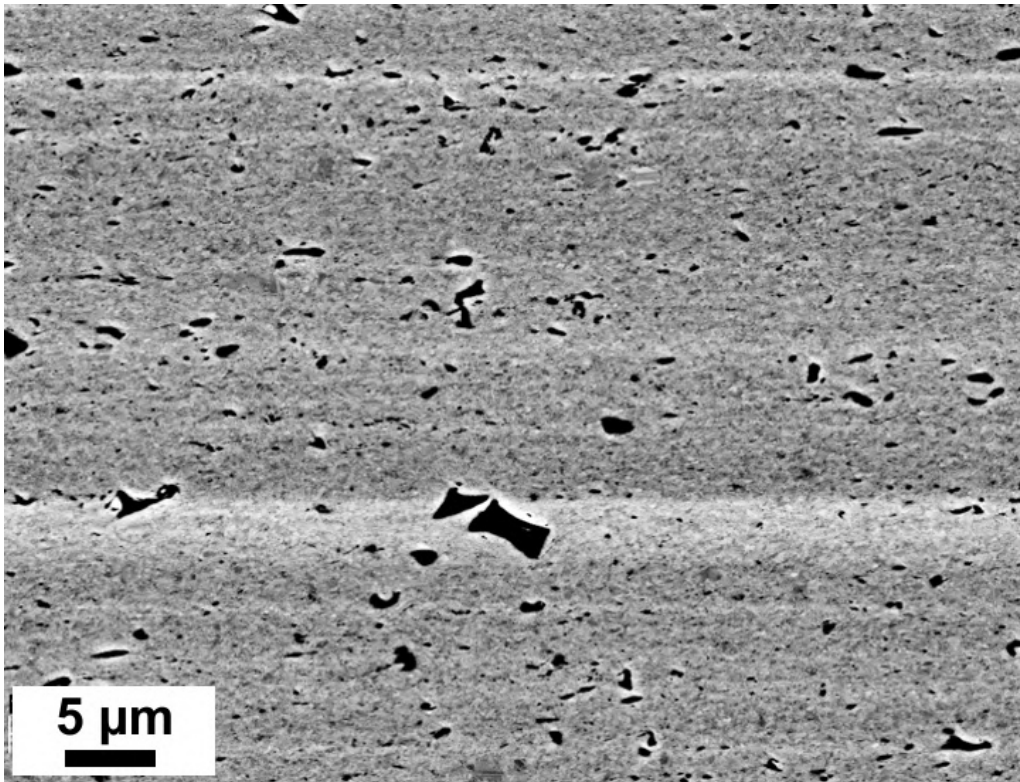


Figure 5.12.: SEM micrograph of a 0.5 wt% Ag/ND composite sample, only HPT-deformed for 10 revolutions at RT.

5. Nanodiamond reinforced metal matrix composites

The goal of the HPT-deformation is to decrease the grain size of the Ag matrix and further improve the ND distribution. Figure 5.10 shows the refinement of the grain size with the sample radius and subsequently the equivalent strain through HPT-deformation (c.f. Figure 5.10 a and b). In pure metals, grain refinement is limited due to grain boundary mobility [4]. In composites, the grain boundary mobility is greatly reduced by the second phase particles [5]. This leads to finer grains in ND reinforced Ag compared to the pure metal, as can be seen in Figures 5.8 and 5.9. Several studies, which investigated ND reinforced MMCs [62, 99, 100, 110], showed that grain refinement plays a key role in providing high strength values and that NDs are able to stabilize the grain size. The influence of the HPT-deformation on the NDs is less prevalent than on the Ag matrix, as with increasing equivalent strain the size of the ND clusters only decreases slightly and the ND distribution shows also only a slight change at low equivalent strains (Figure 5.10 a and b).

During ball-milling and HPT-deformation larger ND clusters get dissolved into smaller particles of about 10 nm diameter. As can be seen in the HRTEM image (Figure 5.11 b), the ND cluster consists in similar parts of ordered diamond structures and of amorphous structures. Studies of the structure of as-produced NDs show that the diamond structure of single NDs is covered by a thin amorphous layer [13, 61, 62], which is a result of the production method [111], and that the NDs form aggregates by covalent bonding [62]. The increased amount of amorphous carbon compared to the as-produced NDs suggests that during ball-milling and HPT-deformation, the NDs are partially damaged and undergo a phase change. As the NDs are Raman active in contrast to the Ag matrix [60, 62], Raman spectroscopy studies can be conducted, to evaluate the damage imposed on the NDs during ball-milling and HPT-deformation. Woo et al. [99] showed that the diamond Raman peak of ND reinforced Al disappeared after ball-milling. They suggest that this is caused by a surface graphitization of the ND particles and that the diamond structure remains in the particle core. A similar effect through HPT-deformation was measured by Aristizabal et al. [25] on Ni MMCs reinforced with CNTs. Here the Raman spectroscopy results showed a fragmentation of the CNTs into graphite/graphene clusters caused by the imposed strain.

Analogous to the Ag/Nd MMCs, images of the Au/ND microstructure were obtained with SEM. Figure 5.13 shows micrographs at $r = 3$ mm of the HPT disks for the pure Au reference powder, the colloidal mixed Au/ND MMC powder with 0.1 and 1 wt% and the ball-milled Au/Nd powder with 0.5 wt%. The Au powder reference sample features a mean grain size of about 120 nm and a multitude of dark spots. As the pure powder does not contain NDs, a possible contamination of the powder either during initial production or consolidation in the HPT has to be considered. The ND reinforced Au samples show an increase in the number of agglomerates and a decrease in the grain size.

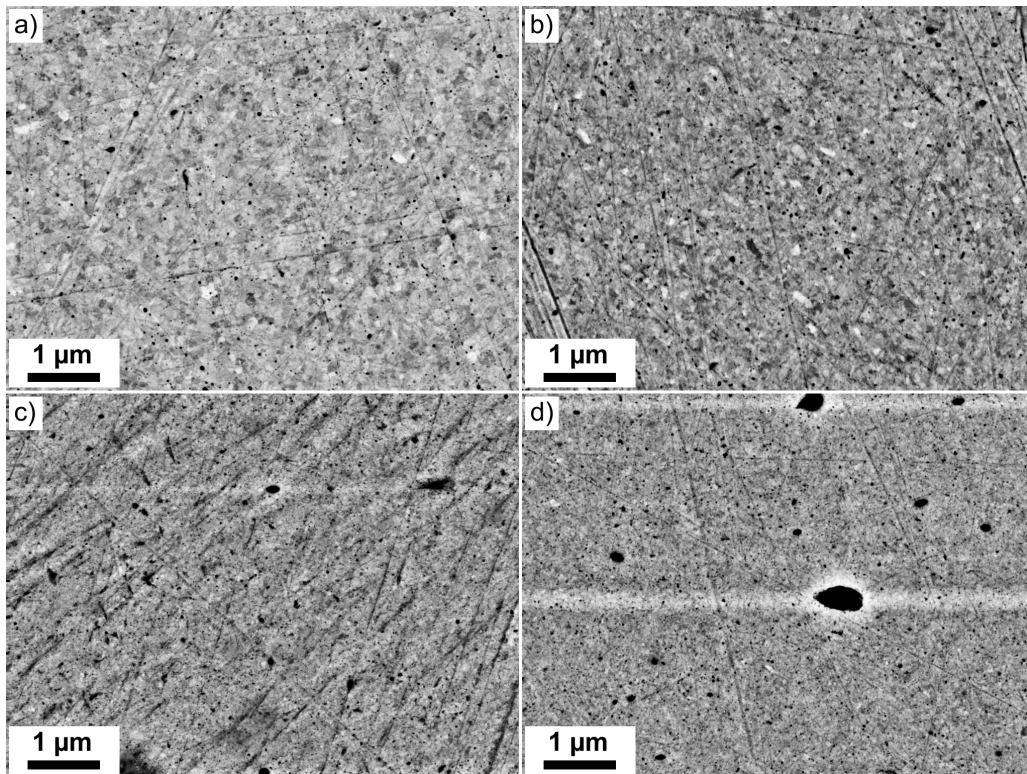


Figure 5.13.: SEM micrographs at $r = 3$ mm of HPT-disks for a) pure Au reference powder, HPT-deformed for 10 revolutions, b) Au powder with 0.1 wt% NDs, colloidal mixed and HPT-deformed for 30 revolutions, c) Au powder with 1 wt% NDs, colloidal mixed and HPT-deformed for 30 revolutions and d) Au powder with 0.5 wt% NDs, ball-milled for 6 hours at 300 rpm and HPT-deformed for 50 revolutions

5. Nanodiamond reinforced metal matrix composites

For the Ni/ND MMCs, SEM micrographs were also taken at a radius of $r = 3$ mm of the HPT-disks. Figure 5.14 shows the microstructure of the 0.5, 1, 3 and 10 vol% samples HPT-deformed for 30 revolutions at RT. With increasing ND content both the grain size and the agglomerate size decrease and the NDs become more homogeneously distributed. Simultaneously, the agglomerates follow a shear-like pattern and the shape of the agglomerates becomes more elongated. In the 10 vol% sample (Figure 5.14 d), the agglomerates are overall much smaller and more round with only remnants of the shear pattern visible.

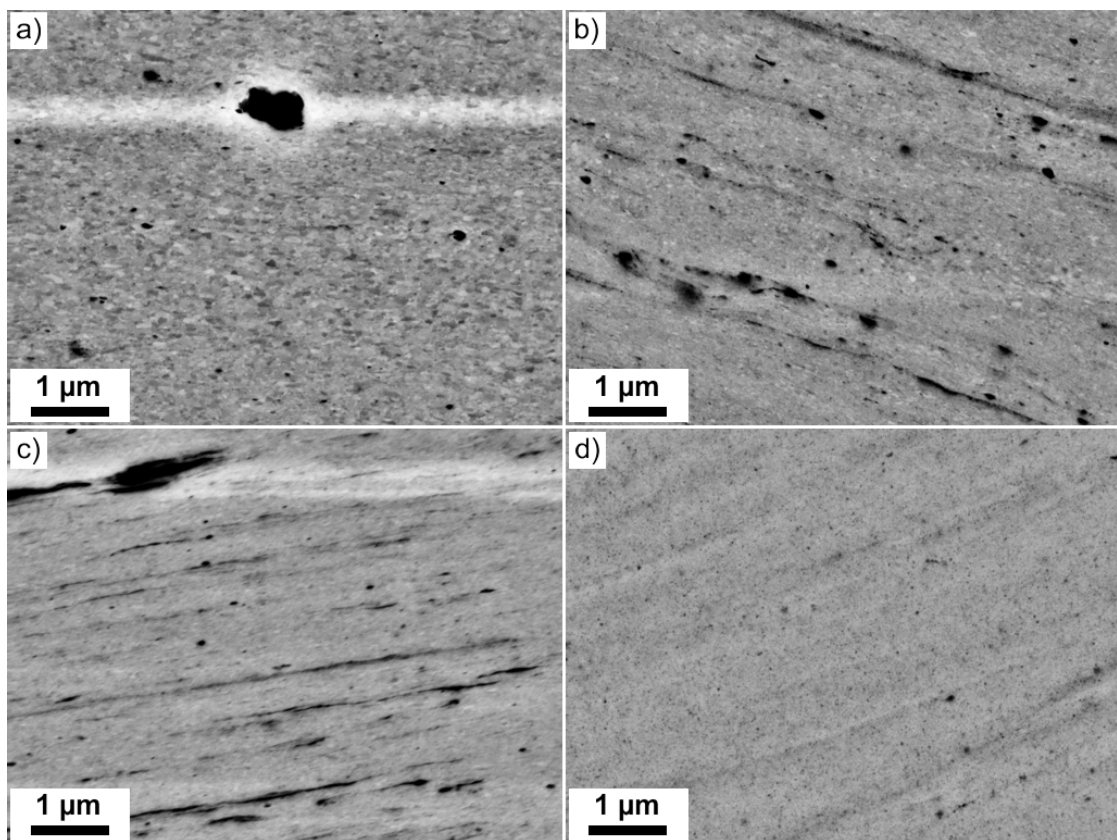


Figure 5.14.: SEM micrographs at $r = 3$ mm of HPT-disks for Ni/ND MMCs with a) 0.5 vol%, b) 1 vol%, c) 3 vol% and d) 10 vol%, all HPT-deformed for 30 revolutions at RT.

6. Strengthening mechanisms in nanocarbon-reinforced metal matrix composites

After outlining how the mechanical properties of the nanocarbon-reinforced MMCs depend on the production parameters in Chapter 4 and Section 5.3, a deeper look at the principal mechanisms controlling this behaviour is needed.

For the Ni/CNT MMCs, the microhardness and the tensile and compression strength as well as the ductility depend on the imposed equivalent strain, the CNT content and the HPT-deformation temperature. For the Ag/ND MMCs, the ball-milling parameters have also a great influence on these properties, while a possible influence of the HPT-deformation temperature was not investigated. For both these MMCs, several different underlying strengthening mechanisms can be proposed as responsible for these property changes.

6.1. Hall-Petch strengthening

The relationship between grain size and yield strength is explained by the Hall-Petch theory, which states that the yield strength σ_y is related to the grain diameter d by:

$$\sigma_y = \sigma_0 + k * \frac{1}{\sqrt{d}} \quad (6.1)$$

with σ_0 and k material-dependant constants [112]. This relation between grain size and strength has been shown to be valid for many different metals and several orders of magnitudes of grain sizes [113]. To evaluate if the Ni/CNT MMCs

6. Strengthening mechanisms in nanocarbon-reinforced metal matrix composites

investigated in this work follow the Hall-Petch relation, the measured Vickers microhardness values of all samples, as summarized in Table 4.1, are drawn as a function of $1/\sqrt{d}$ in Figure 6.1. The microhardness was used for this graph instead of the yield strength, because specimens from samples deformed at RT were not included in the tensile tests due to the often observed crack formation during HPT-deformation and samples deformed at 200°C and at 400 + 200°C displayed a large scatter in the tensile test data due to their brittle failure in the elastic regime. The microhardness can be used for a Hall-Petch plot due to the Tabor relation between yield strength and microhardness, which states that the Vickers microhardness is about three times the yield strength, both measured in MPa [83].

The grain sizes used for this comparison were measured from TEM images for the 2wt% samples (c.f. Figure 3.6) and from SEM images for all other samples (c.f. Figure 3.4), using the equivalent diameter method. Despite some deviations at smaller grain sizes, the Ni/CNT MMCs follow the Hall-Petch relations rather good. A linear approximation was fitted onto the results with the fitting parameters being $y = 49 + 4909*x$, which equals a σ_0 of 160 MPa and a k of 507 MPa $\mu m^{1/2}$.

These results, showing that HPT-deformed Ni/CNT MMCs follow the Hall-Petch relation, were compared to similar results obtained for carbon doped HPT-deformed Ni by Rathmayr and Pippan [45]. In Figure 6.1 the microhardness values for Ni samples doped with four different concentrations (8, 100, 300 and 1200 ppm) are plotted besides the results for the Ni/CNT MMCs. Again, a linear approximation was fitted onto the results with the fitting parameters being $y = 0 + 5975*x$, which equals a σ_0 of 0 MPa and a k of 618 MPa $\mu m^{1/2}$. Similar Hall-Petch relationships between the grain size and the microhardness were found in CNT-reinforced Ni at larger grain sizes by Suarez et al. [68], in CNT-reinforced Cu by Kim et al. [114], and in CNT-reinforced Al by Choi et al. [115]. These results strengthen the argument, that the microhardness increase of Ni/CNT MMCs is mainly the result of a decreased grain size through HPT-deformation.

Like for the Ni/CNT MMCs, the relationship between grain size and yield strength

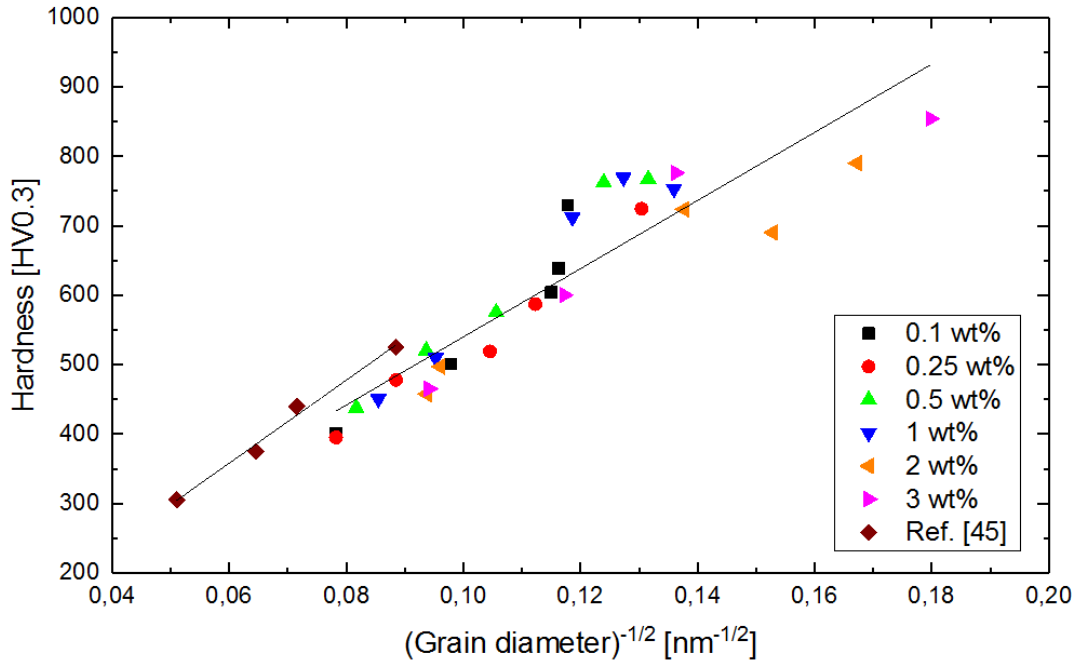


Figure 6.1.: Hall-Petch Plot and linear fit for HPT-deformed Ni/CNT samples and HPT-deformed C doped Ni samples [45] (redrawn from Publication B).

of the Ag/ND MMCs is explained by the Hall-Petch theory (Equation 6.1). Figure 6.2 shows the yield strength measured in the tensile tests (Figure 5.6 and Table 5.2) as a function of the grain size. The grain sizes were measured from SEM images (Figure 5.9) for the pure Ag samples and the Ag/ND composite sample with 0.1 wt% and from TEM images (Figure 5.11) for the Ag/ND composite samples with 0.5 and 2 wt%. The yield strength increases with decreasing grain size and a linear fit could be modelled which follows the Hall-Petch relation (Figure 6.2). The fitting parameters are $y = 76 + 2430 * x$, which equals a σ_0 of 76 MPa and a k of 77 MPa $\mu m^{1/2}$. Comparisons of the measured yield strength and the predicted yield strength using the Hall-Petch equation (equation 1 in Ref. [113]) are also in good agreement (Table 6.1). For these calculations, the measured grain sizes and the constants of pure silver ($\sigma_0 = 29 \pm 3$ MPa, $k = 100$ MPa $\mu m^{1/2}$ [113,116]) were used, hence the slightly different values compared to the linear fit (c.f. Table 6.1 and Figure 6.2). These results indicate, that strengthening by grain refinement

6. Strengthening mechanisms in nanocarbon-reinforced metal matrix composites

is the main contributor for the observed yield strength of the Ag/ND MMCs. This hardening by grain refinement can be achieved by HPT-deformation [1], as well as by mechanical alloying through ball-milling [2, 91]. The contributions of ball-milling and HPT-deformation to the microhardness increase can be seen in Figures 5.8 and 5.9. Ball-milling and compaction of Ag powder with 0.5 wt% NDs result in a microhardness of about 77 HV0.1 for the 150 rpm sample and 94 HV0.1 for the 300 rpm sample. Additional HPT-deformation increases the microhardness further to about 130 and 140 HV0.1 for the 150 rpm and 300 rpm sample, respectively. The microhardness difference of the compacted powders is most likely caused by a stronger size reduction and better distribution of the ND clusters in the Ag powder particles after ball-milling with 300 rpm. This also leads to the microhardness difference of 10 HV0.1 after HPT-deformation.

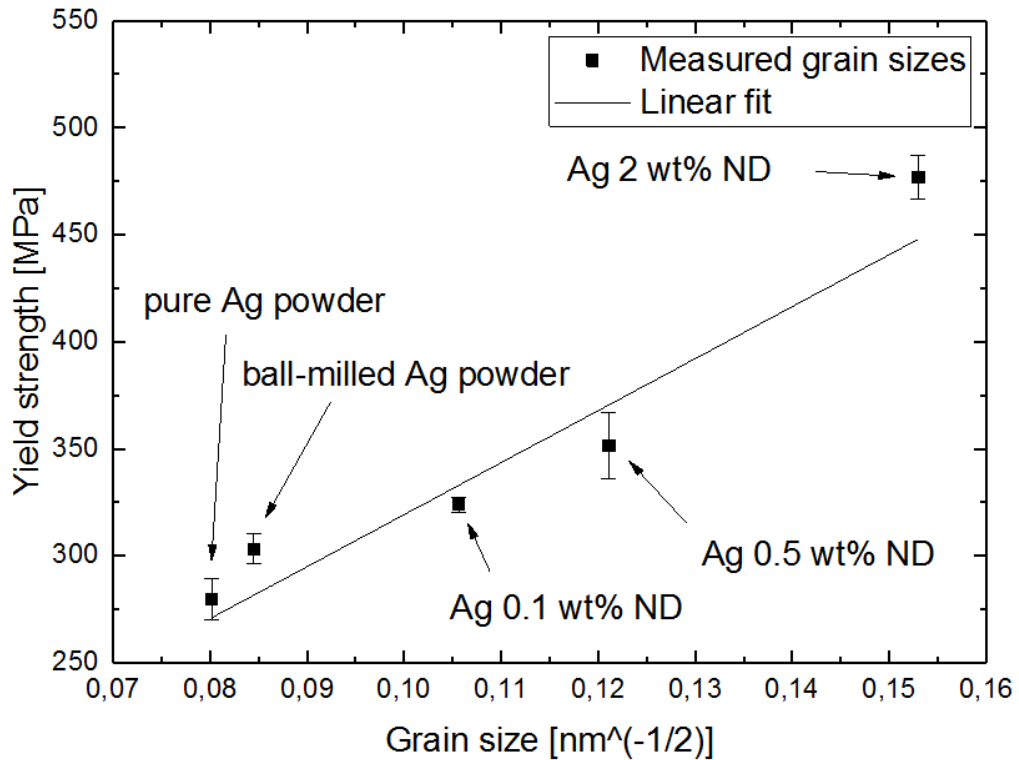


Figure 6.2.: Hall-Petch Plot and linear fit for pure HPT-deformed Ag powder samples and HPT-deformed Ag/ND composite samples.

Table 6.1.: Measured yield strength and calculated strength values for the Hall-Petch strengthening mechanism of HPT-deformed Ag powder samples and Ag/ND composite samples.

HPT-deformed sample 30 turns	Measured Yield strength [MPa]	Hall-Petch strength component [MPa]
Pure Ag powder	280 ± 10	283 ± 3
Ag powder ball-milled	303 ± 7	296 ± 3
0.1 wt% ND	324 ± 4	363 ± 3
0.5 wt% ND	352 ± 15	412 ± 4
2 wt% ND	477 ± 10	513 ± 4

6.2. Dislocation strengthening

Dislocations introduced through plastic deformation are called geometrically necessary and contribute to strengthening by acting as individual obstacles and by creating a long range back stress in coarse-grained materials [117]. In severely deformed ufg and nc materials these dislocations are however not evenly distributed in the microstructure, but concentrated mainly in boundaries. These boundaries subdivide the initial grains and lead to grain refinement with further HPT-deformation [4, 67]. The dislocation density has therefore only an indirect influence on the strength of HPT-deformed materials through furthering the grain refinement.

In the Ag/ND MMC powders, which were subjected to ball-milling before consolidation and HPT-deformation, dislocations are additionally introduced through the ball-milling process [2]. As dislocations are needed to create sub-grains, these additional dislocations can accelerate the grain refinement both during ball-milling and in the subsequent HPT-process and allow the microstructure and therefore the microhardness to reach its saturation with fewer HPT-revolutions. This can be seen by comparing the microhardness evolution with the equivalent strain of the Ni/CNT MMCs and the Ag/ND MMCs (Figures 4.3 and 5.3, respectively), both HPT-deformed for 30 revolutions at RT. While the Ni/CNT MMC sample reaches saturation of the microhardness only at an equivalent strain value of 250,

6. *Strengthening mechanisms in nanocarbon-reinforced metal matrix composites*

the Ag/ND MMC sample show a microhardness saturation over the whole sample radius.

6.3. Reinforcement strengthening

Besides the relation between grain size and microhardness/tensile strength, there is also a dependence of the microhardness on the CNT content, mainly at elevated HPT-deformation temperatures. Figure 6.3 shows the saturation microhardness values for all samples depending on the fourth root of the carbon content and the HPT-deformation temperature. These values are additionally compared to microhardness values for Ni, doped with different amounts of pure carbon and HPT-deformed at RT and 400°C, as published by Rathmayr and Pippan in 2011 [45].

At RT, the carbon content has no significant influence on the microhardness as was already shown in Figure 4.4. At an HPT-deformation temperature of 200°C, the CNT content has an apparently stronger influence on the microhardness. This is due to about 150 HV0.3 lower microhardness values of the 0.1 and 0.25 wt% samples compared to RT. The samples with ≥ 0.5 wt% CNTs on the other hand show only a slight decrease in the microhardness. At 300°C and 400°C, a more steadily increase of the microhardness with the CNT content can be seen, with values about 200 and 300 HV0.3 below the RT values, respectively. The slopes of these increases are smaller than for 200°C but not completely flat as for the RT samples. The 400 + 200°C samples show the largest increase with CNT content, mainly because the 0.1, 0.25 and 0.5 wt% samples have microhardness values between 500 and 600 HV0.3, while the 1, 2 and 3 wt% sample are between 750 and 850 HV0.3. The dependence of the microhardness on the carbon content is vastly different for the carbon-doped Ni samples of Ref. [45]. While the microhardness values are much lower, the increase with the carbon content is much stronger for both the samples HPT-deformed at RT and at 400°C.

There are two ways how hard reinforcement phases can increase the strength of a material. The first mechanism works by forcing moving dislocations to bow around the particles. This bowing is known as dispersion or Orowan strengthening [3, 5].

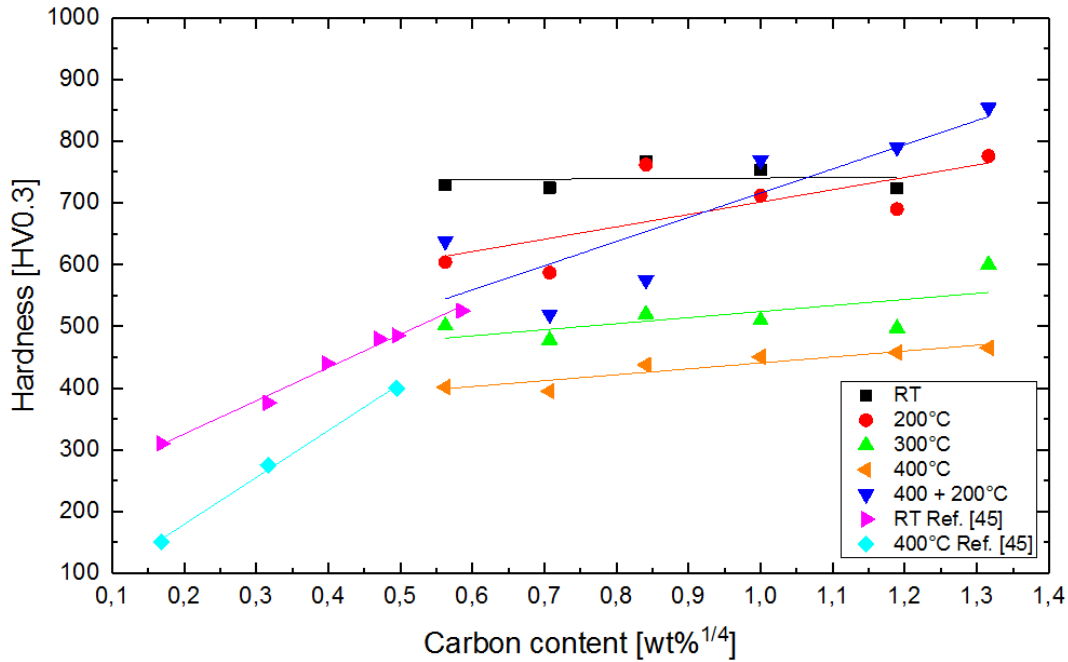


Figure 6.3.: Saturation hardness as function of the carbon content for HPT-deformed Ni/CNT samples and HPT-deformed C doped Ni samples [45]. (redrawn from Publication B).

But this strengthening mechanism can only occur, if the second phase is present inside the grains and smaller than the matrix grain size [118]. CNT agglomerates larger than the grain size would not contribute substantially to the strength of the MMCs. In Figure 3.6 the CNT agglomerates are shown to be either similar in size to the Ni grains (Figures 3.6 a and d), or smaller (Figures 3.6 b and c). They are however only present at the grain boundaries or the triple junctions of the Ni matrix and not inside the grains. Dislocation movements are therefore primarily hindered by grain boundaries and not by the CNTs and the contribution of Orowan strengthening to the strength of the Ni/CNT MMCs is very small or even negligible.

Another way, how the CNT agglomerates can increase the strength is by pinning of the grain boundaries, which allows the formation of finer saturation grain

6. *Strengthening mechanisms in nanocarbon-reinforced metal matrix composites*

sizes during HPT-deformation. This stabilization of finer grains compared to pure HPT-deformed metals is caused by a decrease of the grain boundary mobility by impurities or reinforcement particles located at the grain boundaries and triple junctions [4, 5].

The cause for the different slopes for carbon doped Ni compared to the Ni/CNT MMCs as well as for the different HPT-deformation temperatures is probably the capability of the reinforcing phases to influence the grain boundary mobility. Rathmayr and Pippan [45] showed that the carbon has a larger effect on the final grain size after HPT-deformation at higher temperatures. This can be seen in Figure 6.3 both for carbon doped Ni and for the Ni/CNT MMCs. The difference in the slopes between these two material systems can be caused by the difference in the second phase distribution. While atomic carbon can easily be distributed along the grain boundaries during HPT-deformation, the CNTs are concentrated in larger agglomerates. This was also shown by Aristizabal et al. [26] with HPT-deformed Ni/CNT MMCs, where the diameter and the nearest neighbour distance of the CNT agglomerates decreased with increasing strain, but the CNT area fraction did not change significantly with increasing strain values. Thus, it can be concluded that the carbon is mostly present as CNTs in the agglomerates and might be only to a small part enriched at the grain boundaries. However, the amount of atomic carbon present at the grain boundaries could not be determined as of yet. Future investigations with atom probe microscopy could reveal how much carbon is detached from the CNTs and enriched at the grain boundaries.

The usage of NDs as reinforcement phases also results in an increase of the microhardness, as can be seen by comparing the microhardness of the pure Ag reference sample, the pure ball milled Ag sample and the Ag/ND composite samples ball-milled both at 150 rpm and 300 rpm (Figures 5.8 and 5.9). While there is no significant difference in the microhardness of the pure Ag reference sample and the pure ball milled Ag sample after HPT-deformation, the microhardness increases substantially with the increase in ND content. With a higher ball-milling velocity an additional microhardness increase can be observed for all Ag/ND composite samples. These observations show that the ball-milling amplifies the effect of the

NDs on the microhardness and the grain size through dissolving and distributing the ND clusters in the Ag matrix. Several studies confirm this observed microhardness increase through ND addition both for metals [13, 98–102, 109, 110] and for polymers [119]. NDs as reinforcements have also been shown to give higher microhardness compared to other carbon derivatives such as CNTs or carbon onions [62].

TEM images of the Ag/ND MMC microstructure (Figure 5.11) show that the ND particles, like the CNTs in the Ni matrix, are located at the grain boundaries and triple junctions of the Ag matrix. The Orowan strengthening mechanism can therefore, like in the Ni/CNT MMCs, not be used for the Ag/ND MMCs, since the ND particles are not located inside the grains, and the microhardness increase is caused by a stronger grain refinement due to the pinning effect of the NDs [4, 5].

6.4. Load transfer strengthening

Another factor in providing high microhardness and strength for MMCs is the load transfer between the matrix and the second phase. A good bonding and a high aspect ratio are necessary for an efficient load transfer from the softer matrix to the harder reinforcement phase [3]. With a modified Shear Lag model, introduced by Nardone and Prawo [120], the contribution of the load transfer strengthening in MMCs can be calculated as

$$\Delta\sigma_{LT} = \nu_P * \sigma_m * \left[\frac{(l + t) * A}{4 * l} \right] \quad (6.2)$$

with ν_P the particle volume fraction, σ_m the yield strength of the unreinforced matrix, l and t the length and width of the reinforcing particles, and A their aspect ratio [121].

Exemplary calculations of the load transfer contributions to the tensile strength of the Ni/CNT MMCs with 2 wt% CNT content give $\Delta\sigma_{LT}$ values between 18.0 ± 9.5 MPa for the sample HPT-deformed at 200°C and 15.1 ± 7.0 MPa for the sample HPT-deformed at 400+200°C. The value for σ_m is given as 148 MPa [122] and the values for l , t and A were taken from the measurements discussed in Section 4.4.

6. Strengthening mechanisms in nanocarbon-reinforced metal matrix composites

With aspect ratio values smaller than 2 and particle volume fractions of 8.33 vol%, the contribution of the load transfer to the tensile strength of the Ni/CNT MMCs is very small (c.f. Figures 4.7 and 4.8).

Similar results can be obtained for the Ag/ND MMCs. HRTEM images of Ag/ND composite samples with 2 wt% NDs (Figure 5.11 b) indicate, that ball-milling for 6h at 300 rpm and subsequent HPT-deformation leads to small, round ND clusters. The aspect ratios were determined to be around 1.5 for the 0.1, 0.5 and 2 wt% samples, which were used for tensile testing, while σ_m is given as 29 MPa [116]. The $\Delta\sigma_{LT}$ values are 0.08 ± 0.03 MPa for 0.1 wt%, 0.43 ± 0.18 MPa for 0.5 wt% and 1.77 ± 0.77 MPa for 2 wt% ND content. These values show that the load transfer has no significant influence on the tensile strength of the Ag/ND MMCs (c.f. Table 6.1).

6.5. Impurities and solid solution strengthening

The strengthening of the material through solid solution hardening through carbon atoms as well as the introduction of impurities during colloidal mixing have also to be considered when evaluating the contributing factors to the strength. The solid solution of carbon in Ni and the formation of Ni_3C in Ni/CNT MMCs has been investigated by Suarez et al [123]. They cited a maximum solubility of carbon in Ni of 0.56 wt% at 1600 K (1327°C) [124] and showed that Ni_3C is a metastable phase up to 1600°C. They also found no evidence for the formation of the hcp Ni_3C phase in both the HT-XRD spectra of 5 wt% Ni/CNT MMCs and in the SAD pattern of a fcc Ni matrix at the interface to a CNT cluster. The SAD pattern of an HPT-deformed Ni/CNT MMC sample with 1 wt% CNT content (Figure 3.3) also shows only a Ni fcc structure and no hcp phase. It can be therefore concluded that colloidal mixing, sintering and HPT-deformation does not lead to the formation of Ni_3C .

The influence of other impurities apart from carbon on the mechanical properties of HPT-deformed Ni has been investigated by Rathmayr and Pippan [45] for different Ni samples with carbon contents between 8 and 1200 ppm and total im-

6.5. Impurities and solid solution strengthening

purity contents between 41 and 3130 ppm. They found that the UTS is mainly influenced by the carbon content, while the ductility is governed by non-metallic inclusions. Bachmaier et al. [80], on the other hand, found an increase in the saturation microhardness in Ni powder and more so in oxidized Ni powder after consolidation and HPT-deformation compared to HPT-deformed bulk Ni. This microhardness increase was a result of the grain boundary pinning of the oxide particles. The Ni powder used in this work has not been oxidized, and the equivalent strain value where microhardness saturation is reached is similar to that of the pure Ni powder [80]. It is therefore reasonable to conclude that the microhardness increase from 290 HV1 for the bulk Ni to 570 HV1 for the pure Ni powder is due to the presence of oxides and that the further increase to at least 724 HV0.3 for the Ni/CNT MMCs (Table 4.1) can be ascribed to the CNT reinforcement.

For the Ag/ND MMCs, ball-milling is another way for the introduction of impurities into the material. As the ND clusters are dissolved during ball-milling and HPT, single C atoms could be removed from the particles and distributed throughout the Ag matrix [125]. As the solubility of carbon in Ag is lower than 0.1 at% [126], solid solution strengthening would only be possible through forced mixing during ball-milling and HPT-deformation. Hydrogen and oxygen from the atmosphere and Fe from the milling jars are the main impurity elements that can lead to a strength increase in the final composite material. The milling time and velocity, the milling atmosphere as well as the microhardness difference between powder and milling medium are all important factors in this regard [2]. SAD patterns of the 2 wt% Ag/ND MMC samples ball-milled for 3 hours at 150 rpm and for 6 hours at 300 rpm (Figures 5.11 a and b, respectively) show only peaks of pure Ag. Since SAD measurements only cover very small areas, possible Fe or Ag₂O impurities could not be detected. Two possible indicators for impurities introduced through ball-milling are the higher microhardness of the compacted Ag/ND composite sample with 0.5 wt% NDs ball-milled at 300 rpm compared to that ball-milled at 150 rpm (Figures 5.2 and 5.3) and the presence of inclusions in the fracture surface of the pure ball milled Ag sample (Figure 5.7 b). Future evaluations with energy dispersive X-ray spectroscopy (EDX) over larger sample areas will determine if there are small amounts of Fe dissolved in the compos-

6. Strengthening mechanisms in nanocarbon-reinforced metal matrix composites

ites. Also possible are X-ray diffraction (XRD) measurements to evaluate possible lattice parameter changes of Ag due to impurities.

7. Summary

In this thesis, nanocarbon-reinforced MMCs were deformed by HPT at various temperatures. High equivalent strains can be used with this method for decreasing the grain size of bulk materials, generating new mechanically alloyed materials, compacting and deforming powders and homogenizing the distribution of second phases inside matrix materials. MMCs are combinations of a softer metal matrix and a harder reinforcement phase. Carbon allotropes, such as CNTs and NDs, are well suited as reinforcement phases of MMCs, but only if their tendency to form large agglomerates can be overcome. HPT-deformation is the perfect method to dissolve such large agglomerates and distribute the particles in the matrix. The goal in this work was to improve the second phase distribution and to decrease the grain size of the matrix materials. An increase in hardness and tensile strength without a too strong decrease in ductility has been expected from these experiments.

In the following the main experimental results are summarized and then the conclusion for the design and processing of this type of composites are drawn. Ni/CNT MMCs were produced from powder by colloidal mixing and sintering. HPT-deformation of the sintered pellets was done at RT, 200°C, 300°C, 400°C and with a two-temperature deformation process (400 + 200°C). The increase in the number of revolutions and subsequently the equivalent strain leads to a grain refinement of the Ni matrix. The size and the distributions of the CNT agglomerates does not change significantly between 1 and 30 HPT-revolutions. The microhardness of the Ni/CNT MMCs increases until it reaches a saturation value. For 1wt% CNT content this saturation was reached after 30 revolution or an equivalent strain of ϵ_{eq} of about 250.

7. Summary

With increasing CNT content, the microstructure of the Ni/CNT MMCs, HPT-deformed at RT for 20 revolutions, showed more and larger CNT agglomerates, while the grain sizes showed no significant difference between the samples. They also reach similar saturation microhardness values independent of the CNT content, with the exception of the samples with 3 wt%. These samples could not be deformed for more than 2.5 revolutions, because of slippage between the anvils due to a high microhardness and high CNT content.

SEM images and TKD scans indicate that the grain sizes increase with increasing HPT-deformation temperature, while the grain sizes of the sample deformed at two temperatures (400 + 200°C) are similar to those of the 200°C sample (Figure 3.7). HRTEM images show agglomerates of strongly deformed CNTs getting smaller and more spherical with increasing HPT-deformation temperature. The saturation microhardness decreases, microhardness values above 700 HV0.3 at RT and about 400 HV0.3 after HPT-deformation at 400°C. The two-temperature deformation process (400 + 200°C) on the other hand increases the saturation microhardness up to 800 HV0.3.

Evaluations of the texture show a fcc shear texture independent of the HPT-deformation temperature, with a concentration of grain orientations in [111]-direction. Annealing experiments show that the two-temperature process is advantageous for maintaining smaller grains and smaller CNT cluster sizes as well as a higher microhardness after annealing, most likely due to a more homogeneous CNT distribution.

Similar to the microhardness, the tensile strength, the compression strength and the anisotropy of Ni/CNT MMCs decrease with increasing HPT-deformation temperature and increase also after the two-temperature deformation process. The ductility increases with increasing HPT-deformation temperature. The specimens with lower than 1 wt% CNTs also showed some ductility after the two-temperature deformation process.

Ag/ND composite samples were produced from powders by ball-milling and HPT-

deformation. The ND weight percentages as well as the milling time, the milling velocity and the number of HPT revolutions were gradually increased to increase the microhardness, decrease the grain size of the Ag matrix and to improve the second phase distribution. The addition of a maximum of 5 wt% NDs has been found to increase the microhardness up to 186 Vickers compared to 105 Vickers of the pure Ag reference sample. A ball-milling time of 6 hours at a velocity of 300 rpm and a subsequent compaction and HPT-deformation for 30 revolutions has been found to achieve fully saturated microhardness values. Tensile tests of pure HPT-deformed Ag samples and Ag/ND composite samples revealed an increase of the strength, but also a decrease of the ductility for increasing ND content compared to the pure Ag reference sample. While an increased ND content increases the size of the ND agglomerates and decreases the grain size to a certain extent, a higher ball-milling velocity and a higher equivalent strain have a much greater influence on grain size and ND agglomerate size and distribution.

Several concentrations of NDs have been mixed with Au powder either by colloidal mixing (0.1, 1 wt%) or by ball-milling (0.5 wt%) and compared to pure Au powder. After HPT-deformation, the MMCs showed an increase in microhardness of 20, 50 and 80 HV0.1 (0.1, 1 and 0.5 wt%, respectively) compared to pure Au. While the microstructure of pure HPT-deformed Au features some dark spots, possibly stemming from contamination of the powder, the number and size of spots increase with increasing ND content. Simultaneously, the grain size of the Au matrix decreases.

The microhardness of Ni reinforced with 0.5, 1, 3 and 10 vol% NDs was measured after HPT-deformation at RT and at various temperature combinations. The ND content was the main factor controlling the grain size and the microhardness of the HPT-deformed samples. The two-temperature deformation processes provided only a small microhardness increase compared to the samples HPT-deformed at RT (Figure 5.5). The microstructures of HPT-deformed Ni/ND MMCs feature decreasing grain sizes with increasing ND content. The ND agglomerates get smaller and more homogeneously distributed with increasing ND content in contrast to the other investigated MMC materials, where an increased second phase

7. Summary

content leads to larger agglomerates and no improvement in the distribution when HPT-deformation has been performed at the same temperature and with the same number of revolutions.

The main conclusions from these experimental results are:

- Increasing strength and hardness through increased equivalent strain during HPT-deformation and higher reinforcement content, induced by a decrease in grain size.
- Decreasing ductility concurrent with the increasing strength, caused mainly by the increase in content of agglomerates.
- Dissolution of reinforcement agglomerates during HPT-deformation through particle debonding at the agglomerate surface, as illustrated in Figure 7.1.
- Saturation of the agglomerate dissolution due to high bonding forces between particles in small agglomerates.
- Higher HPT-deformation temperatures result in larger grain sizes and improved agglomerate dissolution, most probable due to the higher strain rate sensitivity and the resulting more homogeneous deformation.
- A two-temperature HPT-deformation process permits the optimization of the microstructure by combining the improved agglomerate dissolution at higher temperatures with the grain size decrease at lower temperatures.
- Better dissolution of NDs than CNTs due to smaller individual particles with lower aspect ratio and ball-milling prior to the HPT-deformation process.

The evaluation of the strengthening mechanisms in nanocarbon-reinforced and HPT-deformed MMCs have shown that the observed strength increase is mainly caused by decreasing the grain size (Hall-Petch theory). The reinforcements (CNTs or NDs), located at the grain boundaries and triple junctions act as obstacles for the grain boundary movement, which allows a stronger grain refinement through HPT-deformation than in pure metals. The process of grain refinement is similar as in pure metals. The HPT-deformation process causes the dislocations to coalesce

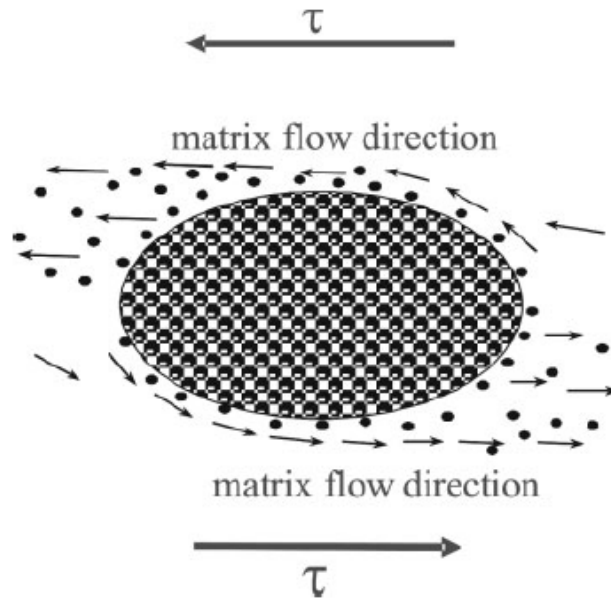


Figure 7.1.: Schematic illustration of the dissolution process of particle clusters during plastic deformation [71].

into sub-boundaries, which leads to the formation of sub-grains and subsequently a smaller grain size with increasing equivalent strain. Orowan strengthening, the typical hardening mechanism in nanodispersion strengthened alloys, was not observed in the MMCs, as the reinforcements are not located inside the grains to enable dislocation looping. Load transfer strengthening as well as strengthening through impurities and solid solution of carbon only have a small influence on the final strength.

Overall, it can be concluded that with the right combination of pre-deformation powder treatment, reinforcement content, as well as process temperature, HPT-deformation can be used to create nanocarbon-reinforced MMCs. An increased microhardness and tensile strength and also a reasonable ductility can be achieved through the optimization of the microstructure with ufg or nc metal grains and a homogeneous distribution of nanometer-sized reinforcement particles.

Although the microstructural and mechanical behaviour of nanocarbon-reinforced

7. Summary

MMCs was thoroughly studied in this work, there are some questions that remain unanswered and should be the subject of future investigations. One such question is, can the second phase distribution be further improved? Figures 3.6 and 5.11 show that the CNT and ND agglomerates are still much larger than their constituent particles and could possibly be further dissolved to achieve a better distribution through longer HPT-deformation and/or higher HPT-deformation temperatures. A further modified HPT-deformation process could also improve the microhardness evolution for the Ni/CNT MMCs. As can be seen in Figure 4.5, full microhardness saturation over the whole sample radius has not been reached for the samples HPT-deformed at lower temperatures and with the two-temperature deformation process. With higher HPT-deformation temperatures it would also be possible to investigate if additional texture components, caused by different deformation and restoration mechanisms, appear similar to HPT-deformed pure Ni.

Last of all a few comments in regards to the applications of nanocarbon-reinforced MMCs are in place. To make those MMCs viable for future applications, it is first necessary to increase the sample size. Although it is possible to perform HPT-deformation on sample sizes up to a diameter of 70 mm, it is unclear if a homogeneous second phase distribution can be achieved for such large samples, especially in regards to the high temperatures needed throughout the whole samples.

Future applications for Ni/CNT MMCs include structural and functional components where at the moment pure Ni or Ni alloys are used and a higher mechanical strength is useful. The higher thermal stability of Ni/CNT MMCs is also a desired advantage. Another promising field of application for Ni/CNT MMCs lies in tribology. While the high microhardness provides a good wear resistance, the CNT reinforcements can act additionally as solid lubricants.

The future use of Ag/ND MMCs includes the thermal management of electronic components and, like for the Ni/CNT MMCs, applications where a higher strength and wear resistance are needed. This includes the jewellery industry, where the reinforcement with NDs not only improves the mechanical properties of Ag and also Au, but also adds to the aesthetic and monetary value of the materials.

References

- [1] R. Z. Valiev, R. K. Islamgaliev, and I. V. Alexandrov, “Bulk nanostructured materials from severe plastic deformation,” *Prog. Mater. Sci.*, vol. 45, no. 2, 2000.
- [2] C. Suryanarayana, “Mechanical alloying and milling,” *Prog. Mater. Sci.*, vol. 46, no. 1–2, pp. 1–184, 2001.
- [3] T.W. Clyne, P.J. Withers, “An introduction to metal matrix composites,” Cambridge University Press, 1993
- [4] R. Pippan, S. Scheriau, A. Taylor, M. Hafok, A. Hohenwarter, and A. Bachmaier, “Saturation of Fragmentation During Severe Plastic Deformation,” *Annu. Rev. Mater. Res.*, vol. 40, no. 1, pp. 319–343, 2010.
- [5] A. Bachmaier and R. Pippan, “Generation of metallic nanocomposites by severe plastic deformation,” *Int. Mater. Rev.*, vol. 58, no. 1, pp. 41–62, 2013.
- [6] A. Hohenwarter, “Incremental high pressure torsion as a novel severe plastic deformation process: Processing features and application to copper,” *Mater. Sci. Eng. A*, vol. 626, pp. 80–85, 2015.
- [7] K. Edalati and Z. Horita, “A review on high-pressure torsion (HPT) from 1935 to 1988,” *Mater. Sci. Eng. A*, vol. 652, pp. 325–352, 2016.
- [8] T. G. Langdon, “Research on bulk nanostructured materials in Ufa: Twenty years of scientific achievements,” *Mater. Sci. Eng. A*, vol. 503, no. 1–2, pp. 6–9, 2009.
- [9] R. Wadsack, R. Pippan, and B. Schedler, “Structural refinement of chromium by severe plastic deformation,” *Fusion Eng. Des.*, vol. 66–68, pp. 265–269, 2003.
- [10] A. Vorhauer and R. Pippan, “On the homogeneity of deformation by high pressure torsion,” *Scr. Mater.*, vol. 51, no. 9, pp. 921–925, 2004.

References

- [11] T. Hebesberger, H. P. Stüwe, A. Vorhauer, F. Wetscher, and R. Pippan, “Structure of Cu deformed by high pressure torsion,” *Acta Mater.*, vol. 53, no. 2, pp. 393–402, 2005.
- [12] A. P. Zhilyaev and T. G. Langdon, “Using high-pressure torsion for metal processing: Fundamentals and applications,” *Prog. Mater. Sci.*, vol. 53, no. 6, pp. 893–979, 2008.
- [13] O. A. Shenderova, V. V. Zhirnov, and D. W. Brenner, “Carbon nanostructures,” *Crit. Rev. Solid State Mater. Sci.*, vol. 27, no. 3–4, pp. 227–356, 2002.
- [14] G. D. Ado Jorio and M. S. Dresselhaus, Carbon nanotubes: “Advanced topics in the synthesis, structure, properties and applications,” *Top. Appl. Phys.*, vol. 11, no. 3. 2008.
- [15] S. R. Bakshi, D. Lahiri, and A. Agarwal, “Carbon nanotube reinforced metal matrix composites - a review,” *Int. Mater. Rev.*, vol. 55, no. 1, pp. 41–64, 2010.
- [16] A. V. Radhamani, H. C. Lau, and S. Ramakrishna, “CNT-reinforced metal and steel nanocomposites: A comprehensive assessment of progress and future directions,” *Compos. Part A Appl. Sci. Manuf.*, vol. 114, no. August, pp. 170–187, 2018.
- [17] E. T. Thostenson, Z. Ren, and T.-W. Chou, “Advances in the science and technology of carbon nanotubes and their composites: a review,” *Compos. Sci. Technol.*, vol. 61, no. 13, pp. 1899–1912, 2001.
- [18] K. S. Munir, P. Kingshott, and C. Wen, “Carbon Nanotube Reinforced Titanium Metal Matrix Composites Prepared by Powder Metallurgy—A Review,” *Crit. Rev. Solid State Mater. Sci.*, vol. 40, no. 1, pp. 38–55, 2015.
- [19] A. Miranda, N. Barekar, B. J. McKay, and B. Field, “MWCNTs and their use in Al-MMCs for ultra-high thermal conductivity applications : A review,” *J. Alloys Compd.*, vol. 774, pp. 820–840, 2019.
- [20] A. Dorri Moghadam, E. Omrani, P. L. Menezes, and P. K. Rohatgi, “Mechanical and tribological properties of self-lubricating metal matrix nanocomposites reinforced by carbon nanotubes (CNTs) and graphene - A review,” *Compos. Part B Eng.*, vol. 77, pp. 402–420, 2015.
- [21] W. Zhai, N. Srikanth, L. B. Kong, and K. Zhou, “Carbon nanomaterials in tribology,” *Carbon N. Y.*, vol. 119, pp. 150–171, 2017.

- [22] S. Imani Yengejeh, S. A. Kazemi, and A. Öchsner, “Carbon nanotubes as reinforcement in composites: A review of the analytical, numerical and experimental approaches,” *Comput. Mater. Sci.*, vol. 136, pp. 85–101, 2017.
- [23] S. Suarez, F. Lasserre, F. Soldera, R. Pippan, and F. Mücklich, “Microstructural thermal stability of CNT-reinforced composites processed by severe plastic deformation,” *Mater. Sci. Eng. A*, vol. 626, pp. 122–127, 2015.
- [24] K. Aristizabal, A. Katzensteiner, F. Mücklich, S. Suárez, and A. Bachmaier, “Evolution of the microstructure in carbon nanotube reinforced Nickel matrix composites processed by high-pressure torsion,” *IOP Conf. Ser. Mater. Sci. Eng.*, vol. 258, p. 012008, 2017.
- [25] K. Aristizabal, A. Katzensteiner, A. Bachmaier, F. Mücklich, and S. Suarez, “Study of the structural defects on carbon nanotubes in metal matrix composites processed by severe plastic deformation,” *Carbon N. Y.*, vol. 125, pp. 156–161, 2017.
- [26] K. Aristizabal, A. Katzensteiner, A. Bachmaier, F. Mücklich, and S. Suárez, “On the reinforcement homogenization in CNT/metal matrix composites during severe plastic deformation,” *Mater. Charact.*, vol. 136, no. January, pp. 375–381, 2018.
- [27] K. Aristizabal, A. Katzensteiner, M. Leoni, F. Mücklich, and S. Suárez, “Evolution of the lattice defects and crystalline domain size in carbon nanotube metal matrix composites processed by severe plastic deformation,” *Mater. Charact.*, vol. 154, no. April, pp. 344–352, Aug. 2019.
- [28] K. Aristizabal, A. Tayrac, A. Katzensteiner, A. Bachmaier, and S. Suarez, “Friction and Tribo-Chemical Behavior of SPD-Processed CNT-Reinforced Composites,” *Lubricants*, vol. 7, no. 75, pp. 1–10, 2019.
- [29] H. Li et al., “Strong and ductile nanostructured Cu-carbon nanotube composite,” *Appl. Phys. Lett.*, vol. 95, no. 7, pp. 19–22, 2009.
- [30] P. Jenei, E. Y. Yoon, J. Gubicza, H. S. Kim, J. L. Lábár, and T. Ungár, “Microstructure and hardness of copper-carbon nanotube composites consolidated by High Pressure Torsion,” *Mater. Sci. Eng. A*, vol. 528, no. 13–14, pp. 4690–4695, 2011.
- [31] P. Jenei, J. Gubicza, E. Y. Yoon, H. S. Kim, and J. L. Lábár, “High temperature thermal stability of pure copper and copper-carbon nanotube composites consolidated by High Pressure Torsion,” *Compos. Part A Appl. Sci. Manuf.*, vol. 51, pp. 71–79, 2013.

References

- [32] E. Y. Yoon, D. J. Lee, B. Park, M. R. Akbarpour, M. Farvizi, and H. S. Kim, “Grain refinement and tensile strength of carbon nanotube-reinforced Cu matrix nanocomposites processed by high-pressure torsion,” *Met. Mater. Int.*, vol. 19, no. 5, pp. 927–932, 2013.
- [33] M. R. Akbarpour, M. Farvizi, D. J. Lee, H. Rezaei, and H. S. Kim, “Effect of high-pressure torsion on the microstructure and strengthening mechanisms of hot-consolidated Cu-CNT nanocomposite,” *Mater. Sci. Eng. A*, vol. 638, pp. 289–295, 2015.
- [34] T. Tokunaga, K. Kaneko, and Z. Horita, “Production of aluminum-matrix carbon nanotube composite using high pressure torsion,” *Mater. Sci. Eng. A*, vol. 490, pp. 300–304, 2008.
- [35] S. H. Joo, S. C. Yoon, C. S. Lee, D. H. Nam, S. H. Hong, and H. S. Kim, “Microstructure and tensile behavior of Al and Al-matrix carbon nanotube composites processed by high pressure torsion of the powders,” *J. Mater. Sci.*, vol. 45, no. 17, pp. 4652–4658, 2010.
- [36] D. D. Phuong, P. Van Trinh, N. Van An, N. Van Luan, P. Ngoc, and A. A. Nazarov, “Effects of carbon nanotube content and annealing temperature on the hardness of CNT reinforced aluminum nanocomposites processed by the high pressure torsion technique,” *J. Alloys Compd.*, vol. 613, pp. 68–73, 2014.
- [37] H. Asgharzadeh and H. S. Kim, “Microstructure and Mechanical Properties of Al-3 Vol% CNT Nanocomposites Processed by High-Pressure Torsion,” *Arch. Metall. Mater.*, vol. 62, no. 2, pp. 1109–1112, 2017.
- [38] F. X. Li et al., “Microstructure and strength of nano- / ultrafine-grained carbon nanotube-reinforced titanium composites processed by high-pressure torsion,” *Mater. Sci. Eng. A*, vol. 722, no. March, pp. 122–128, 2018.
- [39] I. Y. Archakov et al., “Microstructure and mechanical characteristics of nanostructured nickel-graphene composites processed by high pressure torsion,” *Rev. Adv. Mater. Sci.*, vol. 50, no. 1–2, pp. 13–23, 2017.
- [40] Y. Huang et al., “The fabrication of graphene-reinforced Al-based nanocomposites using high-pressure torsion,” *Acta Mater.*, vol. 164, pp. 499–511, 2019.
- [41] N. Khobragade, K. Sikdar, B. Kumar, S. Bera, and D. Roy, “Mechanical and electrical properties of copper-graphene nanocomposite fabricated by high pressure torsion,” *J. Alloys Compd.*, vol. 776, pp. 123–132, 2019.

- [42] T. Tokunaga, K. Kaneko, K. Sato, and Z. Horita, “Microstructure and mechanical properties of aluminum – fullerene composite fabricated by high pressure torsion,” *Scr. Mater.*, vol. 58, pp. 735–738, 2008.
- [43] H. Asgharzadeh and S. Joo, “Al/C60 Nanocomposites Fabricated by High-Pressure Torsion,” *Metall. Mater. Trans. A*, vol. 46A, pp. 1838–1842, 2015.
- [44] A. Roh, H. Y. Um, D. Kim, S. Nam, H. S. Kim, and H. Choi, “Influence of high-pressure torsion and hot rolling on the microstructure and mechanical properties of aluminum – fullerene composites,” *J. Mater. Sci.*, vol. 52, no. 20, pp. 11988–12000, 2017.
- [45] G. B. Rathmayr and R. Pippan, “Influence of impurities and deformation temperature on the saturation microstructure and ductility of HPT-deformed nickel,” *Acta Mater.*, vol. 59, no. 19, pp. 7228–7240, 2011.
- [46] C. Borchers et al., “Nanocrystalline steel obtained by mechanical alloying of iron and graphite subsequently compacted by high-pressure torsion,” *Acta Mater.*, vol. 97, pp. 207–215, 2015.
- [47] H. Zare, M. Jahedi, M. R. Toroghinejad, M. Meratian, and M. Knezevic, “Compressive, shear, and fracture behavior of CNT reinforced Al matrix composites manufactured by severe plastic deformation,” *Mater. Des.*, vol. 106, pp. 112–119, 2016.
- [48] H. Zare, M. Jahedi, M. R. Toroghinejad, M. Meratian, and M. Knezevic, “Microstructure and mechanical properties of carbon nanotubes reinforced aluminum matrix composites synthesized via equal-channel angular pressing,” *Mater. Sci. Eng. A*, vol. 670, pp. 205–216, 2016.
- [49] P. Quang, Y. G. Jeong, S. C. Yoon, S. H. Hong, and H. S. Kim, “Consolidation of 1 vol.% carbon nanotube reinforced metal matrix nanocomposites via equal channel angular pressing,” *J. Mater. Process. Technol.*, vol. 188, pp. 318–320, 2007.
- [50] S. J. Yoo, S. H. Han, and W. J. Kim, “A combination of ball milling and high-ratio differential speed rolling for synthesizing carbon nanotube / copper composites,” *Carbon N. Y.*, vol. 61, pp. 487–500, 2013.
- [51] L. Xiong, J. Shuai, K. Liu, Z. Hou, L. Zhu, and W. Li, “Enhanced mechanical and electrical properties of super-aligned carbon nanotubes reinforced copper by severe plastic deformation,” *Compos. Part B*, vol. 160, no. October 2018, pp. 315–320, 2019.

References

- [52] S. J. Yoo, S. H. Han, and W. J. Kim, “Magnesium matrix composites fabricated by using accumulative roll bonding of magnesium sheets coated with carbon-nanotube- containing aluminum powders,” *Scr. Mater.*, vol. 67, no. 2, pp. 129–132, 2012.
- [53] G. Ferreira et al., “Characterization of hydrogen storage properties of Mg-Fe-CNT composites prepared by ball milling , hot-extrusion and severe plastic deformation methods,” *Int. J. Hydrogen Energy*, vol. 41, no. 48, pp. 23092–23098, 2016.
- [54] F. Ferreira, I. Ferreira, E. Camacho, F. Lopes, A. C. Marques, and A. Velhinho, “Graphene oxide-reinforced aluminium-matrix nanostructured composites fabricated by accumulative roll bonding,” *Compos. Part B Eng.*, vol. 164, no. October 2018, pp. 265–271, 2019.
- [55] V. Viswanathan, T. Laha, K. Balani, A. Agarwal, and S. Seal, “Challenges and advances in nanocomposite processing techniques,” *Mater. Sci. Eng. R Reports*, vol. 54, no. 5–6, pp. 121–285, 2006.
- [56] M. S. Dresselhaus and G. Dresselhaus, “Nanotechnology in Carbon Materials I,” *Acta Metall.*, vol. 9, no. 97, pp. 33–42, 1997.
- [57] Z. Li, L. Wang, Y. Li, Y. Feng, and W. Feng, “Carbon-based functional nanomaterials: Preparation, properties and applications,” *Compos. Sci. Technol.*, vol. 179, no. April, pp. 10–40, 2019.
- [58] S. Iijima, “Helical microtubules of graphitic carbon,” *Nature*, vol. 354, no. November, pp. 56–58, 1991.
- [59] M. S. Dresselhaus, G. Dresselhaus, and R. Saito, “Physics of carbon nanotubes,” *Carbon N. Y.*, vol. 33, no. 7, pp. 883–891, 1995.
- [60] O. A. Shenderova, “Production of Nanodiamond Particles,” *Comp. Hard Mat.*, vol. 3. pp. 143-171, 2014.
- [61] V.A. Popov, “Metal Matrix Composites with Non-Agglomerated Nanodiamond Reinforcing Particles,” *Nanocomp.*, pp. 369-401, 2013.
- [62] L. Reinert, M. Zeiger, S. Suárez, V. Presser, and F. Mücklich, “Dispersion analysis of carbon nanotubes, carbon onions, and nanodiamonds for their application as reinforcement phase in nickel metal matrix composites,” *RSC Adv.*, vol. 5, no. 115, pp. 95149–95159, 2015.

- [63] P. W. Trimby, “Orientation mapping of nanostructured materials using transmission Kikuchi diffraction in the scanning electron microscope,” *Ultramicroscopy*, vol. 120, pp. 16–24, 2012.
- [64] <https://www.bruker.com/products/x-ray-diffraction-and-elemental-analysis/eds-wds-ebbsd-sem-micro-xrf-and-sem-micro-ct/esprit-2.html> (accessed: March 25th, 2019)
- [65] <https://www.edax.com/products/ebbsd/oim-analysis> (accessed: March 25th, 2019)
- [66] H. P. Stüwe, “Equivalent strains in severe plastic deformation,” *Adv. Eng. Mater.*, vol. 5, no. 5, pp. 291–295, 2003.
- [67] Y. Cao, S. Ni, X. Liao, M. Song, and Y. Zhu, “Structural evolutions of metallic materials processed by severe plastic deformation,” *Mater. Sci. Eng. R Reports*, vol. 133, no. May, pp. 1–59, 2018.
- [68] S. Suarez, F. Lasserre, and F. Mücklich, “Mechanical properties of MWNT/Ni bulk composites: Influence of the microstructural refinement on the hardness,” *Mater. Sci. Eng. A*, vol. 587, pp. 381–386, 2013.
- [69] C. A. Schneider, W. S. Rasband, and K. W. Eliceiri, “NIH Image to ImageJ: 25 years of Image Analysis,” *Nat. Methods*, vol. 9, no. 7, pp. 671–675, 2012.
- [70] A. C. Ferrari and J. Robertson, “Interpretation of Raman spectra of disordered and amorphous carbon,” *Phys. Rev. B*, vol. 61, no. 20, pp. 14095–14107, 2000.
- [71] R. Pippan, F. Wetscher, M. Hafok, A. Vorhauer, and I. Sabirov, “The limits of refinement by severe plastic deformation,” *Adv. Eng. Mater.*, vol. 8, no. 11, pp. 1046–1056, 2006.
- [72] K. W. Neale, L. S. Tóth, and J. J. Jonas, “LARGE STRAIN SHEAR AND TORSION OF RATE-SENSITIVE FCC POLYCRYSTALS,” *Int. J. Plast.*, vol. 6, pp. 45–61, 1990.
- [73] M. Hafok and R. Pippan, “High-pressure torsion applied to nickel single crystals,” *Philos. Mag.*, vol. 88, no. 12, pp. 1857–1877, 2008.
- [74] P. Ghosh, O. Renk, and R. Pippan, “Microtexture analysis of restoration mechanisms during high pressure torsion of pure nickel,” *Mater. Sci. Eng. A*, vol. 684, no. December 2016, pp. 101–109, 2017.

References

- [75] F. Mokdad, B. L. Xiao, D. R. Ni, D. L. Chen, Z. Y. Liu, and Z. Y. Ma, “Deformation and strengthening mechanisms of a carbon nanotube reinforced aluminum composite,” *Carbon N. Y.*, vol. 104, pp. 64–77, 2016.
- [76] G. Q. Han et al., “The influence of CNTs on the microstructure and ductility of CNT/Mg composites,” *Mater. Lett.*, vol. 181, pp. 300–304, 2016.
- [77] G. B. Rathmayr, A. Bachmaier, and R. Pippan, “Development of a New Testing Procedure for Performing Tensile Tests on Specimens with Sub-Millimetre Dimensions,” *J. Test. Eval.*, vol. 41, no. 4, p. 20120175, 2013.
- [78] <http://www.microsample.eu/specimen-preparation/> (accessed: June 12, 2018).
- [79] X. H. An et al., “The influence of stacking fault energy on the mechanical properties of nanostructured Cu and Cu-Al alloys processed by high-pressure torsion,” *Philos. Mag.*, vol. 91, no. 25, pp. 3307–3326, 2011.
- [80] A. Bachmaier, A. Hohenwarter, and R. Pippan, “New procedure to generate stable nanocrystallites by severe plastic deformation,” *Scr. Mater.*, vol. 61, no. 11, pp. 1016–1019, 2009.
- [81] S. Suárez, A. Rosenkranz, C. Gachot, and F. Mücklich, “Enhanced tribological properties of MWCNT/Ni bulk composites - Influence of processing on friction and wear behaviour,” *Carbon N. Y.*, vol. 66, pp. 164–171, 2014.
- [82] P. Rossi, S. Suarez, F. Soldera, and F. Mücklich, “Quantitative Assessment of the Reinforcement Distribution Homogeneity in CNT/Metal Composites,” *Adv. Eng. Mater.*, vol. 17, no. 7, pp. 1017–1021, 2015.
- [83] D. Tabor, “Hardness of Metals,” Clarendon Press, Oxford, 1951.
- [84] P. Zhang, S. X. Li, and Z. F. Zhang, “General relationship between strength and hardness,” *Mater. Sci. Eng. A*, vol. 529, no. 1, pp. 62–73, 2011.
- [85] G. B. Rathmayr and R. Pippan, “Extrinsic and intrinsic fracture behavior of high pressure torsion deformed nickel,” *Scr. Mater.*, vol. 66, no. 8, pp. 507–510, 2012.
- [86] A. Pineau, A. A. Benzerga, and T. Pardoen, “Failure of metals I: Brittle and ductile fracture,” *Acta Mater.*, vol. 107, pp. 424–483, 2016.
- [87] V. V. Ganesh and N. Chawla, “Effect of reinforcement-particle-orientation anisotropy on the tensile and fatigue behavior of metal-matrix composites,” *Metall. Mater. Trans. A*, vol. 35, no. January, pp. 53–61, 2004.

- [88] G. B. Rathmayr, A. Hohenwarter, and R. Pippan, “Influence of grain shape and orientation on the mechanical properties of high pressure torsion deformed nickel,” *Mater. Sci. Eng. A*, vol. 560, pp. 224–231, 2013.
- [89] S. V. Kidalov and F. M. Shakhov, “Thermal conductivity of diamond composites,” *Materials (Basel)*., vol. 2, no. 4, pp. 2467–2495, 2009.
- [90] L. Wang, Y. Gao, Q. Xue, H. Liu, and T. Xu, “Effects of nano-diamond particles on the structure and tribological property of Ni-matrix nanocomposite coatings,” *Mater. Sci. Eng. A*, vol. 390, no. 1–2, pp. 313–318, 2005.
- [91] B. Q. Han, J. Ye, F. Tang, J. Schoenung, and E. J. Lavernia, “Processing and behavior of nanostructured metallic alloys and composites by cryomilling,” *J. Mater. Sci.*, vol. 42, no. 5, pp. 1660–1672, 2007.
- [92] F. A. da Costa, A. G. P. da Silva, F. A. Filho, U. U. Gomes, and F. A. Vieira, “Synthesis of a nanocrystalline composite W-25 wt.% Ag powder by high energy milling,” *Powder Technol.*, vol. 188, no. 1, pp. 30–33, 2008.
- [93] J. H. Ahn and S. Oh, “High-energy ball-milling for the synthesis of Ag-B superconducting materials,” *J. Alloys Compd.*, vol. 504, no. SUPPL. 1, pp. 292–294, 2010.
- [94] X. Yan and G. Xu, “Effect of surface modification of Cu with Ag by ball-milling on the corrosion resistance of low infrared emissivity coating,” *Mater. Sci. Eng. B Solid-State Mater. Adv. Technol.*, vol. 166, no. 2, pp. 152–157, 2010.
- [95] G. R. Khayati and K. Janghorban, “The nanostructure evolution of Ag powder synthesized by high energy ball milling,” *Adv. Powder Technol.*, vol. 23, no. 3, pp. 393–397, 2012.
- [96] Z. Hegedüs, S. R. Meka, and E. J. Mittemeijer, “In situ consolidation of ball milled metals,” *J. Alloys Compd.*, vol. 695, no. December, pp. 721–725, 2017.
- [97] D. Oleszak and P. H. Shingu, “Nanocrystalline metals prepared by low energy ball milling,” *J. Appl. Phys.*, vol. 79, no. 6, pp. 2975–2980, 1996.
- [98] H. Kaftelen and M. L. Öveçoğlu, “Microstructural characterization and wear properties of ultra-dispersed nanodiamond (UDD) reinforced Al matrix composites fabricated by ball-milling and sintering,” *J. Compos. Mater.*, vol. 46, no. 13, pp. 1521–1534, 2012.
- [99] D. J. Woo et al., “Synthesis of nanodiamond-reinforced aluminum metal composite powders and coatings using high-energy ball milling and cold spray,” *Carbon N. Y.*, vol. 63, no. 1, pp. 404–415, 2013.

References

- [100] V. Livramento, J. B. Correia, N. Shohoji, and E. Osawa, “Nanodiamond as an effective reinforcing component for nano-copper,” *Diam. Relat. Mater.*, vol. 16, no. 2, pp. 202–204, 2007.
- [101] V. A. Popov et al., “New mechanical-alloying-based technological scheme for producing electrochemical composite coatings reinforced with non-agglomerated nanodiamond particles,” *J. Alloys Compd.*, vol. 615, no. S1, pp. S433–S436, 2015.
- [102] K. Hanada et al., “Further studies on copper nanocomposite with dispersed single-digit-nanodiamond particles,” *Diam. Relat. Mater.*, vol. 16, no. 12, pp. 2054–2057, 2007.
- [103] S. L. Urtiga Filho, R. Rodriguez, J. C. Earthman, and E. J. Lavernia, “Synthesis of diamond reinforced Al-Mg nanocrystalline composite powder using ball milling,” *Mater. Sci. Forum*, vol. 416–418, no. 1, pp. 213–218, 2003.
- [104] B. Chen et al., “Length effect of carbon nanotubes on the strengthening mechanisms in metal matrix composites,” *Acta Mater.*, vol. 140, pp. 317–325, 2017.
- [105] G. Angella, B. Esfandiar Jahromi, and M. Vedani, “A comparison between equal channel angular pressing and asymmetric rolling of silver in the severe plastic deformation regime,” *Mater. Sci. Eng. A*, vol. 559, pp. 742–750, 2013.
- [106] J. Gubicza, N. Q. Chinh, J. L. Lábár, Z. Hegedus, and T. G. Langdon, “Principles of self-annealing in silver processed by equal-channel angular pressing: The significance of a very low stacking fault energy,” *Mater. Sci. Eng. A*, vol. 527, no. 3, pp. 752–760, 2010.
- [107] H. W. Hsueh, F. Y. Hung, T. S. Lui, and L. H. Chen, “Effect of the direct current on microstructure, tensile property and bonding strength of pure silver wires,” *Microelectron. Reliab.*, vol. 53, no. 8, pp. 1159–1163, 2013.
- [108] J. Wu and C. C. Lee, “The growth and tensile deformation behavior of the silver solid solution phase with zinc,” *Mater. Sci. Eng. A*, vol. 668, pp. 160–165, 2016.
- [109] J. He, N. Zhao, C. Shi, X. Du, J. Li, and P. Nash, “Reinforcing copper matrix composites through molecular-level mixing of functionalized nanodiamond by co-deposition route,” *Mater. Sci. Eng. A*, vol. 490, no. 1–2, pp. 293–299, 2008.
- [110] I. Petrov et al., “Nickel galvanic coatings co-deposited with fractions of detonation nanodiamond,” *Diam. Relat. Mater.*, vol. 15, no. 11-12 SPEC. ISS., pp. 2035–2038, 2006.

- [111] K. Iakoubovskii, K. Mitsuishi, and K. Furuya, “High-resolution electron microscopy of detonation nanodiamond,” *Nanotechnology*, vol. 19, no. 15, 2008.
- [112] E. O. Hall, “The Deformation and Ageing of Mild Steel: III Discussion of Results,” *Proc. Phys. Soc. Sect. B*, vol. 64, p. 747, 1951.
- [113] Z. C. Cordero, B. E. Knight, and C. A. Schuh, “Six decades of the Hall–Petch effect – a survey of grain-size strengthening studies on pure metals,” *Int. Mater. Rev.*, vol. 61, no. 8, pp. 495–512, 2016.
- [114] K. T. Kim, J. Eckert, S. B. Menzel, T. Gemming, and S. H. Hong, “Grain refinement assisted strengthening of carbon nanotube reinforced copper matrix nanocomposites,” *Appl. Phys. Lett.*, vol. 92, no. 12, pp. 3–5, 2008.
- [115] H. J. Choi, J. H. Shin, and D. H. Bae, “Grain size effect on the strengthening behavior of aluminum-based composites containing multi-walled carbon nanotubes,” *Compos. Sci. Technol.*, vol. 71, no. 15, pp. 1699–1705, 2011.
- [116] J. Gubicza, N. Q. Chinh, J. L. Lábár, Z. Hegedus, C. Xu, and T. G. Langdon, “Microstructure and yield strength of severely deformed silver,” *Scr. Mater.*, vol. 58, no. 9, pp. 775–778, 2008.
- [117] Ashby and M.F., “The deformation of plastically non-homogeneous materials,” *Philos. Mag.*, vol. 21, no. 170, pp. 37–41, 1969.
- [118] T. Gladman, “Precipitation hardening in metals,” *Mater. Sci. Technol.*, vol. 15, no. 1, pp. 30–36, 2004.
- [119] U. Maitra, K. E. Prasad, U. Ramamurty, and C. N. R. Rao, “Mechanical properties of nanodiamond-reinforced polymer-matrix composites,” *Solid State Commun.*, vol. 149, no. 39–40, pp. 1693–1697, 2009.
- [120] V. C. Nardone and K. M. Prewo, “On the strength of discontinuous silicon carbide reinforced aluminum composites,” *Scr. Metall.*, vol. 20, no. 1, pp. 43–48, 1986.
- [121] R. Casati and M. Vedani, “Metal Matrix Composites Reinforced by Nano-Particles—A Review,” *Metals (Basel)*, vol. 4, no. 1, pp. 65–83, 2014.
- [122] W. Callister and D. Rethwisch, *Materials science and engineering: an introduction*, vol. 94. 2007.
- [123] S. Suarez, F. Lasserre, O. Prat, and F. Mücklich, “Processing and interfacial reaction evaluation in MWCNT/Ni composites,” *Phys. Status Solidi Appl. Mater. Sci.*, vol. 211, no. 7, pp. 1555–1561, 2014.

References

- [124] M. Singleton and P. Nash, “The C-Ni (Carbon-Nickel) system,” *Bull. Alloy Phase Diagrams*, vol. 10, no. 2, pp. 121–126, 1989.
- [125] I. Sabirov, M. Y. Murashkin, and R. Z. Valiev, “Nanostructured aluminium alloys produced by severe plastic deformation: New horizons in development,” *Mater. Sci. Eng. A*, vol. 560, pp. 1–24, 2013.
- [126] R. B. McLellan, “The Solubility of Carbon in Solid Gold, Copper, and Silver,” *Scr. Metall.*, vol. 3, pp. 389–392, 1969.

Appendix

First-authored publications

Publication A: Temperature dependent structural evolution in nickel/carbon nanotube composites processed by high-pressure torsion

Publication B: Influence of Processing Parameters on the Mechanical Properties of HPT-Deformed Nickel/Carbon Nanotube Composites

A. Temperature dependent structural evolution in nickel/carbon nanotube composites processed by high-pressure torsion

Authors

Andreas Katzensteiner¹, Katherine Aristizabal², Sebastian Suarez², Reinhard Pippan¹ and Andrea Bachmaier¹

¹ Erich Schmid Institute, Jahnstr. 12, A-8700 Leoben, Austria

² Department of Materials Science, Campus D3.3, D-66123 Saarbrücken, Germany

Journal

IOP Conference Series: Materials Science and Engineering **194**; 2017; 012019

Abstract

Nickel/Carbon nanotube (CNT) composites with varying amounts of CNTs were processed at different temperatures by high-pressure torsion (HPT) with the aim to optimize the process parameters to obtain a homogenous dispersion of CNTs in the metallic matrix. As the CNT distribution has an enormous influence on the composite properties, the structural evolution with increasing strain and the final microstructure of the composites are investigated by scanning and transmission electron microscopy. Microhardness measurements were additionally performed. Microhardness increases up to 800 Vickers (HV) and the mean grain size decreases to an equivalent radius smaller than 40 nm for HPT at room temperature (RT), while the CNTs form rather large agglomerates. HPT-deformation at 200°C shows no significant change in hardness, grain size and CNT agglomerate size. For HPT-deformation at 300°C and 400°C grain sizes increase to 60 nm respectively 90 nm, microhardness decreases to 500 HV respectively 400 HV and the size of the CNT agglomerates decreases from more than 5 times the grain size at RT to smaller than the grain size. It could be shown that the optimal HPT processing route to improve the CNT distribution is a combination of deformation at 400°C with subsequent deformation at RT.

A.1. Introduction

Nanocrystalline (NC) and ultrafine-grained (UFG) materials have been shown to surpass coarse grained materials both in mechanical and in functional utility [1]. During the last couple of decades, severe plastic deformation (SPD) has been used to obtain dense UFG or even NC bulk materials in reasonable volumes [2].

In the majority of the studies SPD processing by high-pressure torsion (HPT) deformation of metal matrix composites (MMCs) showed improved mechanical properties compared to the deformation of pure metals, due to combining matrix and reinforcement properties [3, 4]. These properties are controlled by the size of the reinforcement as well as by its distribution within the matrix [5].

In this study, MMCs with nickel as the metal phase and carbon nanotubes (CNTs) as reinforcement are deformed by HPT. CNTs are well suited for use as reinforcement phase because of their high thermal conductivity, high specific strength, low weight and large aspect ratio [6]. Preinvestigations of SPD deformed Ni and Cu/CNT composites with 1 and 3wt% CNTs and 3 to 4 vol% CNTs have been already performed [7–9]. The present study investigates Ni/CNT MMCs with a greater variety of CNT weight percentages and HPT-deformation is additionally conducted at different temperatures to investigate the influence of temperature on the structural evolution. Since CNTs are known to form agglomerates in a metal matrix due to Van der Waals forces [10], a strong emphasis in this study is further laid on obtaining a uniform distribution of small CNT agglomerates. Hence, samples are deformed for different numbers of revolutions as well.

A.2. Experimental

The initial Ni/CNT MMC material was produced as described in [11]. The samples in the as-fabricated condition had a diameter of 8 mm, a thickness of about 1 mm and contained CNT weight percentages of 0.1, 0.25, 0.5, 1, 2 and 3. These samples were HPT-deformed with 0.2 rpm at room temperature (RT) for up to 30 revolutions as described in [12]. Samples were additionally deformed for 30 revolutions at 200°C, 300°C and 400°C with 0.6 rpm, resulting in an equivalent strain of more than 700 at a radius $r = 3$ mm [13].

Microhardness was measured every 0.25 mm along the radii of the HPT discs (mean value of three indents at each measurement point). The hardness measurements were carried out with a BUEHLER Micromet 5100 using a load of 300 g ($HV_{0.3}$).

Microstructures were characterized in a scanning electron microscope (SEM) type LEO 1525 using back scattered electrons (BSE). Images were taken along the radii of the samples every 0.5 mm to determine the dependence of the microstructural evolution on the equivalent strain.

A. Temperature dependent structural evolution in nickel/carbon nanotube composites

Additionally, HPT-deformed samples with 0.1wt% and 1wt% CNTs were prepared for transmission electron microscopy (TEM) investigations (Phillips CM12). HPT-deformation parameters were the following: 30 revolutions at 200°C (0.1wt%); 30 revolutions at RT (1wt%); 30 revolutions at 400°C with additional 5 revolutions at RT (1wt%). TEM images were recorded in radial direction for the samples with 1wt% CNTs and in axial direction for the 0.1wt% sample. All TEM samples were obtained at $r = 2\text{mm}$.

A.3. Results and discussion

With increasing equivalent strain the microhardness increases until it reaches a saturation at high strains for all investigated Ni/CNT MMCs (except the sample containing 3wt% CNTs). This is exemplarily shown in Figure A.1 a for the Ni MMC sample with 1wt% CNTs, which reaches a saturation hardness of 753 HV after 30 revolutions. Independent of the CNT weight percentage, all HPT-deformed samples show saturation hardness values above 720 HV after HPT-deformation at RT, as can be seen in Table A.1. The saturation onset for all samples is at a radius of about 3 mm after 30 revolutions, which corresponds to an equivalent strain of about 250 for the Ni/CNT MMC sample containing 1wt% CNTs (Figure A.1 a) and up to an equivalent strain of 400 for other compositions. In pure metals and single phase alloys the saturation regime is reached at a much lower strain [14, 15]. Similar high strains to reach saturation in hardness were needed for HPT-consolidated samples of pure Ni powder [16]. In the Ni/CNT MMCs an additional effect due to the presence of the CNTs has also to be considered. For the sample containing 3wt% CNTs, HPT-deformation at RT was limited to 5 revolutions due to the high hardness of the sample. Hence no steady state could be reached in this case.

To investigate the influence of the deformation temperature, HPT samples were deformed at 200°C, 300°C and 400°C. Figure A.1 b shows the hardness evolution with increasing strain at different deformation temperatures for Ni MMCs with 1wt% CNTs. The sample deformed at 200°C reaches almost the same saturation hardness as the sample deformed at RT, but higher strains are necessary to reach

saturation. At 300°C, the saturation hardness decreases to 510 HV. At 400°C, the saturation hardness decreases further (451 HV), but almost the same amount of strain is needed to reach saturation compared to the sample deformed at RT.

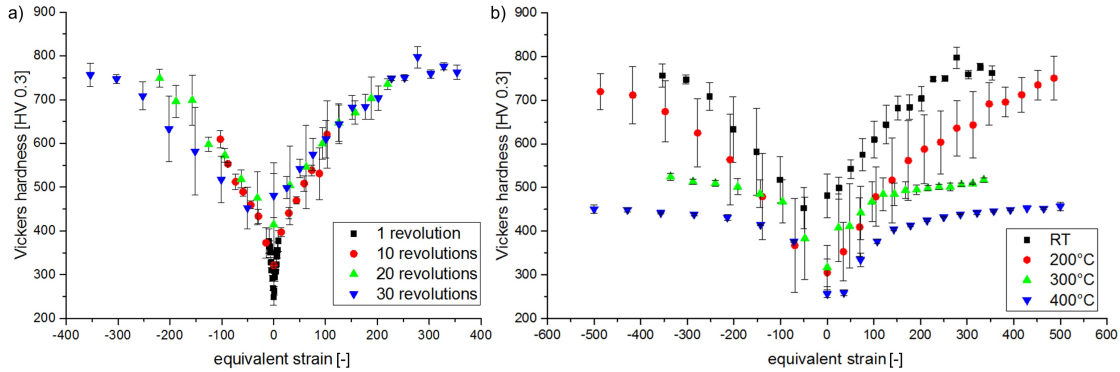


Figure A.1.: Vickers hardness as function of the applied equivalent strain of Ni MMCs with 1wt% CNTs after a) 1, 10, 20 and 30 revolutions at RT and after b) 30 revolutions at 200°C, 300°C and 400°C.

Table A.1 summarizes the saturation hardness values for all compositions and deformation temperatures. For all Ni/CNT MMCs the saturation hardness decreases with increasing deformation temperature. Only for the samples containing 0.5wt% CNTs, nearly the same hardness is reached at RT and 200°C. The Ni/CNT MMC samples with 0.25wt% and 0.5wt% samples have the most distinct decrease in hardness with increasing HPT-deformation temperature, the samples containing 2wt% CNTs, the smallest. As an example for the microstructural evolution of the Ni/CNT MMCs with increasing strain, Figure A.2 shows SEM images of the Ni MMCs with 1wt% CNTs deformed at RT at different amounts of applied strain. The size and the distribution of the CNT agglomerates does not significantly change with increasing number of revolutions, while the grain sizes of the Ni matrix decreases. Surprising is that Ni MMCs with different CNT weight percentages show a similar microstructural evolution of the Ni matrix and CNT distribution independent of the CNT content.

Figure A.3 displays the saturation microstructure of the Ni MMCs with 1wt%

A. *Temperature dependent structural evolution in nickel/carbon nanotube composites*

Table A.1.: Hardness values for all compositions and deformation temperatures (r=3 mm).

wt% CNTs	0.1	0.25	0.5	1	2	3
Sat. hardness RT	729 ± 33	724 ± 33	767 ± 22	753 ± 11	724 ± 24	-
Sat. hardness 200°C	604 ± 19	587 ± 37	762 ± 12	712 ± 49	702 ± 19	776 ± 27
Sat. hardness 300°C	501 ± 5	478 ± 6	520 ± 5	510 ± 6	497 ± 4	600 ± 1
Sat. hardness 400°C	401 ± 3	395 ± 3	438 ± 5	451 ± 3	458 ± 8	465 ± 3

CNTs at different deformation temperatures recorded at $r = 3$ mm. With increasing HPT-deformation temperature, the saturation grain size increases, while CNT agglomerates become smaller and more globular. After deformation at 300°C the CNTs still show some clustering, although these clusters consist of smaller agglomerates (Figure A.3 c). After deformation at 400°C a homogeneous distribution of small CNT agglomerates is achieved (Figure A.3 d). Ni MMC samples containing higher weight percentages of CNTs show a higher density of agglomerates, but there is no significant influence of CNT content on agglomerate size and shape.

Processing of the Ni MMC samples by HPT leads to strong grain refinement. SEM investigations show a decrease of the grain size with increasing number of revolutions and saturation values smaller than 40 nm for all compositions after 30 revolutions. However, a slight decrease of the grain size with increasing amount of CNTs is observed.

At a deformation temperature of 200°C, grain sizes increase slightly, but are below 100 nm. For deformation temperatures of 300°C and 400°C grain sizes increase further for nearly all compositions.

Since grains are hardly resolvable in SEM in the saturation region, the microstructure in the steady state of selected samples is additionally investigated in detail

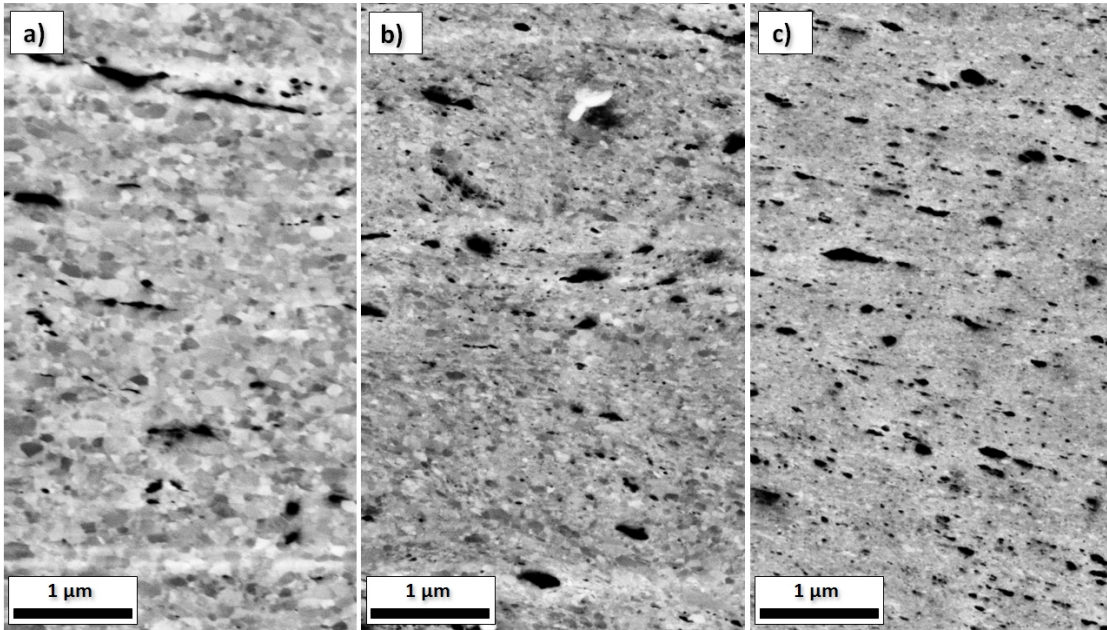


Figure A.2.: SEM images of Ni MMCs with 1wt% CNTs at $r = 3$ mm after a) 1, b) 10 and c) 20 revolutions deformed at RT.

by TEM.

Figure A.4 shows bright and dark field images with corresponding selected area diffraction (SAD) pattern of the Ni MMC sample with 1wt% CNTs deformed at RT, which was recorded at an equivalent strain of 450. Both images illustrate a nanocrystalline microstructure with grains having a size of about 100 nm and below, showing various defects displayed as contrast variations inside the grains. The grains are clearly elongated along the shear direction (as indicated in Figure A.4 a). In the SAD pattern shown in Figure A.4 a fcc Ni and traces of NiO Debye-Scherrer rings are observed. CNT agglomerates could not be discerned.

The generated microstructures of the Ni MMC sample with the lowest CNT content (0.1wt%) in the saturation regime are shown in bright and dark field images in Figure A.5. A comparable nanocrystalline structure with few larger but as well very small grains is revealed, where the different grains can hardly be distinguished from each other. The different shape of the grains (equiaxed in this case) is due

A. Temperature dependent structural evolution in nickel/carbon nanotube composites

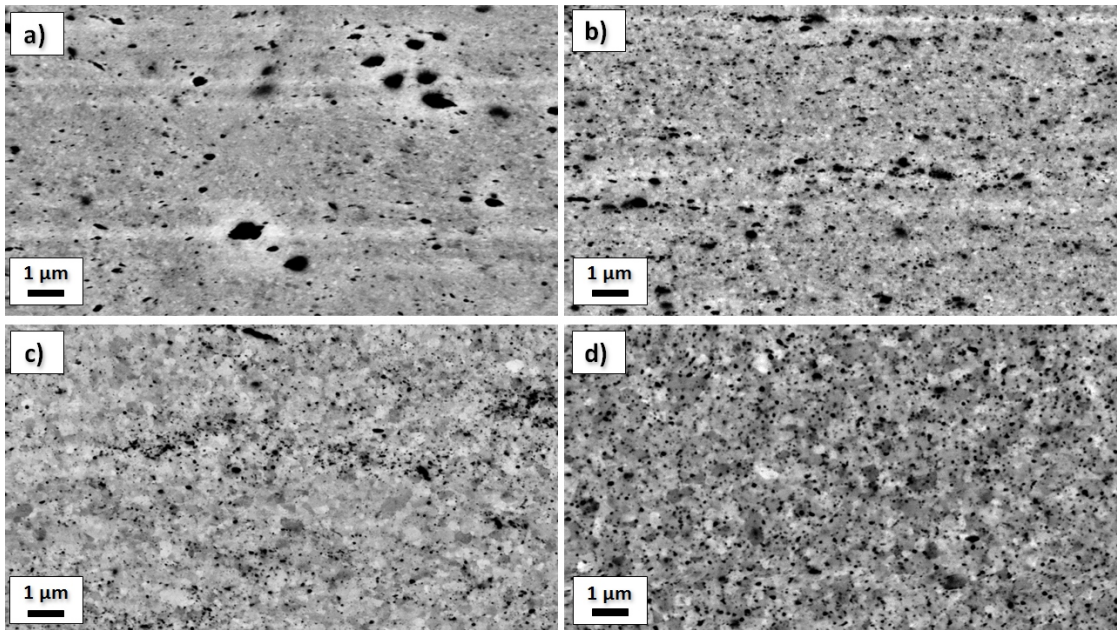


Figure A.3.: SEM images of Ni MMCs with 1wt% CNTs after 30 revolutions at $r = 3$ mm at a) RT, b) 200°C, c) 300°C and d) 400°C.

to the sample being observed in axial direction. In the SAD pattern only fcc Ni rings are visible.

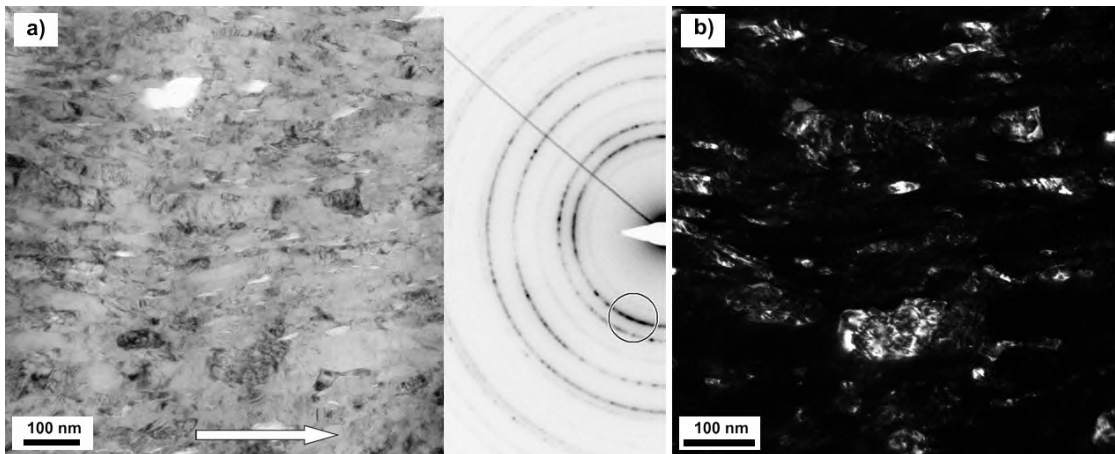


Figure A.4.: a) Bright field TEM image with corresponding SAD pattern and b) dark field TEM image of Ni MMCs with 1wt% CNTs after 30 revolutions at RT ($r = 2$ mm). The arrow marks the shear direction.

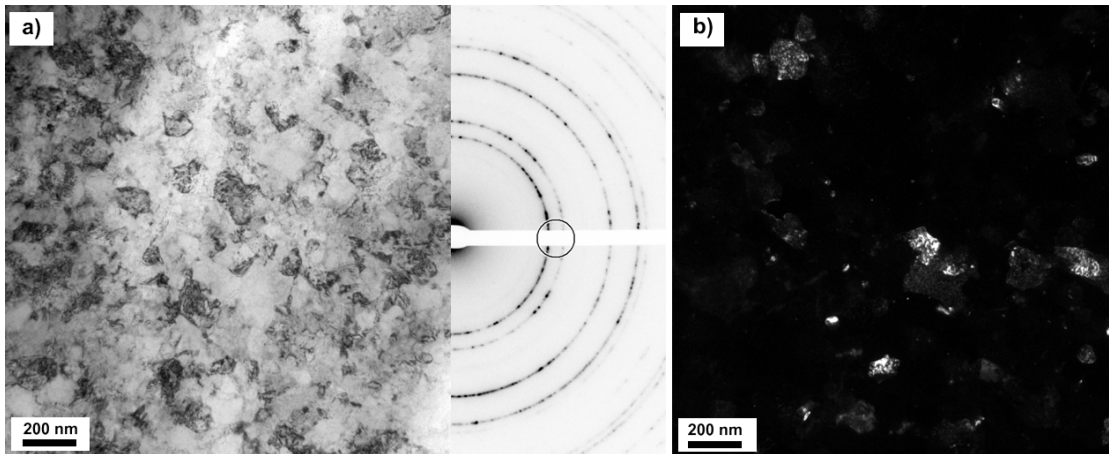


Figure A.5.: a) Bright field TEM image with corresponding SAD pattern and b) dark field TEM image of Ni MMCs with 0.1wt% CNTs after 30 revolutions at 200°C ($r = 2$ mm).

Unfortunately, HPT samples deformed at RT show strong crack formation. At deformation temperatures of 300°C and 400°C, no cracks are observed. Furthermore, a better homogeneity of CNT distribution is obtained at 400°C (see Figure A.3 d). A drawback is, however, the decrease of the saturation hardness at this deformation temperature. By contrast, HPT-deformation at 200°C prohibits crack formation without significant hardness decrease compared to RT and reduces the grain size compared to 400°C HPT (compare Figure A.4 and A.5).

To achieve a microstructure consisting of a Ni matrix with small grain sizes and small, evenly distributed CNT agglomerates, HPT samples were initially deformed for 30 revolutions at 400°C and subsequently deformed for 5 revolutions at RT. Figure A.6 shows the microstructure of a Ni MMC sample with 1wt% CNTs deformed with the aforementioned parameters. In the SEM image (Figure A.6 a) a homogeneous distribution of small, globular CNT agglomerates is visible, while the grains of the Ni matrix are very small. The processed microstructure is also investigated by TEM (Figure A.6 b and c). A nanocrystalline Ni matrix can be seen, in which the grains are below 50 nm in size. The grains are somewhat elongated due to the sample being observed in radial direction (as indicated in Figure A.6

A. *Temperature dependent structural evolution in nickel/carbon nanotube composites*

b). Again, no CNT agglomerates could be identified in TEM. The SAD pattern (inset in Figure A.6 b with annotated dark field spot) shows a slight broadening of the Ni diffraction rings, due to the smaller grain size compared to the sample deformed at RT and 200°C (Figure A.4 and A.5). Additionally, weak diffraction rings of NiO are visible.

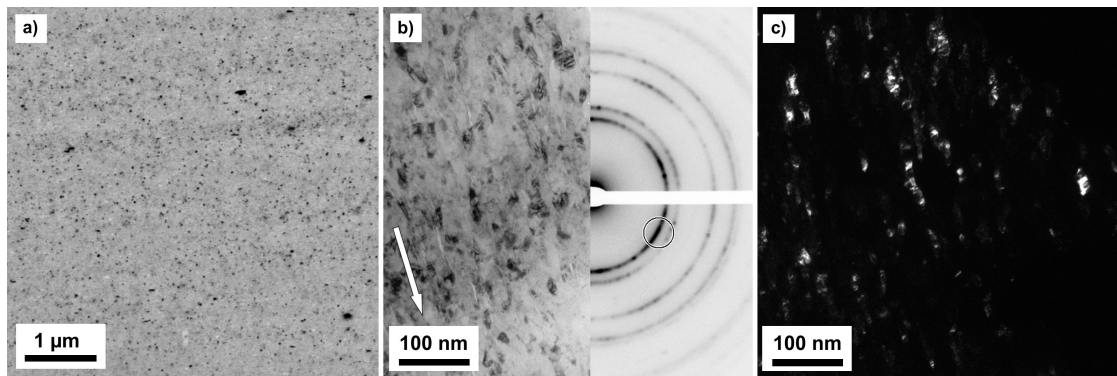


Figure A.6.: a) SEM image, b) bright field TEM image with corresponding SAD pattern and c) dark field TEM image of Ni MMC with 1wt% CNTs after 30 revolutions at 400°C and 5 additional revolutions at RT ($r = 2$ mm). The arrow marks the shear direction.

Ni MMC samples deformed for 30 revolutions at 400°C with additional 5 revolutions at RT exhibit the same crack formation tendency as samples deformed at RT. Hence, HPT parameters were adjusted to 30 revolutions at 400°C with additional 10 revolutions at 200°C. First microstructural investigations show that comparable microstructures can be achieved using this deformation parameters with the advantage of no crack formation after HPT-deformation. Both samples also exhibit the same high hardness of 769 HV. Further adjustments of the HPT parameters and their influence on microstructural evolution are certainly of interest and are currently conducted. For the analysis of the structural defects present in the CNTs after SPD, Raman spectroscopy investigations are underway.

A.4. Conclusion

Ni MMCs with differing amounts of CNTs were processed by HPT. It could be shown that grain size and microhardness depend strongly on the number of revolutions, while CNT agglomerate size, shape and distribution change only slightly. The applied equivalent strain has a more pronounced effect on the grain size and hardness than the differing weight percentages of CNTs.

Increasing the deformation temperature leads to larger grain sizes and a decrease of the hardness in the steady state. CNT agglomerates become smaller, more globular and more evenly distributed with increasing deformation temperature.

Samples, which were deformed for 30 revolutions at 400°C followed by additional 5 revolutions at RT, exhibit the most homogenous microstructure. Crack formation could be prevented by changing the deformation parameters to additional 10 revolutions at 200°C.

Acknowledgment

A. Katzensteiner and A. Bachmaier gratefully acknowledge the financial support by the Austrian Science Fund (FWF): I2294-N36. S. Suarez and K. Aristizabal gratefully acknowledge the financial support from DFG (Grant: SU911/1-1). Additionally, K. Aristizabal would like to thank the German Academic Exchange Service (DAAD) for financial support.

References

- [1] Gleiter H 1989 *Prog. Mater. Sci.* **33** 223–315
- [2] Zhilyaev A P and Langdon T G 2008 *Prog. Mater. Sci.* **53** 893–979
- [3] Islamgaliev R K, Buchgraber W, Kolobov Y R, Amirkhanov N M, Sergueeva A V, Ivanov K V and Grabovetskaya G P 2001 *Mater. Sci. Eng. A* **319–21** 872–6
- [4] Bachmaier A and Pippan R 2011 *Mater. Sci. Eng. A* **528** 7589–95
- [5] Bachmaier A and Pippan R 2013 *Int. Mater. Rev.* **58** 41–62
- [6] Jorio A, Dresselhaus G and Gresselhaus M S 2008 *Carbon Nanotubes: Advanced Topics in the Synthesis, Structure, Properties and Applications* (Topics in Applied Physics vol 111) ed C E Ascheron and A H Duham (Berlin: Springer) chapter 5 pp 165–94
- [7] Jenei P, Yoon E Y, Gubicza J, Kim H S, Labar J L and Ungar T 2011 *Mater. Sci. Eng. A* **528** 4690–95
- [8] Akbarpour M R, Farvizi M, Lee D J, Rezaei H and Kim H S 2015 *Mater. Sci. Eng. A* **638** 289–95
- [9] Suarez S, Lasserre F, Soldera F, Pippan R and Mücklich F 2015 *Mater. Sci. Eng. A* **626** 122–7
- [10] Reinert L, Zeiger M, Suarez S, Presser V and Mücklich F 2015 *RSC Adv.* **5** 95149–59
- [11] Suarez S, Lasserre F, Prat O and Mücklich F 2014 *Phys. Stat. Sol. A* **211** 1555–61

References

- [12] Hohenwarter A, Bachmaier A, Gludovatz B, Scheriau S and Pippan R 2009 *Int. J. Mater. Res.* **100** 1653–61
- [13] Stüwe H P 2003 *Adv. Eng. Mater.* **5**, 291–5
- [14] An X H, Lin Q Y, Wu S D, Zhang Z F, Figueiredo R B, Gao N and Langdon T G 2011 *Phil. Mag.* **91:25**, 3307–26
- [15] Pippan R, Scheriau S, Taylor A, Hafok M, Hohenwarter A and Bachmaier A 2010 *Annu. Rev. Mater. Res.* **40**, 319–43
- [16] Bachmaier A, Hohenwarter A and Pippan R 2009 *Scripta Mater.* **61**, 1016–9

B. Influence of Processing Parameters on the Mechanical Properties of HPT-Deformed Nickel/Carbon Nanotube Composites

Authors

Andreas Katzensteiner¹, Timo Müller^{1*}, Karoline Kormout¹, Katherine Aristizabal², Sebastián Suarez², Reinhard Pippan¹ and Andrea Bachmaier¹

¹ Erich Schmid Institute, Jahnstr. 12, A-8700 Leoben, Austria

² Department of Materials Science, Campus D3.3, D-66123 Saarbrücken, Germany

*Current address: Deutsches Elektronen-Synchrotron DESY, Photon Science, Hamburg, Germany

Journal

Advanced Engineering Materials; 2018; 1800422

Abstract

Nickel/carbon nanotube (Ni/CNT) composites with varying amounts of CNTs are deformed by high-pressure torsion (HPT) at different deformation temperatures to high strains, where no further refinement of the Ni matrix microstructure is observed. Mean Ni grain sizes increase with increasing HPT-deformation temperature, while the size of the CNT agglomerates is significantly reduced. Additionally, the distribution of the agglomerates in the metal matrix becomes more homogenous. To investigate the mechanical performance of the HPT-deformed composites, uniaxial tensile and compression tests are conducted. Depending on the HPT-deformation temperature and the resulting microstructure, either brittle or ductile fracture occurs, and the ultimate tensile strength varies between 900 and 2100 MPa. Increased HPT-deformation temperatures induce a decrease in the anisotropy of the mechanical properties, mainly caused by a shrinking of the CNT agglomerates. It is shown, that tuning the HPT-deformation temperature is the key for optimizing both the microstructure and the mechanical performance.

B.1. Introduction

Processing of metal matrix nanocomposites (MMCs) by severe plastic deformation (SPD) has gathered much interest in the materials science community because of the possibility of this method to not only create a nanograined or ultrafine grained microstructure, but also to disperse the second phase particles homogeneously throughout the metal matrix [1]. These second phase particles are known to improve the mechanical properties of pure metals, due to their ability to pin dislocations and grain boundaries as well as to act as reinforcing phase. In nanocrystalline materials, they also inhibit grain growth, which improves the thermal stability of SPD processed metals [2].

Carbon nanotubes (CNTs) consist of rolled up sheets of graphene, either single or multilayered, and possess outstanding material properties, such as high specific strength and high thermal conductivity [3]. These properties make them promising candidates as reinforcing phase for MMCs [4], and the strength and

ductility of such CNT/metal composites are the subject of several studies, using severe plastic deformation (SPD) processes, such as high-pressure torsion (HPT) or equal channel angular pressing (ECAP) [5–7], and other processing techniques, for example, electrodeposition [8–12]. Contrary to other carbon allotropes, such as nanodiamonds, CNTs are known to form large agglomerates when dispersed in MMCs [13]. The breaking-up and dispersion of these agglomerates, which has a significant influence on the mechanical performance of the MMCs, is therefore of utmost importance for improving the properties of such composites.

An often used method to investigate the mechanical properties of HPT-deformed bulk materials is tensile testing [14–16]. Tensile tests are used as a direct measurement of the yield strength and the ultimate tensile strength (UTS), the uniform elongation, the stress and strain at fracture, and the Young's modulus. Due to the size limitations of HPT processed samples, special care has to be exercised on the fabrication of appropriate tensile test specimens with these dimensions, since proportional standards for tensile test specimens are only given for larger samples, as used in industrial environments [17, 18].

The majority of studies on the topic of CNT-reinforced metals come to the conclusion, that the addition of CNTs as second phase particles has a beneficial impact on the strength and ductility. Yoon et al. [5] showed, that the addition of 5 or 10 vol% of CNTs to pure Cu and a subsequent HPT-deformation of up to 10 revolutions increases the UTS from 190 MPa to 352 and 345 MPa, respectively. A similar UTS increase has been reported by Asgharzadeh and Kim [7] in Al reinforced with 3 vol% CNTs and HPT-deformed up to 10 revolutions. Other consolidation methods have also shown to improve the mechanical properties of CNT reinforced metals. Yang et al. [8] reported a 1.7 times higher UTS and an elongation about 18% higher of ball-milled and extrusion-sintered Al containing 2.5 wt% CNTs compared to pure Al. Spark plasma sintered Cu mixed with 5 vol% CNTs showed a comparable strength increase [9].

The mechanical properties of Ni, as metal basis in different carbon-based reinforced composites, have been the subject of several studies as well. An increase

B. Influence of Processing Parameters on the Mechanical Properties

of the UTS by a factor of almost two without a decrease in ductility, compared to pure Ni, through the addition of carbon impurities between 0.008 and 0.06 wt% and subsequent HPT-deformation, has been reported by Rathmayr and Pippan [16]. On the other hand, a study by Archakov et al. [19] revealed a decrease in the ductility, but no increase in the UTS in ball milled and sintered Ni powder with 0.5 to 2 wt% of thermally expanded graphite, compared to pure Ni. Dai et al. [12] showed a hardness and UTS increase of CNT reinforced electrodeposited Ni, compared to the pure metal without significant loss of ductility.

A previous study of our group has shown, that the HPT-deformation temperature has a strong influence on the hardness of Ni/CNT composites with up to 3 wt% CNT content and also on the dispersion of the CNTs in the Ni matrix [20]. Therefore, a two temperature deformation process has been developed to optimize hardness, grain size, CNT agglomerate size, and CNT distribution in the metal matrix of these composites.

In this study, the influence of the HPT-deformation temperature on the strength and ductility of Nickel composites, with up to 3 wt% of CNTs has been investigated by tensile and compression tests, in order to optimize the mechanical performance. While tensile tests [21, 22] and ultrasonic velocity measurements [23] have been used in previous studies to investigate the mechanical anisotropy of SiC reinforced MMCs, it is, to the best of our knowledge, the first time that compression tests have been used to investigate the anisotropy of HPT-deformed Ni/CNT MMCs and the influence of deformation temperature and CNT distribution on it.

B.2. Experimental Section

Ni/CNT composites were produced via colloidal mixing of Ni dendritic powder (Alfa Aesar, -325 mesh) with Multiwall CNTs (Graphene Supermarket, USA, purity > 95%, individual particle diameter of 20–85 nm, mean length between 5-15 μm) in an ethylene glycol dispersion according to ref. [13] with final CNT weight percentages of 0.1, 0.25, 0.5, 1, 2, and 3. These weight percentages correspond to volume percentages of 0.42, 1.04, 2.08, 4.17, 8.33, and 12.5. The composite

B.2. Experimental Section

samples had a diameter of 8 mm and a height of about 1 mm. HPT was used at a velocity of 0.6 revolutions per minute and a hydrostatic pressure of 7.5 GPa, to obtain a saturated microstructure, as described in ref. [24]. The varied processing parameters were the deformation temperature and the number of revolutions, deforming either for 30 revolutions at room temperature, 200, 300, and 400°C or using a two-temperature deformation process with 30 revolutions at 400°C and subsequent 10 revolutions at 200°C. From each HPT sample, two tensile test specimens were produced with a recently developed fabrication method for round, small-scale tensile specimens, which allowed a high-accuracy fabrication with negligible material change [18, 25]. Tensile tests of samples HPT-deformed at room temperature were not conducted in this study, because of the high disposition of such samples to develop cracks during deformation, which excluded them from valid tensile testing. The gauge length was 2.5 mm and the diameter was between 300 and 500 μm . Hence, a ratio of gauge length to gauge diameter of 5:1 to 8:1 was achieved. The tensile axis was set to be about 2 mm from the center of the HPT disc to ensure full microstructural saturation in the testing region and long enough pulling shoulders on both sides to avoid a pull-out of the specimens from the grips. Tensile tests were then performed on a Kammrath & Weiss tensile stage with a 2 kN load cell and a testing velocity of $2.5 \mu\text{m s}^{-1}$ at room temperature. The complete tensile test setup and the evaluation software are thoroughly described in refs. [18, 25]. After tensile testing, the fracture surfaces were investigated with a scanning electron microscope (SEM) type LEO 1525 equipped with an In-lens detector.

For the compression tests, three small cubes with side lengths of about 1 mm were cut from each HPT sample at a radius of about 3 mm from the disc center and polished with fine abrasive paper to get smooth, parallel surfaces. These cubes were then each compressed along one of the three directions, as depicted in Figure B.1 (axial, radial and tangential), in the Kammrath & Weiss tensile/compression module with a 10 kN load cell and a testing velocity of $0.5 \mu\text{m s}^{-1}$ at room temperature. Test setup and data evaluation were analogous to the tensile tests. The microstructure of the 2 wt% CNT samples was investigated with SEM using a back scattered electron (BSE) detector and with a transmission electron microscope (TEM) JEOL

B. Influence of Processing Parameters on the Mechanical Properties

2100F. The SEM images were recorded in tangential direction at a radius of 3 mm and the TEM images were recorded in axial direction at a radius of 2 mm. To determine the anisotropy of the microstructure, additional micrographs of the HPT samples were recorded with SEM in axial and radial direction at a radius of 3 mm.

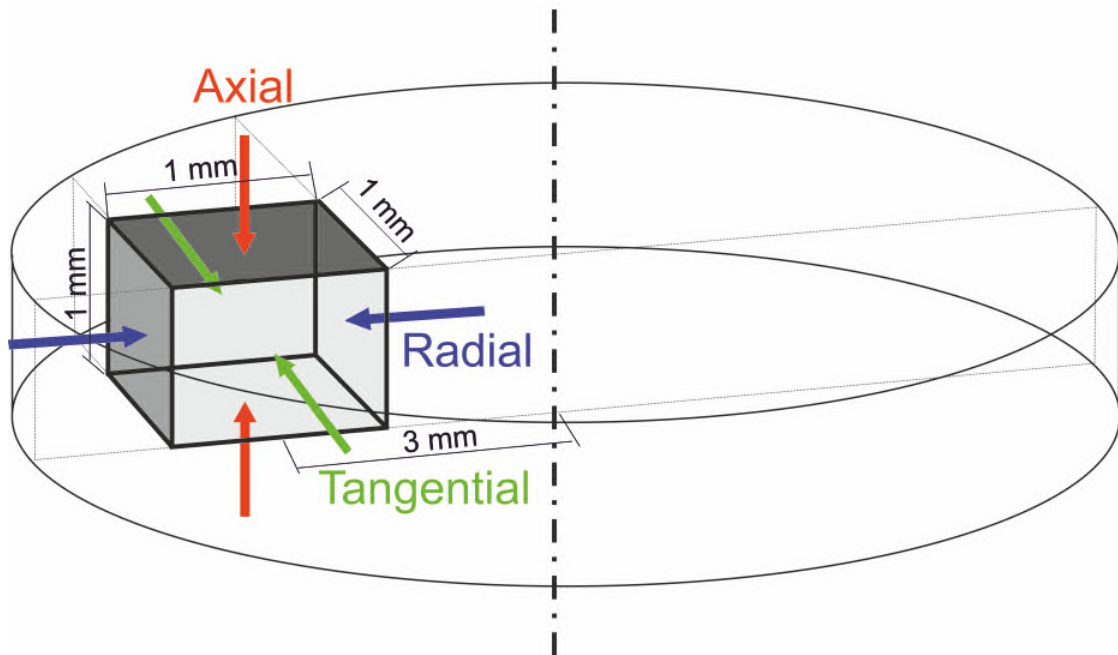


Figure B.1.: Schematic of a compression test specimen cut from an HPT disc with the orientations of the acting forces in each test direction.

B.3. Results and Discussion

B.3.1. Microstructural development

The influence of the deformation temperature on the microstructure and the hardness of Ni/CNT MMCs has been described in ref. [20]. It was shown, that the HPT-deformation temperature has a strong influence on the hardness, the grain size of the Ni matrix and the agglomerate sizes of the CNTs, and their distribution in the metal matrix. Figure B.2 exemplarily shows the microstructural change of a

2 wt% Ni/CNT composite with increasing HPT-deformation temperature. HPT at 200 °C results in large, irregular CNT agglomerates, imbedded inhomogeneously in a nanograined Ni matrix (Figure B.2 a). Increasing the HPT-deformation temperature to 300 and 400 °C (Figure B.2 b, c, respectively) leads to an increase in the Ni matrix grain size, a decrease in the size of the CNT agglomerates and a homogenization of the CNT distribution in the matrix. A two-temperature deformation process has been shown to optimize the microstructure, resulting in a Ni matrix with grain sizes smaller than 100 nm and mostly small, homogeneously distributed CNT agglomerates (Figure B.2 d). Some larger agglomerates are still present in this sample due to the high amount of CNTs. Figure B.3 a shows the corresponding hardness evolution of these samples, with a decrease in the saturation hardness with increasing HPT-deformation temperature from 702 HV down to 458 HV and a hardness increase up to 855 HV of the sample deformed at two temperatures.

B.3.2. Mechanical properties

The results of the tensile tests reveal a strong influence of the deformation temperature on the mechanical properties of the composites. Figure B.3 b exemplarily shows this for the specimens with 0.25 and 2 wt% CNT content. Both specimens HPT-deformed at a temperature of 200 °C, show fracture in the elastic regime, with a fracture stress of 2121 and 2066 MPa, respectively. At 300 °C, the 0.25 wt% specimen shows a stronger decrease in the UTS down to 1338 MPa, and a higher fracture strain of 4%, than the 2 wt% specimen with 1558 MPa UTS and 0.5% fracture strain. A further increase in the deformation temperature to 400 °C decreases the UTS to 892 MPa on the 0.25 wt% specimen, and to 1221 MPa on the 2 wt% specimen. The ductility increases to 4.9% and 2.1% fracture strain, respectively. The UTS and ductility of the specimen with low CNT content, deformed with the two-temperature process, is relatively high (1671 MPa with 3.1% fracture strain). The specimen with high CNT content fails in the elastic regime, even after deformation with the two-temperature process.

B. Influence of Processing Parameters on the Mechanical Properties

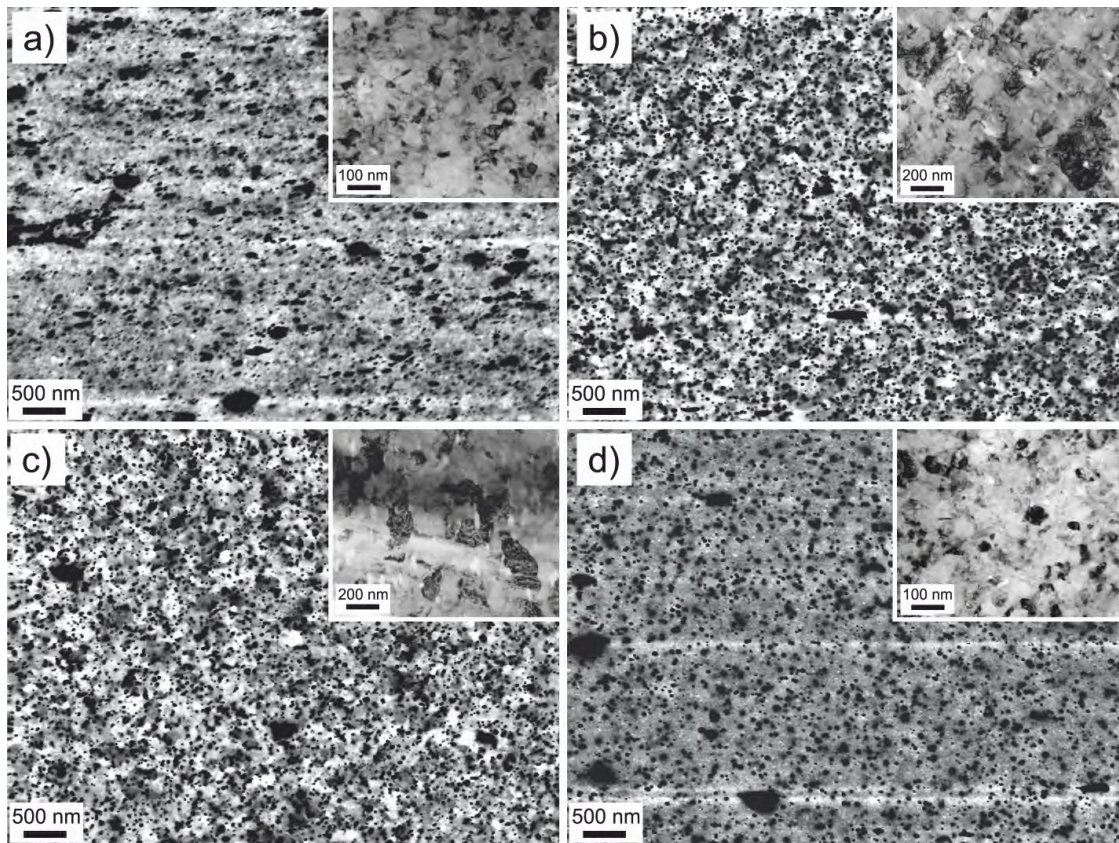


Figure B.2.: Microstructure images of 2wt% Ni/CNT samples at a radius of 3mm after HPT-deformation at a) 200°C, b) 300°C, c) 400°C, and d) 400 + 200°C (The inlays show TEM images taken with higher magnification at approximately the same position).

Figure B.4 displays UTS, yield strength, uniform elongation, and reduction in area of the tensile tests of all CNT weight percentages and deformation temperatures. Specimens with more than 1 wt% CNTs, deformed at 200°C or with the two-temperature process, failed in the elastic regime and, therefore, showed no plastic yield. In this case, the fracture stress is plotted instead of the UTS. The UTS (Figure B.4 a) and the yield strength (Figure B.4 b) show no clear relationship to the amount of CNTs. A similar trend was observed from hardness measurements, where no significant increase in the hardness with increasing CNT content was determined [20]. Another influencing factor is the HPT-deformation

B.3. Results and Discussion

temperature. The 400°C specimens show the lowest UTS and yield strength values. Higher values are obtained for the specimens deformed at 300°C in accordance with hardness measurements [20]. For the other temperatures (200°C and the two-temperature process), no clear temperature influence on UTS and yield strength for specimens ≤ 1 wt% CNTs can be discerned, but generally the highest values are achieved. The uniform elongation and reduction in area are plotted in Figure B.4 c and d, respectively. At low CNT contents, there is no evident influence of the HPT-deformation temperature on the uniform elongation. The uniform elongation is, however, influenced by the deformation temperature at higher CNT contents, where it is considerably higher after deformation at 400°C compared to deformation at 300°C. The reduction in area (Figure B.4 d), as a second measure of ductility, is more dependent on the CNT content than on the HPT-deformation temperature and decreases strongly with increasing CNT content. Furthermore, the reduction in area is generally lower for higher CNT contents at all HPT-deformation temperatures.

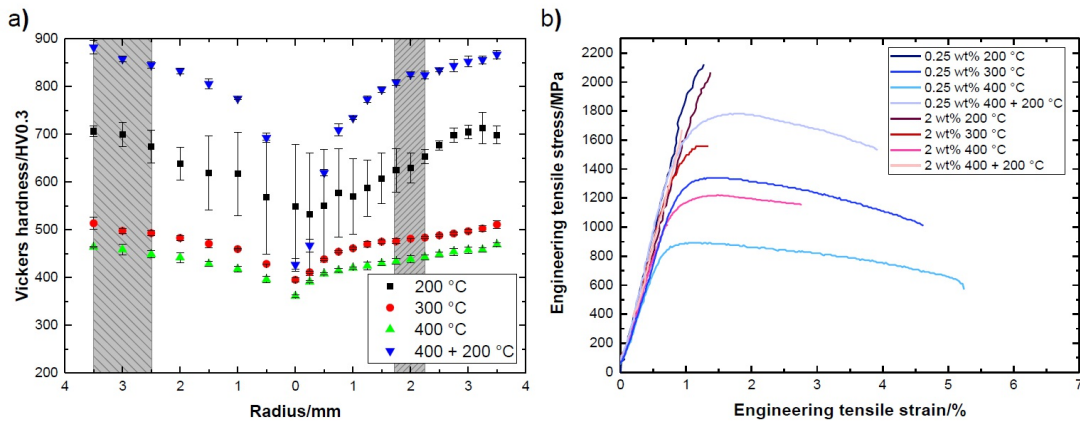


Figure B.3.: a) Vickers hardness as function of the HPT disc radius of Ni MMCs with 2wt% CNTs, HPT-deformed at 200°C, 300°C, 400°C, and 400 + 200°C. The left and right gray areas indicate the compression region and the tensile test region, respectively. b) Engineering tensile stress-strain curves of Ni MMCs with 0.25 and 2wt% CNTs, HPT-deformed at 200°C, 300°C, 400°C, and 400 + 200°C

B. Influence of Processing Parameters on the Mechanical Properties

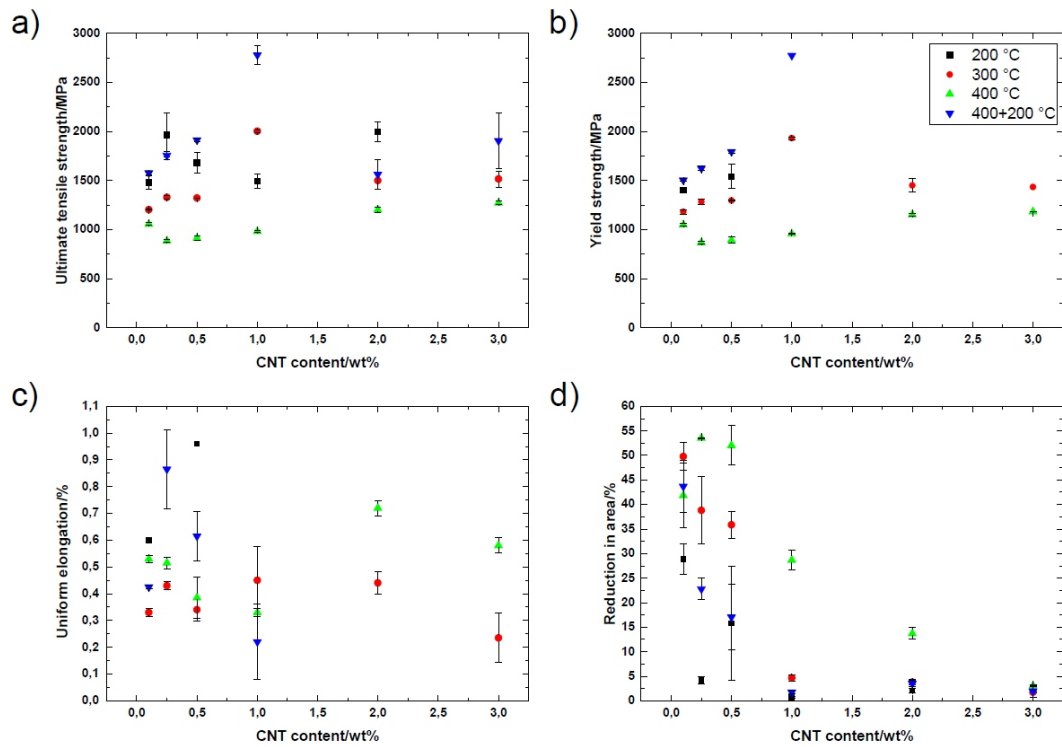


Figure B.4.: UTS a), yield strength b), uniform elongation c), and reduction in area d) as functions of the CNT content for specimens HPT-deformed at different temperatures.

To evaluate the fracture surface of the tensile specimens, SEM micrographs were obtained. Figure B.5 exemplarily shows the fracture surfaces of the 2 wt% specimens, HPT-deformed at a) 200°C, b) 300°C, c) 400°C, and d) 400 + 200°C. The specimen deformed at 200°C shows a brittle fracture surface, while higher deformation temperatures resulted in the typical cup-and-cone micro-ductile fracture. The specimen deformed with the two-temperature process also shows a brittle fracture surface. High magnification images, however, reveal the presence of dimples even in the specimens with generally brittle fracture surfaces. The size of those dimples seems to vary with the deformation temperature, and therefore with the grain size. Depending on the CNT content, the fracture surfaces show a varying amount of large and irregular inclusions in specimens deformed at 200°C and small, more

disc-like inclusions in specimens deformed at higher temperatures (as indicated by arrows in Figure B.5). These features are most likely CNT agglomerates.

Compared to tensile test results of pure Ni [15] and Ni mixed with 0.5–2 wt% thermally expanded graphite (TEG), which was ball-milled to create a nickel-graphene-graphite composite [19], the combination of Ni with high amounts of CNTs leads to an increase of the UTS, but also to a decrease in ductility even at higher HPT-deformation temperatures. These results are also in contrast to the findings of ref. [16], where the addition of carbon impurities between 0.06 and 0.008 wt% to HPT-deformed Ni were not enough to cause embrittlement due to carbon content at the grain boundaries. Similar results were obtained with Ni/CNT composites fabricated by electrodeposition [12]. The differences might be due to the higher carbon content in the present study, and the agglomerates, which could not be completely dissolved during HPT.

In ref. [16], the carbon content, as well as the HPT-deformation temperature controlled the final saturation grain size. The hardness, which increased with decreasing grain size from 300 HV at a grain diameter of 400 nm, to 550 HV at a grain diameter of 120 nm, follow the Hall–Petch relation. Additionally, a linear trend was obtained if the hardness was plotted as function of the fourth root of the carbon content, which reflects the dependence of the grain boundary mobility on the carbon content [16]. In this study, specimens from samples deformed at room temperature could not be included in the tensile test results due the often observed crack formation during HPT processing or their high premature failure rate during tensile testing. Also samples deformed at 200°C and at two temperatures display a large scatter in the tensile test data due to their brittle failure in the elastic regime. To compare our results with ref. [16], the hardness for all CNT contents and HPT-deformation temperatures is plotted as function of grain size in Figure B.6 a. The mean grain sizes were measured from TEM images for the 2 wt% samples and from SEM images for all other samples, using the equivalent diameter method. Additionally, the data points available from ref. [16] are displayed. A linear relation with a similar slope as in ref. [16] with small deviations at smaller grain sizes is obtained for the Ni/CNT MMCs of this study. A

B. Influence of Processing Parameters on the Mechanical Properties

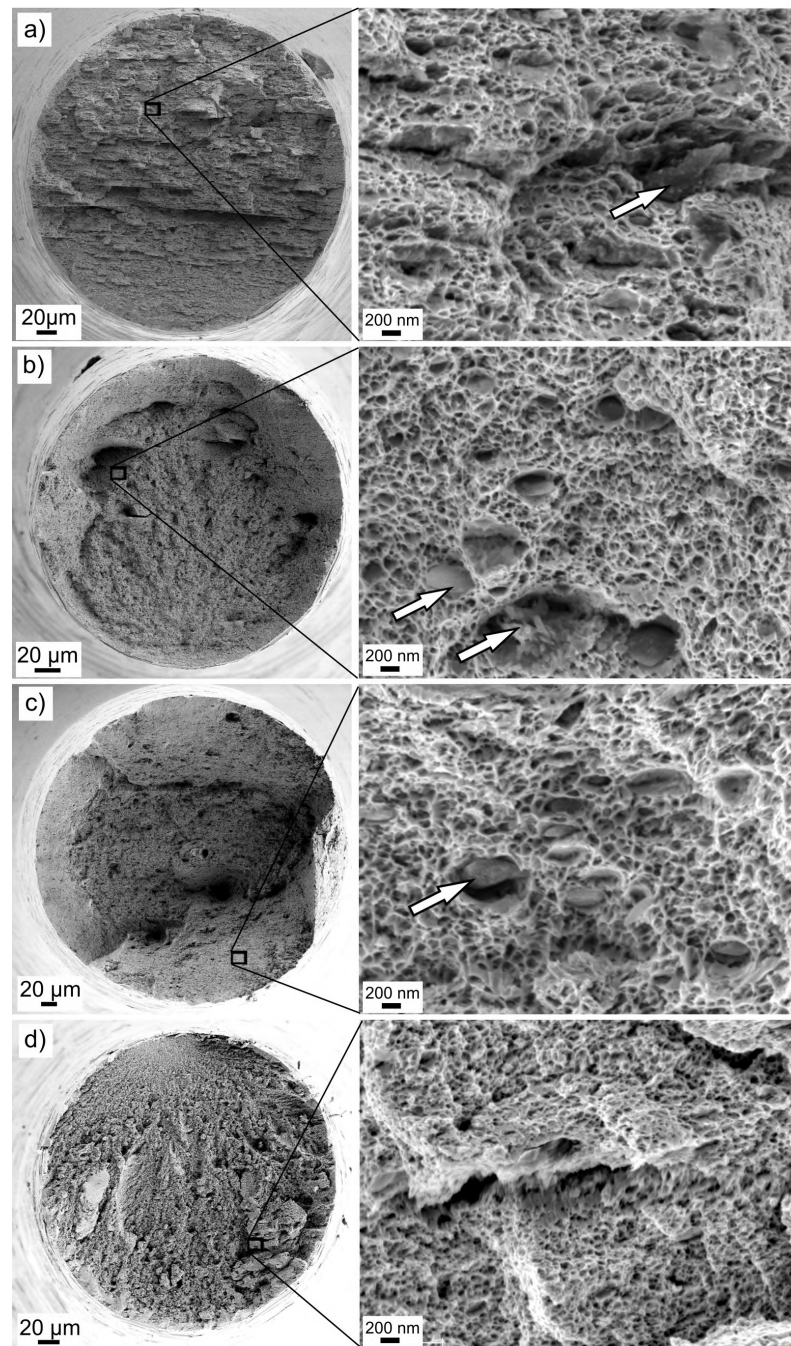


Figure B.5.: Fracture surfaces and detail fracture surfaces of Ni MMCs with 2wt% CNTs HPT-deformed at a) 200°C, b) 300°C, c) 400°C, and d) 400 + 200°C. CNT agglomerates are marked by arrows.

Hall–Petch relationship between the grain size and the hardness was also found by Suarez et al. [26] in CNT-reinforced nickel at larger grain sizes, by Kim et al. [9] in CNT-reinforced Cu, and by Choi et al. [11] in CNT-reinforced aluminum. It thus strengthens the argument, that the hardness increase of MMCs with CNTs as reinforcing phase is the result of a decreased grain size and the grain boundaries being obstacles for dislocation motion. Nonetheless, there can be other mechanisms at play, such as the dislocation density (work hardening) and the particle dispersion (Orowan strengthening). The latter strengthening mechanism is only valid for CNT agglomerates being smaller than the Ni matrix grain size and thus there is only a small or even negligible contribution to the strength of the composites in this study. CNT agglomerates larger than the grain size do not contribute to the strength substantially.

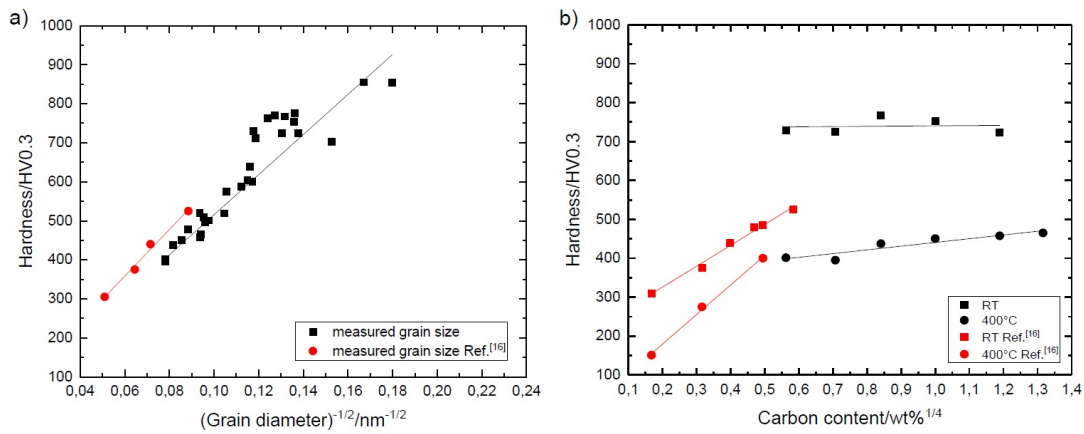


Figure B.6.: a) Saturation hardness as a function of grain size. The red data points are taken from ref. [16]. b) Saturation hardness as function of carbon content for two different HPT-deformation temperatures. The red data points are taken from ref. [16].

In Figure B.6 b, the hardness is plotted as a function of the carbon content for CNT samples deformed at room temperature and at 400°C and compared to the hardness data of ref. [16](only data for room temperature and 400°C available). For both Ni/CNT MMCs, a linear relation is obtained as well. The slope of the

B. Influence of Processing Parameters on the Mechanical Properties

curves are, however, considerably smaller. A decreased slope suggests a smaller influence of carbon on the saturation grain size after HPT-deformation [16]. In ref. [16], the carbon is mainly enriched along the grain boundaries and has thus a large effect on the final grain size after HPT-deformation. In ref. [27], the evolution of the CNT distribution homogeneity is thoroughly analyzed and different size descriptors and shape factors for the CNT agglomerates were obtained. It was shown that the diameter and the nearest neighbor distance of the CNT agglomerates decreased with increasing strain, but the CNT area fraction did not change significantly with increasing strain values. Thus, it is assumed that the carbon in this study is mostly present as CNTs in the agglomerates as well and might be only to a small part enriched at the grain boundaries. However, a ratio between the carbon present in CNT agglomerates and at the grain boundaries cannot be determined.

The CNT content has, however, a bigger influence on the ductility of the composites than on the hardness, the UTS and the yield strength, especially after deformation at two temperatures, where low (<1 wt%) amounts of small CNT agglomerates lead to a combination of relatively high ductility and high UTS, whereas high (>1 wt%) CNT content specimens show a generally brittle behavior. Since pure Ni shows ductile fracture even for nanoscaled grain sizes [15], a possible explanation for these results is, that the ductility is mainly governed by the number of CNT agglomerates which serve as micro defects in the Ni matrix. Due to the high amount of CNTs not all agglomerates can be reduced in size. Their size, shape, and concentration are thought to be one of the main criteria for the type of fracture (c.f. Figure B.2, B.5). Especially the large, irregular CNT agglomerates can act as fracture nuclei due to being a bundle of mechanically interlocked CNTs with high strength, which are then strongly compressed and damaged during HPT-deformation [13].

In the region near the UTS, these micro defects grow and build up pores. Between these larger pores, small pores in the Ni matrix develop as consequence of the multi-axial stress distribution. Both types of pores subsequently grow until final fracture occurs. The size of the two different kinds of pores of the samples

deformed at 200°C and 400 + 200°C (Figure B.5 a, d) is clearly different, whereas the fracture surfaces of the samples deformed at 300 and 400°C display pores with a more comparable size (Figure B.5 b, c). This could be a consequence of the different microstructure (cf. Figure B.2), where the samples deformed at 200°C and 400 + 200°C show CNT agglomerates larger than the Ni grain size, and the samples deformed at 300 and 400°C show CNT agglomerates smaller or the same size as the Ni grains. Similar behavior has been found in Al/SiC MMCs, where the fracture surfaces of tensile specimens show a brittle fracture of the SiC particles in a dimpled fracture of the Al matrix [22].

B.3.3. Anisotropy

Our results regarding the mechanical anisotropy obtained by compression testing are shown in Figure B.7. The compressive stress is plotted as a function of the compressive strain of specimens with 0.25 and 2wt% CNTs, HPT-deformed at a) 200°C, b) 300°C, c) 400°C, and d) 400 + 200°C. After HPT-deformation at 200°C, both compositions show low ductility, high yield stresses of up to 3000 MPa and a distinct anisotropy, indicated by a strong disparity of the yield stress between the three tested orientations (Figure B.7 a). Increasing the HPT-deformation temperature to 300°C increases the ductility and decreases the yield stress for both specimens. The anisotropy also decreases, showing a similar decline in both specimens (Figure B.7 b). Only in radial direction, the 2wt% specimen shows a different behavior. At 400°C HPT-deformation temperature, both specimens show a further decrease of the yield stress down to about 1100 MPa and a high ductility similar to the 300°C specimens. The 2wt% specimen still shows some anisotropy (Figure B.7 c). The specimens obtained by the two-temperature deformation process, shown in Figure B.7 d, reveal a clear disparity of the mechanical behavior of low-CNT specimens and high-CNT specimens. While the 0.25wt% specimens show a high yield stress and ductility in combination with a low anisotropy, the 2wt% specimens display a very brittle behavior with a high maximum stress. The fracture mode during compression clearly depends on the CNT content. Specimens with low CNT content deform either ductile or by shear band formation and strain localization at an angle of about 45° depending on the HPT-deformation tempera-

B. Influence of Processing Parameters on the Mechanical Properties

ture. High CNT content specimens on the other hand fail generally through brittle fracture.

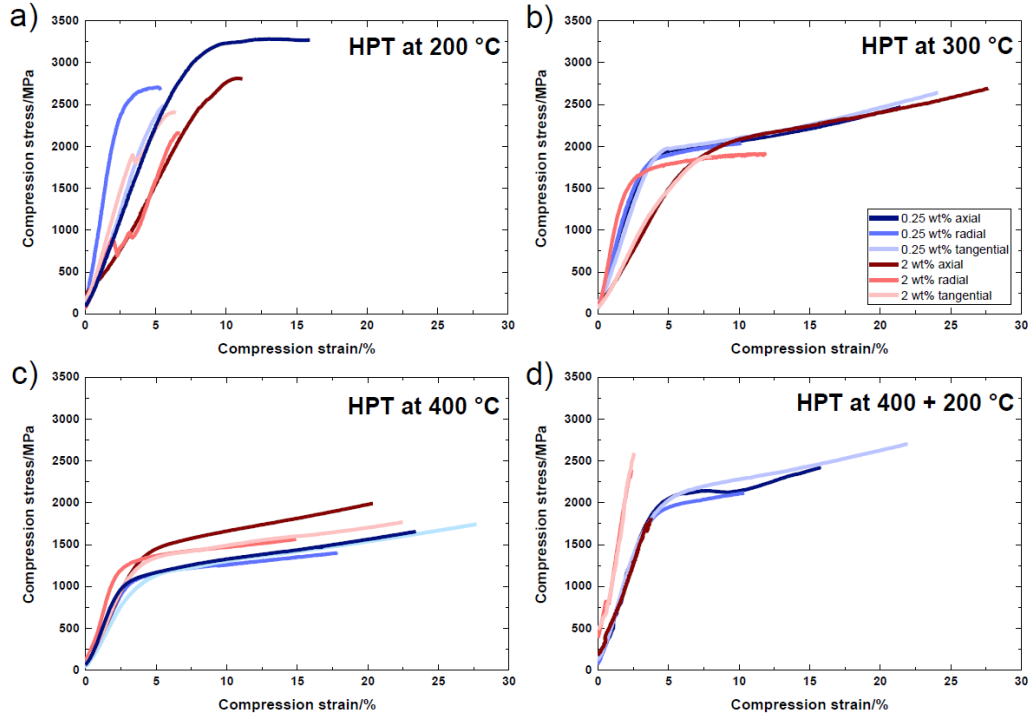


Figure B.7.: Compression stress-strain curves in axial, radial and tangential direction of Ni MMCs with 0.25 and 2wt% CNTs, HPT-deformed at a) 200°C, b) 300°C, c) 400°C, and d) 400 + 200°C.

To assess how much the size and shape of the CNT agglomerates play a role in the anisotropy of the composites, SEM images of the microstructure have been taken in tangential, radial and axial direction at a HPT disc radius of 3 mm. Figure B.8 shows these images for samples with 2wt% CNTs. At the lowest HPT-deformation temperature (Figure B.8 a–c), large, irregular CNT agglomerates are inhomogenously dispersed in a fine grained Ni matrix. These agglomerates are mainly stretched in shear direction (Figure B.8 b, c), but also slightly elongated in radial direction (Figure B.8 a). An increase of the deformation temperature to 300°C leads to an increase in the mean grain size of the Ni matrix (Figure B.8

d–f) and to a decrease of the mean agglomerate size, which are also more homogeneously distributed while still elongated in shear direction. Figure B.8 g–i show an increase in the Ni matrix grain size at an HPT-deformation temperature of 400°C, while the agglomerate size and elongation is comparable to the samples deformed at 300°C. The SEM images of the sample deformed at two temperatures (400 and 200°C) show a Ni matrix with very small grains and small, evenly distributed CNT agglomerates (Figure B.8 j–l). These CNT agglomerates are, however, elongated in the shear direction as well.

A decrease of the anisotropy of the mechanical properties, especially of the ductility, with increasing deformation temperature is observed in the compression tests, although the CNT agglomerates are elongated in shear direction in all investigated samples (Figure B.7). This can be attributed to the mean size decrease of elongated CNT agglomerates. A comparison between Figure B.7 and B.8 shows accordance between the decrease of the anisotropy and the decrease of the agglomerate sizes. Because of the high CNT content in the 2 wt% sample, some larger agglomerates, randomly distributed in the matrix, remain even after deformation at higher temperatures (300°C and 400°C). This explains the higher anisotropy of the 2 wt% specimens compared to the 0.25 wt% specimen at these deformation temperatures (Figure B.7). Similar results were obtained by Ganesh and Chawla [22] with SiC reinforced Al MMCs. They showed, that an increase in the volume fraction of the reinforcing particles increases the anisotropy of the MMCs during tensile tests.

HPT-deformed microstructures often consist of elongated grains, which are aligned nearly parallel to the shear plane and display a shear texture. An orientation dependency of the mechanical properties in Ni/CNT MMCs is also caused by the grain shape (grain aspect ratio) and the shear texture of the grains of the Ni matrix. In a previous study, TEM images of a Ni/CNT MMC sample with 1 wt% CNTs, HPT-deformed for 30 revolutions at 400°C and additional 5 revolutions at room temperature, show an elongation of the Ni grains in the Ni/CNT MMCs as well [20]. The influence of the grain aspect ratio and orientation on the anisotropy of HPT-deformed Ni was already investigated by Rathmayr et al. [14] and cannot be entirely ruled out for the Ni/CNT MMCs. In ref. [14], however, no influence

B. Influence of Processing Parameters on the Mechanical Properties

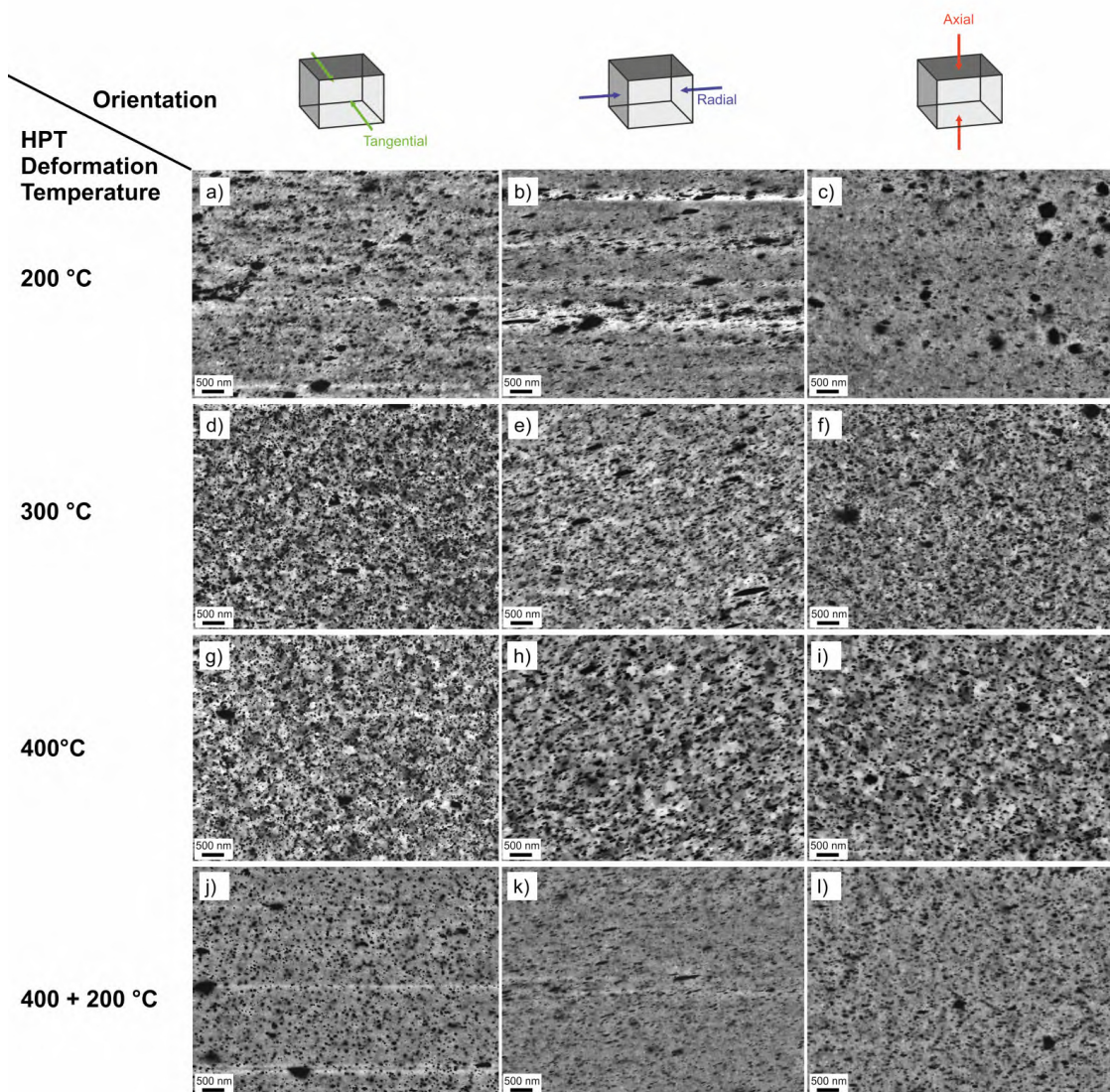


Figure B.8.: SEM images at 3mm radius in tangential, radial, and axial direction of Ni MMCs with 2 wt% CNTs, HPT-deformed at 200°C a-c), 300°C d-f), 400°C g-i), and 400 + 200°C j-l).

of the grain aspect ratio on the UTS and the uniform elongation was found and the observed difference in the UTS of about 100 MPa was attributed to the shear texture. If the shear texture plays a role in the compression strength of the investigated Ni/CNT MMCs, specimens oriented parallel to the shear plane (i.e., tangential testing direction) should have a higher compression strength than spec-

imens oriented perpendicular to the shear plane (i.e., axial testing direction) [14], which is not observed (Figure B.7).

B.4. Summary

Ni/CNT MMCs with varying amounts of CNTs were HPT-deformed at different temperatures and their mechanical performance was evaluated. Tensile tests showed that decreasing the deformation temperature has a stronger influence on the UTS of the composites than the CNT content. The UTS of specimens deformed with a two-temperature process was almost as high as that of the 200°C specimens but provides a better ductility at low CNT contents. In general, the CNT content has a strong influence on the ductility, especially after the two-temperature deformation, where only specimens with 1 wt% and higher showed a brittle fracture behavior.

An overall brittle fracture behavior was observed for specimens deformed at 200°C, whereas ductile failure for specimens deformed at higher temperatures was observed. The difference in the fracture mode can be ascribed to the dependence of the size and shape of the CNT agglomerates on the deformation temperature. Compression tests showed that the anisotropy of mechanical properties decreases with increasing deformation temperature. Microstructural observations of all tested orientations suggest that the anisotropy measured in the compression tests is mainly determined by the size and shape of the CNT agglomerates.

Acknowledgments

A. Katzensteiner and A. Bachmaier gratefully acknowledge the financial support by the Austrian Science Fund (FWF): I2294-N36. S. Suarez and K. Aristizabal gratefully acknowledge the financial support from DFG (Grant: SU911/1-1). Additionally, K. Aristizabal would like to thank the German Academic Exchange Service (DAAD) for financial support.

Conflict of Interest

The authors declare no conflict of interest.

Keywords

carbon nanotubes, high-pressure torsion, mechanical properties, metal matrix composites, nickel

References

- [1] H. Li, A. Misra, Z. Horita, C. C. Koch, N. A. Mara, P. O. Dickerson, Y. Zhu, *Appl. Phys. Lett.* 2009, 95, 19.
- [2] P. Jenei, J. Gubicza, E. Y. Yoon, H. S. Kim, J. L. Lábár, *Compos. Part A Appl. Sci. Manuf.* 2013, 51, 71.
- [3] T. Yamamoto, K. Watanabe, E. R. Hernández, *Carbon Nanotubes, Topics Applied Physics*, Vol. 111 (Eds: A. Jorio, G. Dresselhaus, M. S. Dresselhaus), Springer, Berlin, Heidelberg, Germany 2008, pp. 165–195.
- [4] S. R. Bakshi, D. Lahiri, A. Agarwal, *Int. Mater. Rev.* 2010, 55, 41.
- [5] E. Y. Yoon, D. J. Lee, B. Park, M. R. Akbarpour, M. Farvizi, H. S. Kim, *Met. Mater. Int.* 2013, 19, 927.
- [6] H. Zare, M. Jahedi, M. R. Toroghinejad, M. Meratian, M. Knezevic, *Mater. Des.* 2016, 106, 112.
- [7] H. Asgharzadeh, H. S. Kim, *Arch. Metall. Mater.* 2017, 62, 1109.
- [8] X. Yang, E. Liu, C. Shi, C. He, J. Li, N. Zhao, K. Kondoh, *J. Alloys Compd.* 2013, 563, 216.
- [9] K. T. Kim, J. Eckert, S. B. Menzel, T. Gemming, S. H. Hong, *Appl. Phys. Lett.* 2008, 92, 3.
- [10] B. Chen, K. Kondoh, H. Imai, J. Umeda, M. Takahashi, *Scr. Mater.* 2016, 113, 158.
- [11] H. J. Choi, J. H. Shin, D. H. Bae, *Compos. Sci. Technol.* 2011, 71, 1699.

References

- [12] P. Q. Dai, W. C. Xu, Q. Y. Huang, *Mater. Sci. Eng. A* 2008, 483–484, 172.
- [13] L. Reinert, M. Zeiger, S. Suárez, V. Presser, F. Mücklich, *RSC Adv.* 2015, 5, 95149.
- [14] G. B. Rathmayr, A. Hohenwarter, R. Pippan, *Mater. Sci. Eng. A* 2013, 560, 224.
- [15] G. B. Rathmayr, R. Pippan, *Scr. Mater.* 2012, 66, 507.
- [16] G. B. Rathmayr, R. Pippan, *Acta Mater.* 2011, 59, 7228.
- [17] Y. H. Zhao, Y. Z. Guo, Q. Wei, T. D. Topping, A. M. Dangelewicz, Y. T. Zhu, T. G. Langdon, E. J. Lavernia, *Mater. Sci. Eng. A* 2009, 525, 68.
- [18] G. B. Rathmayr, A. Bachmaier, R. Pippan, *J. Test. Eval.* 2013, 41, 1.
- [19] I. Y. Archakov, V. U. Kazykhanov, V. G. Konakov, O. Y. Kurapova, A. E. Medvedev, M. Y. Murashkin, N. N. Novik, I. A. Ovid’Ko, E. N. Solovyeva, R. Z. Valiev, *Rev. Adv. Mater. Sci.* 2017, 50, 13.
- [20] A. Katzensteiner, K. Aristizabal, S. Suarez, R. Pippan, A. Bachmaier, *IOP Conf. Ser. Mater. Sci. Eng.* 2017, 194, 12019.
- [21] N. J. Sørensen, S. Suresh, V. Tvergaard, A. Needleman, *Mater. Sci. Eng. A* 1995, 197, 1.
- [22] V. V. Ganesh, N. Chawla, *Metall. Mater. Trans. A* 2004, 35, 53.
- [23] M. Spies, K. Salama, *Ultrasonics* 1990, 28, 370.
- [24] A. Hohenwarter, A. Bachmaier, B. Gludovatz, S. Scheriau, R. Pippan, *Int. J. Mater. Res.* 2009, 100, 1653.
- [25] <http://www.microsample.eu/specimen-preparation/> (accessed: June 12, 2018).
- [26] S. Suarez, F. Lasserre, F. Mücklich, *Mater. Sci. Eng. A* 2013, 587, 381.
- [27] K. Aristizabal, A. Katzensteiner, A. Bachmaier, F. Mücklich, S. Suárez, *Mater. Charact.* 2018, 136, 375.

Co-authored publications

Publication C: Evolution of the microstructure in carbon nanotube reinforced Nickel matrix composites processed by high-pressure torsion

K. Aristizabal, A. Katzensteiner, F. Mücklich, S. Suárez, and A. Bachmaier, IOP Conf. Ser. Mater. Sci. Eng., vol. 258, p. 012008, 2017.

Publication D: Study of the structural defects on carbon nanotubes in metal matrix composites processed by severe plastic deformation

K. Aristizabal, A. Katzensteiner, A. Bachmaier, F. Mücklich, and S. Suarez, Carbon N. Y., vol. 125, pp. 156–161, 2017.

Publication E: On the reinforcement homogenization in CNT/metal matrix composites during severe plastic deformation

K. Aristizabal, A. Katzensteiner, A. Bachmaier, F. Mücklich, and S. Suárez, Mater. Charact., vol. 136, no. January, pp. 375–381, 2018.

Publication F: Evolution of the lattice defects and crystalline domain size in carbon nanotube metal matrix composites processed by severe plastic deformation

K. Aristizabal, A. Katzensteiner, M. Leoni, F. Mücklich, and S. Suárez, *Mater. Charact.*, vol. 154, no. April, pp. 344–352, Aug. 2019.

Publication G: Friction and Tribo-Chemical Behavior of SPD-Processed CNT-Reinforced Composites

K. Aristizabal, A. Tayrac, A. Katzensteiner, A. Bachmaier, and S. Suarez, *Lubricants*, vol. 7, no. 75, pp. 1–10, 2019.